Excited nucleons on the lattice with chirally improved fermions

DIPLOMARBEIT

von
Dirk Brömmel
aus Regensburg

durchgeführt am
Institut Physik I – Theoretische Physik
der Universität Regensburg
unter Anleitung von Prof. Dr. A. Schäfer

Januar 2004

"Zwei mal drei macht vier, wiedewiedewid und drei macht Neune,
Ich mach' mir die Welt, wiedewiede wie sie mir gefällt."

— from "Pippi Langstrumpf" by Astrid Lindgreen

Contents

Preface

The advent of particle physics and accelerators at the beginning of the last century led to the discovery of many new particles, some of which could not be explained by the theories known at this point. A new quantum number was predicted in order to retain the Pauli principle. The quantum number was called *colour* with a corresponding interaction mediated by the colour or strong force.

The theory of Quantum Chromodynamics (QCD) is a relativistic quantum field theory describing the strong force. The relevant fermion fields are *quarks* which interact via gauge bosons, the *gluons*. Other fundamental forces are gravitation and the weak and electromagnetic interaction. The latter two can be combined to form the electroweak sector. Together with QCD this is the basis of the standard model of particle physics.

One key feature of QCD is asymptotic freedom, i.e. the fact that the coupling constant becomes small for high energies or equivalently for very short distances. Within this high energy regime, perturbation theory can successfully be applied to QCD. The perturbative approach allows for a description of cross-sections and processes occurring in accelerators. However, many phenomena at low energy cannot be treated perturbatively, especially static properties of hadrons. It is only possible to provide qualitative descriptions based on quark models.

The low energy regime on the other hand has recently become a very active field where one attempts to apply QCD to nuclear physics. Hadrons are highly complex objects and deriving their properties from fundamental degrees of freedom is a great challenge. A non-perturbative approach is necessary to describe the strong forces inside the hadrons. At present, only lattice QCD can fill this gap and provide insights by calculations from first principles. Unlike models of forces and degrees of freedom inside the hadrons, lattice QCD makes predictions possible for the internal degrees of freedom and some observables.

The spectrum of baryons, for example, is experimentally well established. However, the numerous existing quark models – be it relativistic or non-relativistic, with or without QCD input – have shortcomings in describing the spectrum correctly. For example, the models cannot solve the longstanding puzzle of the ordering of the excited nucleon states with both parities. Experimentally, the excited positive parity Roper $N(1440)$ resonance lies lower in mass than the negative parity ground state $N(1535)$. An equivalent ordering is found for other baryons, e.g. the Λ and Σ resonances. The quark models either cannot reproduce this ordering or give qualitatively wrong energy levels.

For these reasons, lattice simulations try to contribute to this field for almost two decades now. In the beginning only the ground state nucleon $N(939)$ could be resolved. Improved techniques then made it possible to resolve the first excited state. Only recently has it been possible to explore the negative parity

sector including the $N(1535)$ and $N(1650)$. This work aims at improving the results from the lattice by a different analysis and high precision.

The different approach for the analysis of the data is based on a variational method. This method promises to separate the ground and excited states more clearly. High precision on the other hand can be achieved by using chirally improved fermions. This kind of fermions makes it possible to reach smaller quark masses and obtain results closer to the physical region. Chiral symmetry is believed to be responsible for some effects in the nucleon spectrum and thus reaching small quark masses could reveal dynamics.

Parts of this work have been published [BCG$^+$04] and also presented at the 21$^{\text{st}}$ International Symposium on Lattice Field Theory (Lattice 2003) [BCG$^+$03].

Outline of this work

In Chapter 1 we briefly discuss QCD and illustrate the ideas that lead to the lattice formulation. The starting point is Feynman's path integral formulation in Euclidean space. This approach can be extended to the lattice quite naturally and is used for simulations in quantum field theory. To give a self-contained description we introduce the QCD Lagrangian and explain the importance of chirality. We then show how observables can be calculated. Chapter 1 also accounts for the Dirac operator and the gauge action implemented in our simulation.

The next chapter discusses the multiplet structure of baryons seen in experiments. Although only approximately applicable, we show that a spin-flavour SU(6) group structure resembles the structure of the particles. The discussion connects again to the lattice with the explanation of the interpolating fields for the nucleon. These operators are used to 'create' the desired particles on the lattice. Combined to correlation functions, they provide the matrix elements which we use to extract the masses of the states.

Chapter 3 gives more technical details of the simulation. This includes the description of the variational approach which is used to disentangle our nucleon operators in terms of more physical solutions. We also explain in detail the fitting techniques applied in our work.

In the subsequent chapter we will present our results. Starting with a first test to show that the numerical tools are under control, we continue with a discussion of the masses found. The multiplet structure from Chapter 2 then helps to analyse the content of our optimal operators obtained from the variational method. The chapter closes with a short discussion of finite size and discretisation errors and a comparison to other groups.

We then summarise the findings and give an outlook on possible future improvements.

The appendix includes the used notation along with some calculations omitted in the main text. We also provide tables with the compiled data from the simulation.

Chapter 1

QCD on the lattice

Putting QCD on the lattice is a non-perturbative approach to the quantum field theory of the strong force. The aim of this chapter is to briefly discuss QCD and the basic ideas which lead to the lattice formulation. Let us outline the steps that will be addressed.

The first of the necessary building blocks is Feynman's path integral formulation, sometimes called functional integral formalism.[1] In addition, numerical simulations in the lattice approach are only possible in Euclidean space. This is achieved by rotating the time axis in the complex plane, a step known as Wick rotation.[2]

After that we will see that the regularisation scheme provided by the lattice gives rise to a finite, mathematically well defined expression for the path integral. Using this regularisation, we take a look at the physical observables. At this point we will find a similarity between quantum field theory and statistical mechanics. The methods of Monte Carlo simulation[3] known in statistical physics then allow for a numerical treatment of QCD on the lattice.

Having seen how quantum field theory can be implemented on the lattice, we then introduce the QCD Lagrangian with its fermionic and gauge field parts. With the precise definitions for the field theory, we return to physical observables and general techniques of calculating these observables. This involves the so-called generating functional which is derived in detail.

A separate section will then address chiral symmetry. Chiral symmetry and its spontaneous breaking play an important role in QCD. Because of its physical importance, it cannot be ignored in lattice QCD and we discuss how it can be implemented via the so-called Ginsparg-Wilson equation for the Dirac operator.

Finally, we will briefly review the chirally improved fermions used in this work which approximate a solution of the Ginsparg-Wilson equation. This is accompanied by an explanation of the improved gauge action used in our simulation.

[1] An exhaustive description can be found in e.g. [FH65]
[2] Examples are in any textbook on QCD, e.g. [Mut00, PS95]
[3] An introduction to Monte Carlo simulation in statistical methods is e.g. [BH97]

1.1 The path integral formulation

1.1.1 The Euclidean path integral for a quantum mechanical system

The starting point for the derivation of the path integral is the time evolution operator $\mathcal{U}(t)$ (e.g. in [Sch95])

$$|x,t\rangle = \mathcal{U}(t)\,|x\rangle \tag{1.1}$$

which describes how the time independent Heisenberg state $|x\rangle$ evolves in time. Especially useful formulations are obtained if we use the so-called Euclidean time[4] as we will see later. This corresponds to a change from real time t to imaginary time τ

$$t = -\mathrm{i}\tau\,, \qquad \tau > 0 \tag{1.2}$$

and is equivalent to a rotation of the time axis in the complex plane, sometimes called Wick-rotation. For simplicity, t will denote Euclidean time from now on. We find for a time independent Hamiltonian $\mathcal{H}$

$$\mathcal{U}(t) = \mathrm{e}^{-\mathcal{H}t}. \tag{1.3}$$

Here and throughout the work we will use $\hbar = 1$. The transition amplitude for a particle travelling from x' to x'' within time t then is

$$\langle x''|\,\mathcal{U}(t)\,|x'\rangle\,. \tag{1.4}$$

For the case of a free particle with $\mathcal{H} \equiv \mathcal{H}_0 = \frac{\mathcal{P}^2}{2m}$ this amplitude can be calculated directly after inserting a complete set of momentum eigenstates:

$$\begin{aligned}\langle x''|\,\mathrm{e}^{-\mathcal{H}_0 t}\,|x'\rangle &= \int \mathrm{d}p\,\big\langle x''|\mathrm{e}^{-\mathcal{H}_0 t}|p\big\rangle\,\langle p|x'\rangle = \int \mathrm{d}p\,\langle x''|p\rangle\,\mathrm{e}^{-\frac{\mathcal{P}^2}{2m}t}\,\langle p|x'\rangle \\ &= \int \frac{\mathrm{d}p}{2\pi}\,\mathrm{e}^{\mathrm{i}p(x''-x')}\,\mathrm{e}^{-\frac{p^2}{2m}t} = \Big(\frac{m}{2\pi t}\Big)^{1/2}\mathrm{e}^{-\frac{m}{2t}(x''-x')^2}. \end{aligned}\tag{1.5}$$

If a potential $\mathcal{V}$ is included in the Hamiltonian this calculation is spoiled because in general $\mathcal{V}$ and $\mathcal{H}_0$ do not commute. The result is that the integration cannot be performed in a closed form. To overcome this problem we consider the time evolution operator for small (Euclidean) time ε. Now the operator $\mathcal{U}$ can be approximated by:

$$\mathcal{U}_\varepsilon = \mathrm{e}^{-\mathcal{H}\varepsilon} = \mathcal{U}'_\varepsilon + \mathscr{O}(\varepsilon^3) \tag{1.6}$$

where

$$\mathcal{U}'_\varepsilon = \exp\left(-\frac{1}{2}\mathcal{V}\varepsilon\right)\exp\left(-\mathcal{H}_0\varepsilon\right)\exp\left(-\frac{1}{2}\mathcal{V}\varepsilon\right). \tag{1.7}$$

To see that this approximation holds even for a non-vanishing commutator of $\mathcal{V}$ and $\mathcal{H}_0$, one has to compare the power-series expansion of (1.6) and

$$\mathcal{U}_\varepsilon = \exp\left(-[\mathcal{H}_0 + \mathcal{V}]\varepsilon\right). \tag{1.8}$$

[4] This term is used because the metric then changes from Minkowski metric to an Euclidean metric

With $\mathcal{U}'_\varepsilon$ from (1.7) a calculation as in (1.5) now yields the result

$$\langle x''|\,\mathcal{U}'_\varepsilon\,|x'\rangle = \Big(\frac{m}{2\pi\varepsilon}\Big)^{1/2} \exp\Big(-\frac{m}{2\varepsilon}(x''-x')^2 - \frac{\varepsilon}{2}(V(x'')+V(x'))\Big)\,. \tag{1.9}$$

Dividing our time interval t into N small slices of size $\varepsilon = \frac{t}{N}$ we can now use the Trotter formula[5]

$$\exp\left(-[\mathcal{H}_0+\mathcal{V}]t\right) = \lim_{N\to\infty} {\mathcal{U}'_\varepsilon}^N \tag{1.10}$$

to compute the transition amplitude (1.4) for arbitrary time t and any Hamiltonian $\mathcal{H}$. By inserting $N-1$ complete sets of position eigenstates and using (1.9) we obtain:

$$\begin{aligned}
\langle x''|\,\mathrm{e}^{-\mathcal{H}t}\,|x'\rangle &= \lim_{N\to\infty}\int \mathrm{d}x_1\cdots\mathrm{d}x_{N-1}\,\langle x''|\mathcal{U}'_\varepsilon\,|x_1\rangle\cdots\langle x_{N-1}|\,\mathcal{U}'_\varepsilon\,|x'\rangle \\
&= \lim_{N\to\infty}\Big(\frac{m}{2\pi\varepsilon}\Big)^{N/2}\int \mathrm{d}x_1\cdots\mathrm{d}x_{N-1} \\
&\quad\times\exp\Bigg(-\frac{m}{2\varepsilon}\left[(x''-x_1)^2+\cdots+(x_{N-1}-x')^2\right] \\
&\quad-\varepsilon\left[\frac{1}{2}V(x'')+V(x_1)+\cdots+V(x_{N-1})+\frac{1}{2}V(x')\right]\Bigg).
\end{aligned} \tag{1.11}$$

Denoting the exponent by $-S_\varepsilon[x]$ we see that this is an approximation to the classical Euclidean action S:

$$S[x] = \int_0^t \mathrm{d}t'\,\Big(\frac{m}{2}\dot{x}^2+V(x)\Big) = S_\varepsilon[x]+\mathscr{O}(\varepsilon^2). \tag{1.12}$$

The square brackets here indicate that S is a functional depending on functions $x(t)$. Note that the boundary conditions are $x(t)=x''$ and $x(0)=x'$. On the r.h.s. of (1.11) the time interval t is divided into N time slices. For every time slice the integration is performed over the coordinate x_k (Figure 1.1). Taking the formal limit $N\to\infty$ while $t=N\varepsilon$ is kept constant, we write for the measure

$$[\mathrm{d}x] = \lim_{N\to\infty}\Big(\frac{m}{2\pi\varepsilon}\Big)^{N/2}\mathrm{d}x_1\cdots\mathrm{d}x_{N-1} \tag{1.13}$$

and then obtain

$$\langle x''|\,\mathrm{e}^{-\mathcal{H}t}\,|x'\rangle = \int[\mathrm{d}x]\;\mathrm{e}^{-S[x]}. \tag{1.14}$$

This is the Euclidean path integral for the transition amplitude of a particle travelling from x' to x''. The integration is performed over all possible paths $x(t)$ with x' and x'' as boundary values. Hence the integral is infinite dimensional. Since the integral is taken over functions $x(t)$ instead of variables x, equation (1.14) is also called functional integral. The difference to standard integrals is stressed by denoting the measure as $[\mathrm{d}x]$. We will later see that any operator in the expectation value on the l.h.s. of (1.14) can be replaced by a

[5] A proof for this formula for finite-dimensional matrices can for example be found in [MM97].

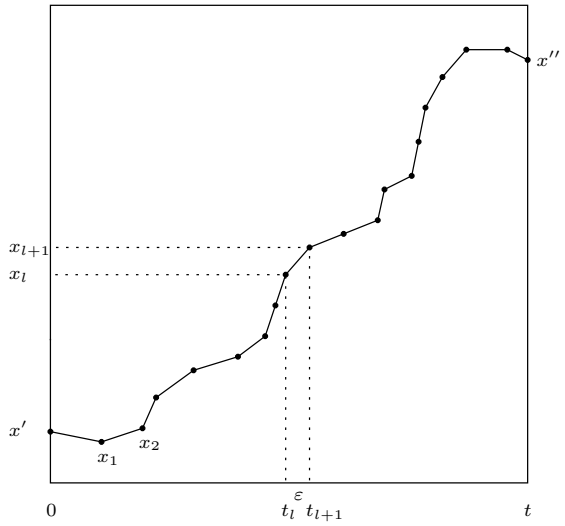

Figure 1.1: Transition time t divided into N time slices separated by $\varepsilon = \frac{t}{N}$. For every time interval the integration is then performed over x_l.

functional in the integral on the r.h.s. This integral Includes a weight factor in form of an exponential containing the classical action S. A completely classical problem corresponds to the limit $\hbar \to 0$. In this case the weight factor[6] would be dominated by the classical solution. All other paths which deviate from this solution would be suppressed exponentially. This formulation and its interpretation is mathematically well defined because of the Euclidean time used. Using real time the exponential would be complex, the weight factor thus strongly oscillating and questions of convergence become an issue. This limits the practical benefits of the path integral as opposed to the Euclidean path integral. From now on, if we say path integral we always refer to the Euclidean path integral.

1.1.2 The Euclidean path integral in quantum field theory

So far, the discussion was limited to *particles* travelling from x' to x''. But a theory of elementary particles requires dynamical systems of *fields*. Instead of quantising systems of particles we have to quantise field variables $\phi(x)$. In the formalism of path integrals this is done by replacing the variables x by fields ϕ. In addition, the fields are not scalar in our case, but ϕ is used as a general variable denoting spinor and vector fields for quarks and gluons respectively.

The derivation is analogous to Section 1.1.1. The path integral expression for the transition amplitude from ϕ' to ϕ'' within time t then reads

$$\left\langle \phi'' | \mathrm{e}^{-\mathcal{H}t} | \phi' \right\rangle = \int [\mathrm{d}\phi]\ \mathrm{e}^{-S[\phi]}, \tag{1.15}$$

where S is again the Euclidean action. For the fields ϕ we have $\phi(0) = \phi'$ and $\phi(t) = \phi''$ as boundary conditions. The measure $[\mathrm{d}\phi]$ denotes the integration over all values of the fields at all space-time points. Formally this can be written

[6] When $\hbar$ is included explicitly the weight factor reads $\exp(-1/\hbar\, S[x])$

as a product over all space-time points

$$[\mathrm{d}\phi] = \prod_{\boldsymbol{x},t} \mathrm{d}\phi(\boldsymbol{x},t). \tag{1.16}$$

1.2 Lattice regularisation

As they stand the expressions (1.15) and (1.16) are not satisfactory in a mathematical sense. We need to apply some regularisation to make the path integral mathematically well defined.

Looking at classical field theories, such techniques are not necessary. In most cases, the atomic scale provides a natural cutoff where the continuum description no longer applies.

In perturbative quantum field theory, however, a cutoff has to be included. To name but a few methods there is Pauli-Villars regularisation, dimensional regularisation or the technique of including a momentum cutoff. The expressions are mathematically well defined after applying any such method. Nevertheless the results for observables may still be divergent in the limit when the cutoff is removed. One then has to include counter terms and renormalise operators to obtain finite physical results.

However, these regularisation schemes were developed for perturbative QCD. Here we implement a different approach that is almost obvious and quite natural. The derivation of the path integral required the use of discrete time slices. The discretisation is now extended to space as well by introducing a lattice with lattice constant a. This minimum distance corresponds to a maximum energy and thus naturally provides an ultraviolet cutoff. Limiting the now discretised space-time to a finite four-volume $V \times T$ we also obtain the necessary infrared cutoff.

The discretisation of space-time together with the finite volume also reduces the infinite number of degrees of freedom to a finite set and thus makes the problem suitable for numerical simulations. The simulation is done on a finite hyper-cubic lattice where the fermion fields ψ are put on the lattice sites and the gauge fields A_μ on the links between these sites. Periodic or anti-periodic boundary conditions are introduced to minimise boundary effects. Finally the limits to infinite volume and vanishing lattice spacing are then applied to the results of the simulation.

1.3 Correlation functions

Physical observables are obtained by calculating expectation values like (1.4) or (1.15), being simple examples of two-point correlation functions. We already related path integrals to these time evolution problems and thus provided a method to calculate these expectation values.

However, up to now we only considered the transition amplitude for a field configuration changing from ϕ' to ϕ''. In general we are interested in matrix elements of operators between physical states, e.g. $\langle n|\mathcal{O}|m\rangle$, and in the energy eigenvalues E_n of the Hamiltonian. For two operators $\mathcal{O}_A$ and $\mathcal{O}_B$, we will find that

$$\mathrm{Tr}\left(\mathcal{O}_B\, \mathrm{e}^{-\mathcal{H}t}\mathcal{O}_A\, \mathrm{e}^{-\mathcal{H}(T-t)}\right) \tag{1.17}$$

is an especially useful expression for computing the desired matrix elements. The first exponential in equation (1.17) is the time evolution from 0 to t. T is the total time extent of the hyper-cubic lattice used for regularisation. Hence the second exponential together with the trace is the evolution due to the periodic boundary conditions on the lattice. Particles described by the fields can propagate not only forward in time, but making the time coordinate circular also backwards in time (see Figure 1.2).

The trace in (1.17) can be evaluated over any complete set of states. A suitable choice are the eigenstates $|0\rangle, |1\rangle, \ldots$ of the Hamiltonian $\mathcal{H}$ with eigenvalues $E_0 < E_1 < \ldots$. We then have

$$\begin{aligned}
\mathrm{Tr}\Big(\mathcal{O}_B\, \mathrm{e}^{-\mathcal{H}t}\mathcal{O}_A\, \mathrm{e}^{-\mathcal{H}(T-t)}\Big) &= \sum_{n=0}^{\infty} \langle n|\, \mathcal{O}_B\, \mathrm{e}^{-\mathcal{H}t}\mathcal{O}_A\, \mathrm{e}^{-\mathcal{H}(T-t)}\, |n\rangle \\
&= \sum_{n,m=0}^{\infty} \langle n|\, \mathcal{O}_B\, \mathrm{e}^{-\mathcal{H}t}\, |m\rangle\, \langle m|\, \mathcal{O}_A\, \mathrm{e}^{-\mathcal{H}(T-t)}\, |n\rangle \\
&= \sum_{n,m=0}^{\infty} \langle n|\, \mathcal{O}_B\, |m\rangle\, \langle m|\, \mathcal{O}_A\, |n\rangle\, \mathrm{e}^{-E_m t}\mathrm{e}^{-E_n(T-t)}.
\end{aligned} \tag{1.18}$$

In addition, we define the partition function Z as

$$Z(T) \equiv \mathrm{Tr}\left(\mathrm{e}^{-\mathcal{H}T}\right) = \sum_{n=0}^{\infty} \langle n|\, \mathrm{e}^{-\mathcal{H}T}\, |n\rangle = \sum_{n=0}^{\infty} \mathrm{e}^{-E_n T}. \tag{1.19}$$

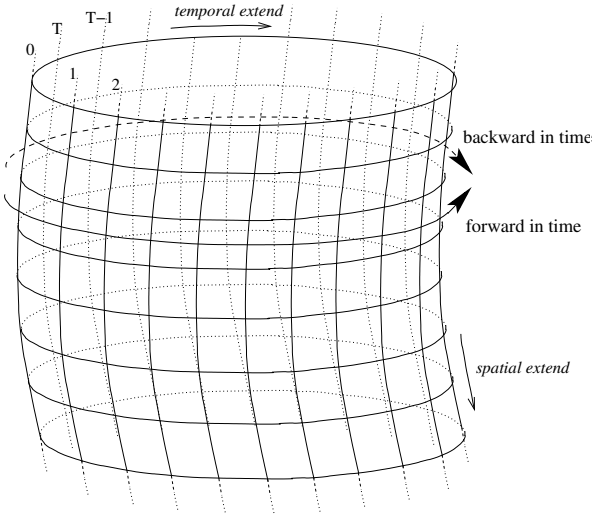

Figure 1.2: Particles can propagate either way around the lattice, forward and backward in time.

Looking at the ratio of (1.18) and (1.19)

$$\begin{aligned}
&\frac{1}{Z(T)}\mathrm{Tr}\left(\mathcal{O}_B\,\mathrm{e}^{-\mathcal{H}t}\mathcal{O}_A\,\mathrm{e}^{-\mathcal{H}(T-t)}\right) = \frac{1}{Z(T)}\sum_{n=0}^{\infty}\langle n|\,\mathcal{O}_B\,\mathrm{e}^{-\mathcal{H}t}\mathcal{O}_A\,\mathrm{e}^{-\mathcal{H}(T-t)}\,|n\rangle \\
&= \sum_{n,m=0}^{\infty}\langle n|\mathcal{O}_B|m\rangle\,\mathrm{e}^{-E_m t}\,\langle m|\mathcal{O}_A|n\rangle\,\mathrm{e}^{-E_n(T-t)}\Big[\mathrm{e}^{-E_0 T}+\mathrm{e}^{-E_1 T}+\cdots\Big]^{-1} \\
&= \sum_{n,m=0}^{\infty}\langle n|\mathcal{O}_B|m\rangle\,\mathrm{e}^{-(E_m-E_0)t}\langle m|\mathcal{O}_A|n\rangle\,\mathrm{e}^{-(E_n-E_0)(T-t)}\Big[1+\mathrm{e}^{-(E_1-E_0)T}+\cdots\Big]^{-1}
\end{aligned} \tag{1.20}$$

we see that all energy levels E_n and also matrix elements like $\langle n|\mathcal{O}_B|m\rangle$ are contained in this expression. Note that only energy differences $E_n - E_0$ to the vacuum energy are directly accessible. This is however sufficient, since experiments also measure the difference to the ground state energy only. We will therefore rename the energy: $(E_n - E_0) \to E_n$.

Re-writing the summation, we can explicitly separate the energy levels in different terms. Let $a, a', \ldots$ be the states with non-vanishing overlap with $\mathcal{O}_A$, ordered such that $E_a < E_{a'} < \ldots$ and the states $b, b', \ldots$ ordered correspondingly. We then have

$$\begin{aligned}
&\frac{1}{Z'(T)}\sum_{n,m=0}^{\infty}\langle n|\mathcal{O}_B|m\rangle\,\mathrm{e}^{-E_m t}\,\langle m|\mathcal{O}_A|n\rangle\,\mathrm{e}^{-E_n(T-t)} \\
&\quad= \frac{1}{Z'}\Big(\langle 0|\mathcal{O}_B|b\rangle\,\langle b|\mathcal{O}_A|0\rangle\,\mathrm{e}^{-E_b t} + \langle a|\mathcal{O}_B|0\rangle\,\langle 0|\mathcal{O}_A|a\rangle\,\mathrm{e}^{-E_a(T-t)} \\
&\qquad + \langle 0|\mathcal{O}_B|b'\rangle\,\langle b'|\mathcal{O}_A|0\rangle\,\mathrm{e}^{-E_{b'}t} + \langle a'|\mathcal{O}_B|0\rangle\,\langle 0|\mathcal{O}_A|a'\rangle\,\mathrm{e}^{-E_{a'}(T-t)} + \ldots\Big)
\end{aligned} \tag{1.21}$$

where Z' is the rescaled partition function

$$Z'(T) = 1 + \mathrm{e}^{-E_1 T} + \mathrm{e}^{-E_2 T} + \cdots\,. \tag{1.22}$$

The crucial property of the traces in (1.17) and (1.19) is that they can be taken over any set of states. Using the basis ϕ of fields in real space, the trace can be connected to path integral expressions (1.15). Instead of having fixed values ϕ' and ϕ'' for the fields at $t = 0$ and $t = T$, we simply set $\phi' = \phi'' = \phi$ and integrate over all configurations ϕ, i.e. we take the trace:

$$\mathrm{Tr}\left(\mathrm{e}^{-\mathcal{H}T}\right) = \int \mathrm{d}\phi\,\langle\phi|\mathrm{e}^{-\mathcal{H}t}|\phi\rangle = \int [\mathrm{d}\phi]\;e^{-S[\phi]} = Z(T). \tag{1.23}$$

Note that this now corresponds to periodic boundary conditions $\phi(0) = \phi(T)$ for the action. Similarly we can derive for the other trace (1.17):

$$\begin{aligned}
\mathrm{Tr}\left(\mathcal{O}_B\,\mathrm{e}^{-\mathcal{H}t}\mathcal{O}_A\,\mathrm{e}^{-\mathcal{H}(T-t)}\right) &= \int \mathrm{d}\phi\,\langle\phi|\,\mathcal{O}_B\,\mathrm{e}^{-\mathcal{H}t}\mathcal{O}_A\,\mathrm{e}^{-\mathcal{H}(T-t)}\,|\phi\rangle \\
&= \int \mathrm{d}\phi\,\mathrm{d}\phi'\,\langle\phi|\,\mathcal{O}_B\,\mathrm{e}^{-\mathcal{H}t}\,|\phi'\rangle\,\langle\phi'|\,\mathcal{O}_A\,\mathrm{e}^{-\mathcal{H}(T-t)}\,|\phi\rangle\,.
\end{aligned} \tag{1.24}$$

Now approximating the time evolution exponentials similar to (1.6) and (1.7), and again using Trotter's formula (1.10), we obtain

$$\begin{aligned}\lim_{N\to\infty} \int \mathrm{d}\phi\, \mathrm{d}\phi_1 \cdots \mathrm{d}\phi_M\, \mathrm{d}\phi'\, \mathrm{d}\phi_{M+1} \cdots \mathrm{d}\phi_N \\ \langle\phi|\mathcal{O}_B|\phi_1\rangle\, \langle\phi_1|\mathcal{U}'_\varepsilon|\phi_2\rangle \cdots \langle\phi_M|\mathcal{U}'_\varepsilon|\phi'\rangle \\ \langle\phi'|\mathcal{O}_A|\phi_{M+1}\rangle\, \langle\phi_{M+1}|\mathcal{U}'_\varepsilon|\phi_{M+2}\rangle \cdots \langle\phi_N|\mathcal{U}'_\varepsilon|\phi\rangle\,,\end{aligned} \tag{1.25}$$

where $\varepsilon = \frac{t}{M} = \frac{T}{N}$. The matrix elements of the operators $\mathcal{O}$ in the basis ϕ turn into functionals $\widetilde{\mathcal{O}}$ of the fields:

$$\begin{aligned}\langle\phi'|\mathcal{O}_A|\phi_{M+1}\rangle &= \widetilde{\mathcal{O}}_A\ \delta(\phi' - \phi_{M+1}), \\ \langle\phi|\mathcal{O}_B|\phi_1\rangle &= \widetilde{\mathcal{O}}_B\ \delta(\phi - \phi_1).\end{aligned} \tag{1.26}$$

We obtain

$$\frac{1}{Z(T)} \mathrm{Tr}\left(\mathcal{O}_B\ \mathrm{e}^{-\mathcal{H}t} \mathcal{O}_A\ \mathrm{e}^{-\mathcal{H}(T-t)}\right) = \frac{1}{Z(T)} \int [\mathrm{d}\phi]\ \widetilde{\mathcal{O}}_B \widetilde{\mathcal{O}}_A\ \mathrm{e}^{-S[\phi]}. \tag{1.27}$$

This is the desired relation between path integrals and correlation functions containing the observables. It is important to note that on the r.h.s. the operators $\mathcal{O}$ are replaced by functionals $\widetilde{\mathcal{O}}$ of the fields being integrated over.

1.4 Quantum field theory and statistical mechanics

With equation (1.27) an analogy between quantum theory and statistical mechanics becomes apparent. For the latter, a general form of the partition function Z reads:

$$Z = \int \mathrm{d}\xi\ \mathrm{e}^{-\beta\mathcal{H}(\xi)}\,, \qquad \beta = \frac{1}{k_B T}. \tag{1.28}$$

Here ξ is a state in configuration space denoting all degrees of freedom. $\mathcal{H}(\xi)$ is the Hamiltonian of the system, T the temperature and k_B the Boltzmann constant. In statistical mechanics the thermal average of any observable $A(\xi)$ in the canonical ensemble is:

$$\langle A(\xi)\rangle_T = \frac{1}{Z} \int \mathrm{d}\xi\ A(\xi) \mathrm{e}^{-\beta\mathcal{H}(\xi)}. \tag{1.29}$$

We see that the Hamiltonian times β in statistical mechanics corresponds to the action S times the omitted $1/\hbar$ in quantum theory. However, equation (1.29) cannot be evaluated explicitly as the number of configurations is very large, often infinite. A technique used in Monte Carlo simulation of statistical mechanics is importance sampling. This is a method where mainly configurations with a large Boltzmann factor $\mathrm{e}^{-\beta\mathcal{H}}$ are considered which are more important for the average. In particular, one generates a set of states ξ_i $(i = 1, 2, \ldots, N)$ distributed according to the statistical weight factor

$$p(\xi_i) = \frac{1}{Z}\ \mathrm{e}^{-\beta\mathcal{H}(\xi_i)}\,, \quad Z = \sum_{i=1}^{N} \mathrm{e}^{-\beta\mathcal{H}(\xi_i)}. \tag{1.30}$$

Picking the N configurations is done by a Markov process.[7] After that, the integral in (1.29) can be approximated by a finite sum:

$$\frac{1}{Z}\int \mathrm{d}\xi\; A(\xi)\mathrm{e}^{-\beta\mathcal{H}(\xi)} \;\rightarrow\; \frac{1}{N}\sum_{i=1}^{N} A(\xi_i). \tag{1.31}$$

To make the connection to the exact results, the limit $N \rightarrow \infty$ has to be taken.

The similarities between quantum theory and statistical mechanics together with the successful application of Monte Carlo simulation in statistical mechanics paved the way for the field of lattice QCD. Simulations therein provide a possibility to make non-perturbative predictions for QCD. It is also important to stress that these predictions are from first principles. No model assumptions have to be included.

1.5 The QCD Lagrangian

So far, we have only mentioned the fields ϕ and the action S in an abstract way, but we have specified neither the fields nor an appropriate action in particular. QCD is a local gauge theory and the degrees of freedom are quark and gluon fields. This section will introduce fermionic fields ψ and the gauge fields A_μ describing the quarks and gluons. The full QCD Lagrangian density $\mathscr{L}_{\mathrm{QCD}}$ as needed for lattice simulation will also be given. The equations of motion and thus the dynamics of the theory can be derived from the Lagrangian density. It also has the advantage that important properties of the theory, such as symmetries, can be read off immediately.

With the Lagrangian density, the action S_{QCD} can be written as

$$S_{\mathrm{QCD}} = \int \mathrm{d}t \int \mathrm{d}^3x\; \mathscr{L}_{\mathrm{QCD}} = \int \mathrm{d}^4x\; \mathscr{L}_{\mathrm{QCD}}. \tag{1.32}$$

Here the Euclidean time is included as the fourth component of x: $x_4 \equiv t$.

The Lagrangian can be split into two parts: one describing the quark fields, the other describing the gauge fields that mediate the strong force:

$$\mathscr{L}_{\mathrm{QCD}} = \mathscr{L}_{\mathrm{fermion}} + \mathscr{L}_{\mathrm{gauge}}. \tag{1.33}$$

1.5.1 Fermionic part of the Lagrangian

The fermion fields in QCD are the fields for the three quark families with their six flavours: *up*, *down*, *charm*, *strange*, *top* and *bottom*:

$$\begin{pmatrix}\mathrm{u}\\ \mathrm{d}\end{pmatrix}\begin{pmatrix}\mathrm{c}\\ \mathrm{s}\end{pmatrix}\begin{pmatrix}\mathrm{t}\\ \mathrm{b}\end{pmatrix}.$$

The corresponding fields are Dirac spinors and denoted by $\psi_\alpha^{(f)}$ where f and α are the flavour and Dirac indices respectively. Every particle also has an antiparticle with the matching field $\bar{\psi}_\alpha^{(f)}$. In addition to flavour, all quarks have the quantum number colour, assuming the values *red*, *blue* or *green*. Writing all

[7] For a complete description see e.g. [BH97]

indices explicitly we would have $\psi^{(f)}_{\alpha,c}$ with c as colour index. Instead we use a vector notation for colour and Dirac components and write $\psi^{(f)}$.

The Pauli exclusion principle characterises fermions and requires them to have anti-symmetric wave functions. As complex valued fields commute, one instead has to use anti-commuting Grassmann valued fields for fermions. For any two Grassmann numbers θ and η we have

$$\theta\eta = -\eta\theta. \tag{1.34}$$

We can now, with the Grassmann valued fields $\psi^{(f)}$ and $\bar{\psi}^{(f)}$ respectively, write down the fermionic part of the Lagrangian:

$$\mathscr{L}_{\text{fermion}} = \bar{\psi}^{(f)}(x)\left(\gamma_\mu D_\mu - m^{(f)}\right)\psi^{(f)}(x). \tag{1.35}$$

Here $m^{(f)}$ is the mass of the quark with flavour f. The γ_μ are 4×4 Dirac matrices[8] in Dirac space with Greek indices μ running from 1 to 4 in Euclidean space. Einstein's summation convention applies for any index.[9] For Dirac and colour indices we use matrix notation. D_μ is the covariant derivative necessary due to the fact that QCD is a locally gauge-invariant theory. It reads:

$$D_\mu \equiv \partial_\mu - \mathrm{i}gA^a_\mu(x)t^a \tag{1.36}$$

with g the coupling constant, A^a_μ the gauge fields being explained in the next section and t^a the eight generators of the algebra su(3).[10] Note that the generators t^a are 3×3 matrices in colour space. The summation convention again applies for a. To understand from where the second of the Hamiltonian $\mathcal{H}$ with eigenvalues $E_0 < E_1 < \ldots$ term of the sum originates, one has to think of the derivative as the difference of the field at two adjacent points. We have a locally gauge-invariant theory and thus this term can be understood as a compensation of the two different colour rotations possible at those two points. For a formulation more suitable for lattice QCD we rescale the gauge fields

$$-\mathrm{i}gA^a_\mu(x)t^a \quad \rightarrow \quad -\mathrm{i}A^a_\mu(x)t^a. \tag{1.37}$$

This changes the covariant derivative (1.36) to

$$D_\mu = \partial_\mu - \mathrm{i}A^a_\mu(x)t^a. \tag{1.38}$$

1.5.2 Gauge field part of the Lagrangian

The gauge fields A_μ in the covariant derivative are necessary to have a gauge invariant theory. As mentioned before, QCD is locally gauge invariant. This implies that the colour orientation of the fields can depend on the position x. The gauge transformations $\Lambda(x)$ in QCD belong to the group SU(3). The fermion fields transform as

$$\begin{aligned} \psi &\rightarrow \Lambda(x)\psi, \\ \bar{\psi} &\rightarrow \bar{\psi}\,\Lambda(x)^{-1}. \end{aligned} \tag{1.39}$$

[8] The Dirac matrices are defined in Appendix A.2

[9] i.e. repeated indices are summed

[10] An explicit form of these generators proportional to the Gell-Mann matrices is given in Appendix A.3

Whereas the covariant derivative transforms as

$$D_\mu \quad \rightarrow \quad \Lambda(x) D_\mu \Lambda(x)^{-1}, \tag{1.40}$$

and thus the Lagrangian in (1.35) remains invariant. It is important to note that the transformation matrices $\Lambda(x)$ do not commute. Thus QCD is a non-Abelian gauge theory, being an example of more general SU(N) Yang-Mills theories.

Having introduced the gauge fields, we now specify their Lagrangian density. As for electrodynamics, this is constructed via a field strength tensor $F^a_{\mu\nu}(x)$:

$$\mathscr{L}_{\text{gauge}} = \frac{1}{4g^2} F^a_{\mu\nu}(x) F^a_{\mu\nu}(x). \tag{1.41}$$

Note that (1.41) is a sum over colour components ($a = 1, \ldots, 8$). The field strength tensor for the gluon field is defined by

$$F^a_{\mu\nu}(x) = \partial_\mu A^a_\nu(x) - \partial_\nu A^a_\mu(x) + f^{abc} A^b_\mu(x) A^c_\nu(x), \tag{1.42}$$

where the f^{abc} are the structure constants of the group SU(3). This expression is analogous to the electric field strength tensor in electrodynamics except for the last term. It arises because the transformation operations do not commute. This term also causes cubic and quadric terms in (1.41) which generate three and four gluon vertices.

1.6 Chiral symmetry in QCD

We now discuss an important property of QCD: chiral symmetry and its spontaneous breaking. Section 1.5.1 introduced the fermionic part of the Lagrangian, $\mathscr{L}_{\text{fermion}}$ (1.35), describing the dynamics of fermions and their coupling to the gauge field. We define the chiral projectors

$$P_{\text{R/L}} \equiv \frac{1}{2}(1 \pm \gamma_5), \tag{1.43}$$

which have the following properties

$$P_{\text{R}} + P_{\text{L}} = 1 \quad \text{and} \quad (P_{\text{R/L}})^2 = P_{\text{R/L}}. \tag{1.44}$$

It is now possible, using (1.43) and (1.44), to decompose the fermion fields into a left- and right-handed part

$$\psi^{(f)} = \psi^{(f)}_{\text{R}} + \psi^{(f)}_{\text{L}} \tag{1.45}$$

where

$$\begin{aligned} \psi^{(f)}_{\text{R/L}} &= P_{\text{R/L}} \psi^{(f)}, \\ \bar{\psi}^{(f)}_{\text{R/L}} &= \bar{\psi}^{(f)} P_{\text{L/R}}. \end{aligned} \tag{1.46}$$

We then insert the sum of the chiral projectors into the fermionic Lagrangian and obtain (again using (1.45))

$$\begin{aligned} &\bar{\psi}^{(f)}(x) \left(\gamma_\mu D_\mu - m^{(f)}\right) \left[P_{\text{R}} + P_{\text{L}}\right] \psi^{(f)}(x) \\ &\qquad = \bar{\psi}^{(f)}(x)\, P_{\text{L}}\, \gamma_\mu D_\mu\, P_{\text{R}}\, \psi^{(f)}(x) + \bar{\psi}^{(f)}(x)\, P_{\text{R}}\, \gamma_\mu D_\mu\, P_{\text{L}}\, \psi^{(f)}(x) \\ &\qquad\quad - m^{(f)} \left[\bar{\psi}^{(f)}(x)\, (P_{\text{R}})^2\, \psi^{(f)}(x) + \bar{\psi}^{(f)}(x)\, (P_{\text{L}})^2\, \psi^{(f)}(x)\right]. \end{aligned}$$

The last line follows from the anti-commutation relation $\{\gamma_5, \gamma_\mu\} = 0$ (see Appendix A.2). This is equivalent to

$$\bar{\psi}_{\mathrm{R}}^{(f)}(x)\,\gamma_\mu D_\mu\,\psi_{\mathrm{R}}^{(f)}(x) + \bar{\psi}_{\mathrm{L}}^{(f)}(x)\,\gamma_\mu D_\mu\,\psi_{\mathrm{L}}^{(f)}(x) - m^{(f)}\left[\bar{\psi}_{\mathrm{R}}^{(f)}(x)\psi_{\mathrm{L}}^{(f)}(x) + \bar{\psi}_{\mathrm{R}}^{(f)}(x)\psi_{\mathrm{L}}^{(f)}(x)\right]. \quad (1.47)$$

From equation (1.47) we see that only the mass term induces a mixing of left- and right-handed fermion fields. Note that $\psi_L^{(f)}$ and $\psi_R^{(f)}$ are eigenstates of γ_5. This leads to the chiral symmetry transformation

$$\begin{aligned} \psi^{(f)} &\rightarrow \mathrm{e}^{-\mathrm{i}\alpha\gamma_5}\,\psi^{(f)}, \\ \bar{\psi}^{(f)} &\rightarrow \bar{\psi}^{(f)}\,\mathrm{e}^{-\mathrm{i}\alpha\gamma_5}. \end{aligned} \quad (1.48)$$

We immediately see that the Lagrangian (1.47) is invariant under the chiral transformation (1.48) for vanishing masses $m^{(f)} = 0$, hence chiral symmetry would be preserved in this case.

However, we do not find chirality to be conserved in nature. The symmetry is broken twofold. First of all, our assumption of vanishing masses $m^{(f)}$ is not met. Luckily, the masses of the up and down quarks are small ($\mathcal{O}(10\,\mathrm{MeV})$) compared to hadron masses ($\mathcal{O}(1\,\mathrm{GeV})$), hence chiral symmetry is approximately fulfilled in the case of two flavours. This is also the basis of chiral perturbation theory, which is an effective field theory describing the dynamics of Goldstone bosons (see e.g. [DGH96]). Chiral perturbation theory can be used to analyse observables in the chiral limit, i.e. at vanishing quark masses, and then perturbation theory in the pion masses is performed. It is, for example, possible to calculate hadron masses and processes at low energies within this framework. Secondly, chiral symmetry is spontaneously broken even for zero quark masses. This breaking is due to the nonzero chiral condensate

$$\langle \bar{\psi}^{(f)} \psi^{(f)} \rangle \neq 0. \quad (1.49)$$

The condensate can be compared to the effect of Cooper-pairs in the theory of superconductivity. In field theory, the condensate of quark anti-quark pairs is caused by the strong attractive interaction between quarks [PS95]. Spontaneous chiral symmetry breaking generates the mass difference between parity partners, e.g. the mass difference of the nucleon ground states of positive and negative parity $N(939)$ and $N(1535)$.[11] In addition, the Goldstone theorem [Gol61] states that spontaneously broken continuous symmetries lead to massless Goldstone bosons. The pion, for example, can be identified with a would-be Goldstone boson having zero mass in the exact chiral limit. This leads to numerous predictions for current matrix elements and pion scattering amplitudes.

[11] The particles and their spectrum are discussed in Section 2.1

1.7 Calculation of correlation functions

With the Lagrangian density from Section 1.5, we can now write down an n-point correlation function in QCD:

$$\begin{aligned}\langle \mathcal{O}_1(t_1)\mathcal{O}_2(t_2)\dots\mathcal{O}_n(t_n)\rangle &\equiv \frac{1}{Z}\int [\mathrm{d}A][\mathrm{d}\psi][\mathrm{d}\bar{\psi}]\ \tilde{\mathcal{O}}_1\tilde{\mathcal{O}}_2\dots\tilde{\mathcal{O}}_n\ \mathrm{e}^{-S[\psi,\bar{\psi},A_\mu]} \\ &= \frac{1}{Z}\int [\mathrm{d}A][\mathrm{d}\psi][\mathrm{d}\bar{\psi}]\ \tilde{\mathcal{O}}_1\tilde{\mathcal{O}}_2\dots\tilde{\mathcal{O}}_n \\ &\quad\times \exp\left(-\int \mathrm{d}^4x\left[\bar{\psi}^{(f)}(\gamma_\mu D_\mu - m^{(f)})\psi^{(f)} - \frac{1}{4g^2}(F^a_{\mu\nu})^2\right]\right)\end{aligned} \tag{1.50}$$

with

$$Z = \int [\mathrm{d}A][\mathrm{d}\psi][\mathrm{d}\bar{\psi}]\ \exp\left(-\int \mathrm{d}^4x\left[\bar{\psi}^{(f)}(\gamma_\mu D_\mu - m^{(f)})\psi^{(f)} - \frac{1}{4g^2}(F^a_{\mu\nu})^2\right]\right). \tag{1.51}$$

Next we can perform the integration over the fermionic part of the action. This can in principle be done for any individual correlation function. However, it is more efficient to use a more general method, the so-called generating functional.

For simplicity we now change to a matrix notation with multi-indices i, j and introduce the Dirac operator $\mathcal{D}_{ij}$ which will be explained in its lattice formulation in Section (1.8.2). The indices i, j denote colour, Dirac and flavour indices as well as discretised space-time positions (x^i_n, t_n). Again a summation over repeated indices is implicitly included:

$$\int \mathrm{d}x\ \bar{\psi}^{(f)}(x)\left(\gamma_\mu D_\mu - m^{(f)}\right)\psi^{(f)}(x) \quad\rightarrow\quad \bar{\psi}_i\,\mathcal{D}_{ij}\,\psi_j. \tag{1.52}$$

1.7.1 The generating functional

A more compact and very neat way of writing down and computing n-point correlation functions is using the generating functional W. It is convenient for finding all possible fermion contractions.

Starting point for the generating functional is the partition function Z from (1.51). In addition to the action S, a source term for every operator is included. So far, we considered abstract functionals $\tilde{\mathcal{O}}$ for the correlation functions. These functionals will consist of products of ψ_i and $\bar{\psi}_i$. The source terms consist of the fields $\psi, \bar{\psi}$ folded with appropriate currents $\bar{\eta}, \eta$:

$$\mathrm{e}^{-S} \rightarrow \mathrm{e}^{-S_{\text{fermion}}-S_{\text{gauge}}+\bar{\eta}_i\psi_i+\bar{\psi}_i\eta_i}. \tag{1.53}$$

The currents $\eta, \bar{\eta}$ are Grassmann valued functions as are the fields. The generating functional then reads

$$W[\eta,\bar{\eta}] = \int [\mathrm{d}A][\mathrm{d}\psi][\mathrm{d}\bar{\psi}]\ \mathrm{e}^{-S_{\text{fermion}}-S_{\text{gauge}}+\bar{\eta}_i\psi_i+\bar{\psi}_i\eta_i}. \tag{1.54}$$

Note that we recover the partition function by evaluating the functional with the currents set to 0

$$Z = W_0 = W[\eta,\bar{\eta}]\Big|_{\eta,\bar{\eta}=0}. \tag{1.55}$$

A correlation function like (1.50) can now simply be calculated by taking derivatives[12] of (1.54):

$$\langle \psi_{i_1} \bar{\psi}_{i_2} \dots \psi_{i_{n-1}} \bar{\psi}_{i_n} \rangle = (-1)^n \frac{1}{W_0} \frac{\partial}{\partial \bar{\eta}_{i_1}} \frac{\partial}{\partial \eta_{i_2}} \cdots \frac{\partial}{\partial \bar{\eta}_{i_{n-1}}} \frac{\partial}{\partial \eta_{i_n}} W[\eta, \bar{\eta}] \Big|_{\eta,\bar{\eta}=0} . \quad (1.56)$$

Within the integral of (1.54), the derivatives each bring down a fermion field from the exponential. The sign emerges from commuting the Grassmann variables and their derivatives.[13] Setting the currents $\eta, \bar{\eta} = 0$ after the differentiation removes the source terms. We thus recover the original form of the correlation function (1.50).

The next step is to compute the generating functional. Therefore the fermionic part of the action in (1.54) is now written as a quadratic expression:

$$\bar{\psi}_i \mathcal{D}_{ij} \psi_j - \bar{\eta}_i \psi_i - \bar{\psi}_i \eta_i = \left[\bar{\psi}_i - \bar{\eta}_k \mathcal{D}^{-1}_{ki}\right] \mathcal{D}_{ij} \left[\psi_j - \mathcal{D}^{-1}_{jk} \eta_k\right] - \bar{\eta}_i \mathcal{D}^{-1}_{ij} \eta_j(y) \quad (1.57)$$

and a change of variables is performed

$$\begin{aligned} \bar{\psi}_i - \bar{\eta}_k \mathcal{D}^{-1}_{ki} &\rightarrow \bar{\psi}_i, \\ \psi_j - \mathcal{D}^{-1}_{jk} \eta_k &\rightarrow \psi_j. \end{aligned} \quad (1.58)$$

Here $\mathcal{D}^{-1}$ is the inverse of $\mathcal{D}$ which is called the quark propagator. The generating functional then reads

$$\int [\mathrm{d}A][\mathrm{d}\psi][\mathrm{d}\bar{\psi}] \mathrm{e}^{-S_{\text{gauge}} - \bar{\psi}_i \mathcal{D}_{ij} \psi_j + \bar{\eta}_i \mathcal{D}^{-1}_{ij} \eta_j} . \quad (1.59)$$

The remaining Gaussian integral can be solved (compare Appendix B.1) and we obtain

$$\int [\mathrm{d}A] \det\mathcal{D} \, \mathrm{e}^{-S_{\text{gauge}} + \bar{\eta}_i \mathcal{D}^{-1}_{ij} \eta_j} . \quad (1.60)$$

The determinant arises due to the integration over the Grassmann valued fermion fields and depends on the gauge fields. The fermion determinant corresponds to closed fermion loops which are contributions of the so-called sea quarks. Simulations that include the fermion determinant are referred to as dynamical calculations. However, dynamical calculations require a big computational effort. Therefore this work and many other simulations are done in the so-called quenched approximation. In this approach the effects of some sea quarks are neglected and the determinant is considered to be constant which reduces the computational complexity. Typically this approximation introduces errors of less than 10 percent in spectrum calculations (see for example [A+03]).

In lattice QCD, the remaining integration over the gauge fields in (1.60) is done using Monte Carlo techniques. Thereby the integral turns into an averaging

[12] The derivatives become functional derivatives $\frac{\delta}{\delta \eta_i}, \frac{\delta}{\delta \bar{\eta}_j}$ in the continuum formulation.

[13] Derivatives of Grassmann numbers obey the same anti-commutation relations like Grassmann numbers themselves. In addition, the partial derivative has to act directly on the number, hence we have to re-order the terms before taking the derivative.

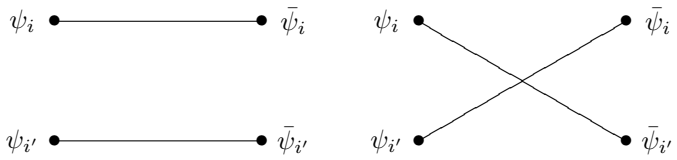

Figure 1.3: A sketch of the possible contractions for a 4-point function. The two diagrams enter with opposite sign because of the Pauli principle.

process over the generated gauge configurations. It is useful to introduce an abbreviation for the remaining gauge integration:

$$\langle \ldots \rangle_G \equiv \frac{1}{W_0} \int [\mathrm{d}A] \, \det\mathcal{D} \, \mathrm{e}^{-S_{\mathrm{gauge}}} \ldots . \tag{1.61}$$

In the quenched approximation, where the fermion determinant is replaced by a constant factor, the remaining gauge integration reads

$$\langle \ldots \rangle_G \equiv \frac{1}{W_0} \int [\mathrm{d}A] \, \mathrm{e}^{-S_{\mathrm{gauge}}} \ldots . \tag{1.62}$$

1.7.2 Wick's Theorem

The generating functional provides a compact notation for n-point correlation functions and shortens much of the calculation. Wick's Theorem now supplies a descriptive way of transcribing the correlation functions in terms of propagators. It is used in a similar fashion as Wick contractions in perturbative QCD for finding Feynman diagrams and their appropriate combinatoric factors. The theorem reads

$$\begin{aligned} &\left\langle \psi_{i_1} \bar{\psi}_{j_1} \psi_{i_2} \bar{\psi}_{j_2} \cdots \psi_{i_n} \bar{\psi}_{j_n} \right\rangle \\ &\qquad = (-1)^n \sum_{\substack{\text{permutations } p \\ \text{of } 1,2,\ldots,n}} \left\langle \mathrm{sign}(p) \, \mathcal{D}^{-1}_{i_1 j_{p_1}} \mathcal{D}^{-1}_{i_2 j_{p_2}} \cdots \mathcal{D}^{-1}_{i_n j_{p_n}} \right\rangle_G . \end{aligned} \tag{1.63}$$

The sign-function[14] preserves the fermionic properties for an interchange of two particles (Figure 1.3). Note that the quark and anti-quark fields only occur pairwise. This becomes clear by looking at (1.60). A single derivative (and similar any odd number) brings down a Dirac propagator $\mathcal{D}^{-1}$ times a source term. Evaluating the result with the sources $\eta, \bar{\eta} = 0$ as demanded in (1.56) eliminates this factor. The occurrence of only pairs of quark and anti-quark fields is also obvious because the propagation can only take place between two fields.

The simplest case of Wick's theorem is for two fields only:

$$\left\langle \psi_{i_1} \bar{\psi}_{j_1} \right\rangle = \left\langle \frac{\partial}{\partial \bar{\eta}_{i_1}} \frac{\partial}{\partial \eta_{j_1}} \mathrm{e}^{\bar{\eta}_i \mathcal{D}^{-1}_{ij} \eta_j} \right\rangle_G \Bigg|_{\eta, \bar{\eta} = 0} . \tag{1.64}$$

[14] $\mathrm{sign}(p)$ is $+1$ for even number of permutations and -1 for odd number of permutations

By performing the calculation

$$\begin{aligned}\left\langle \psi_{i_1}\bar{\psi}_{j_1}\right\rangle &= \left\langle \frac{\partial}{\partial\bar{\eta}_{i_1}}\ \bar{\eta}_i\mathcal{D}^{-1}_{ij_1}\ \mathrm{e}^{\bar{\eta}_i\mathcal{D}^{-1}_{ij}\eta_j}\right\rangle_G\Bigg|_{\eta,\bar{\eta}=0}\\ &= \left\langle \mathcal{D}^{-1}_{i_1j_1}\ \mathrm{e}^{\bar{\eta}_i\mathcal{D}^{-1}_{ij}\eta_j} - \bar{\eta}_i\mathcal{D}^{-1}_{ij_1}\ \mathcal{D}^{-1}_{i_1j}\eta_j\ \mathrm{e}^{\bar{\eta}_i\mathcal{D}^{-1}_{ij}\eta_j}\right\rangle_G\Bigg|_{\eta,\bar{\eta}=0}\\ &= \left\langle \mathcal{D}^{-1}_{i_1j_1}\right\rangle_G,\end{aligned} \tag{1.65}$$

we prove Wick's Theorem for this case. The generalisation of (1.65) to (1.63) can be shown by induction or as carried out in Appendix B.2.

1.8 Chirally improved fermions

We have seen in Section 1.6 that chiral symmetry plays an important role in QCD. This section now discusses the implementation of chiral fermions and thus a chiral Dirac operator on the lattice. The fundamental property of chirally improved fermions for this work is the fact that it is possible to reach smaller bare quark masses [Gat03b]. This is possible because fewer so-called exceptional configurations occur. Smaller quark masses are important to get closer to the physical scale and thus improve chiral extrapolations for the final results. Unless otherwise stated, the following discussion assumes a Dirac operator $\mathcal{D}$ with zero mass.[15]

1.8.1 The Ginsparg-Wilson relation

Until a few years ago it was thought that one cannot implement exact chiral symmetry on the lattice without facing other major drawbacks. The no-go theorem by Nielsen and Ninomiya states that certain essential properties of the Dirac operator cannot hold simultaneously, i.e. there is no local Dirac operator that is chiral and avoids massless doublers at the same time (see [Nie99] and references therein). In Wilson's discretisation of the Dirac operator, chiral symmetry is explicitly broken by an extra term. This term is necessary to avoid massless doublers and becomes irrelevant only in the continuum limit. So in Wilson's approach to lattice QCD chiral symmetry is broken at finite lattice spacing and is only recovered in the continuum limit. Furthermore, an additive quark mass renormalisation requires fine tuning of the bare quark mass. In addition there also is a mixing for operators of different chiral representations.

One of the assumptions of Nielsen and Ninomiya was exact chiral symmetry

$$\{\gamma_5, \mathcal{D}\} = 0. \tag{1.66}$$

According to Ginsparg and Wilson [GW82], it is sufficient to satisfy

$$\{\gamma_5, \mathcal{D}\} = 2a\ \mathcal{D}\,R\gamma_5\,\mathcal{D} \tag{1.67}$$

for any Dirac operator $\mathcal{D}$ to be chirally invariant. Here R is a local operator commuting with γ_5 and a the lattice constant. The condition (1.67) originates from renormalisation group considerations shown for fermions in a gauge field.

[15] With (1.52), this is equivalent to $\mathcal{D} = \gamma_\mu D_\mu$.

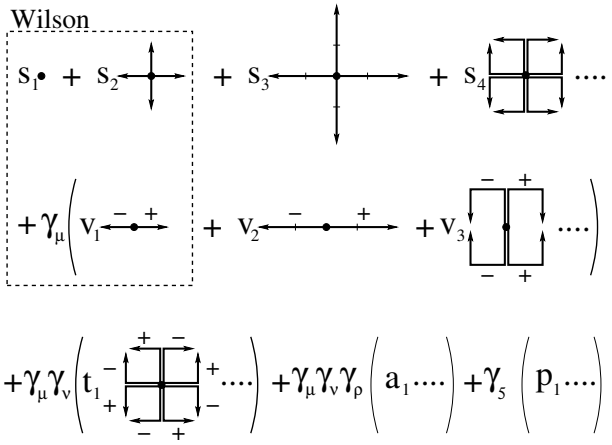

Figure 1.4: Schematic representation of a general lattice Dirac operator, taken from [Gat03b]

Ginsparg and Wilson called this the 'remnant' chiral symmetry criterion. By following this milder condition it is possible to avoid the no-go theorem. Note that the anti-commutation property (1.66) of $\mathcal{D}$ is recovered in the continuum limit $a \to 0$.

1.8.2 A chirally improved Dirac operator

There are several possibilities for chiral fermions obeying the Ginsparg-Wilson relation. Overlap fermions are an exact solution to (1.67) whereas Fixed Point and Chirally Improved (CI) fermions approximate this relation. For this work we will use CI fermions, following the idea developed by Gattringer, Hip and Lang [Gat01, Gat03b, GHL01].

At first, a general lattice Dirac operator consisting of all possible lattice discretisations of the derivative is constructed. A 2-dimensional illustration of such an operator is shown in Figure 1.4. The standard approach by Wilson relies on a constant term and nearest neighbour terms for the derivative, both proportional to the unit matrix, and a term in positive and negative μ-direction summed over all γ_μ. This is depicted within the dashed box in Figure 1.4. The terms are shown as link variables connecting points multiplied with coefficients s_1, s_2 and v_1 respectively. A relative minus sign is necessary for the γ_μ terms to turn them into derivatives. The coefficients are chosen such that there are no doublers. A more general derivative will also include next to nearest neighbours and even more remote points of which the product of link variables is equivalent to paths on the lattice. In addition to including all possible paths in the scalar and vector sector, a general Dirac operator makes use of all 16 elements of the Clifford algebra. Each element of the algebra is multiplied with all paths of link variables. A first set of constraints on the coefficients s_i, v_i, t_i, a_i and p_i is obtained by considering the symmetry transformations C, γ_5-hermiticity, translations, rotations and reflections for the Dirac operator. In particular, certain groups of paths, related by symmetries, come with the same coefficient and possibly some relative signs. The coefficients turn out to be real. The next

step is to insert the expanded Dirac operator directly into the Ginsparg-Wilson relation (1.67) with $R = 1/2$. In doing so, both sides of (1.67) are expanded. It is possible to show that the individual terms are linearly independent, resulting in a system of coupled quadratic equations for the coefficients s_i, v_i, t_i, a_i and p_i. With a truncation of the expanded Dirac operator this system becomes finite and can be solved numerically. The final result is the CI operator which is an approximate solution of the Ginsparg-Wilson relation. A more detailed explanation of the construction of the Dirac operator can for example be found in [GHL01]. A list of terms used in the parametrised Dirac operator along with values for the coefficients used for this simulation can be found e.g. in [BGR, Sch02].

So far, the discussion was limited to a massless Dirac operator $\mathcal{D}$. We need the inverse of this operator, the Dirac propagator $\mathcal{D}^{-1}$, for a simulation. However, a Dirac operator cannot be inverted for vanishing masses. This can be seen as follows: The spectrum of eigenvalues of a Ginsparg-Wilson Dirac operator is located on the Ginsparg-Wilson circle (see Figure 1.5). This circle lies in the complex plane and can be derived from the Ginsparg-Wilson equation (1.67). For zero mass, its centre is on the positive real axis at $1/a$ and its radius is $1/a$. Thus we can have eigenvalues that are zero and the Dirac propagator $\mathcal{D}^{-1}$ is singular. In case of the massive Dirac operator, the intersection of the circle with the real axis is shifted away from the origin by an amount m_q. For smaller and smaller masses, this shift is reduced and the eigenvalues of the Dirac operator get closer to zero, increasing the computational cost of the inversion. For a non Ginsparg-Wilson Dirac operator, the eigenvalues can fluctuate reducing the distance of the smallest eigenvalue from the origin to a value smaller than m_q. These so-called exceptional configurations make the inversion even more costly. One of the benefits of the CI operator is that relatively small bare quark masses m_q can be reached since the eigenvalue fluctuations around the Ginsparg-Wilson circle are small compared to the standard Wilson fermion operator [Gat03b]. However, the main limitation still is the computational effort of inverting the lattice Dirac operator which scales with a large power of the inverse quark mass. In addition, light quark masses are expensive as the linear spatial lattice extent L has to be large relative to the pion mass. This large extent is necessary to avoid finite size effects from pions being exchanged 'around' the boundaries of the lattice. Thus, instead of going to light masses, the operator is calculated for a set of considerably higher quark masses m_q. In the end, the so-called chiral extrapolation is used to obtain the results at physical or vanishing quark masses.

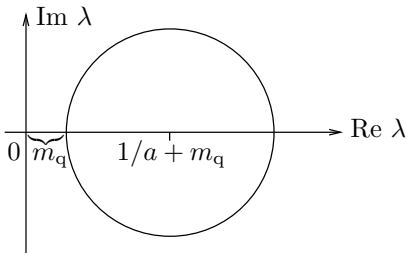

Figure 1.5: The Ginsparg-Wilson circle describing the spectrum of the eigenvalues of the CI operator. For smaller masses the shift m_q reduces and exceptional configurations occur.

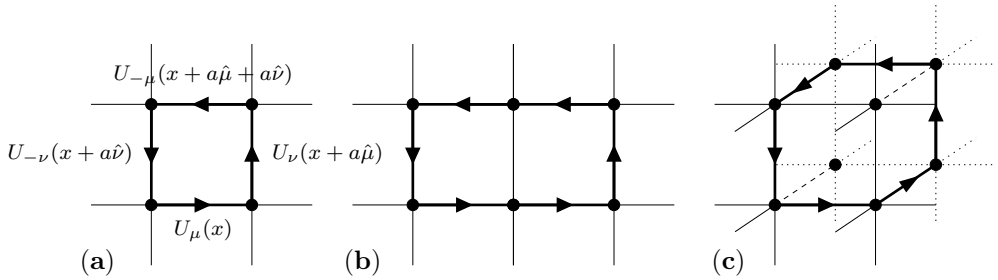

Figure 1.6: Gauge path contributions to the Lüscher-Weisz gauge action. (**a**) the Wilson plaquette $U_{\rm p}$, (**b**) a rectangular path $U_{\rm rect}$ and (**c**) the so-called parallelogram $U_{\rm para}$ lying in three space-time directions. For brevity the link variables are only given for the Wilson plaquette.

1.9 The Lüscher-Weisz gauge action

As for the Dirac operator, we now have to set up a discretised lattice gauge action. The constraints again are that the continuum action is restored for $a \to 0$ and that the symmetries of the action are preserved.

The gauge fields A_μ are directed quantities as can be seen from the Dirac index μ. Therefore it is quite natural to place the fields on the links between lattice sites. These links go in all space-time directions from any given lattice point and thus can support the vector gauge field A_μ. Introducing parallel transporters U_μ, equivalent to path ordered exponentials of the gauge field, it is possible to reformulate the gauge action. The parallel transporters[16] read

$$U_\mu(x) = \mathrm{e}^{\mathrm{i}aA^c_\mu(x)t^c}, \tag{1.68}$$

and transform like

$$U_\mu(x) \quad \to \quad \Lambda(x)U_\mu(x)\Lambda^{-1}(x + a\hat{\mu}). \tag{1.69}$$

For negative indices we define

$$U_{-\mu}(x) = U_\mu(x - a\hat{\mu})^\dagger. \tag{1.70}$$

Here $\hat{\mu}, \hat{\nu}$ are unit vectors in the directions μ, ν. The transformation relation (1.69) proves the parallel transporters suitable for constructing gauge invariant terms needed for a lattice gauge action. We will see that such a discretised action can be constructed as a sum of products of parallel transporters along closed paths. From (1.69) it is obvious that closed paths are gauge invariant.

The simplest kind of closed path is a square on the lattice with side length a. This is the so-called Wilson plaquette (see Figure 1.6.a) from which Wilson constructed the plaquette action. The corners of the plaquette lie on the lattice points x, $x + a\hat{\mu}$, $x + a\hat{\mu} + a\hat{\nu}$ and $x + a\hat{\nu}$. We define the plaquette variable $U_{\rm p}$ as the product of parallel transporters along the plaquette p

$$U_{\rm p} \equiv U_{\mu,\nu}(x) = U_\mu(x)U_\nu(x + a\hat{\mu})U_{-\mu}(x + a\hat{\nu} + a\hat{\mu})U_{-\nu}(x + a\hat{\nu}). \tag{1.71}$$

[16]The index c denotes the colour component index which was called a in the previous sections. It is renamed to avoid confusion with the lattice constant a.

The Wilson plaquette action for SU(3) then is

$$S_{\text{Wilson}}[U] = \sum_{\text{p}} \frac{\beta}{3} \,\text{Re}\left[\text{Tr}(1 - U_{\text{p}})\right], \tag{1.72}$$

which is real and positive. The summation in (1.72) is over all possible 1×1 plaquettes, the trace is over the colour indices. Together with (1.69) – (1.71) we see that (1.72) is gauge invariant. The constant term in the action is physically insignificant and only included to exactly match the continuum expression in the limit $a \to 0$. To show that (1.72) is in fact equivalent to the continuum gauge action, one has to expand (1.68) for small a and insert it into the trace. Using the Campbell-Baker-Hausdorff relation[17] and the lattice approximation for the derivative of the gauge fields,

$$a \cdot \partial_\mu A^c_\nu(x) = A^c_\nu(x + a\hat{\mu}) - A^c_\nu(x) + \mathcal{O}(a^2)\,, \tag{1.73}$$

the Wilson action (1.72) in the continuum limit $a \to 0$ becomes

$$\begin{aligned} S &= \frac{\beta}{4 \cdot 3} \sum_x a^4 \,\text{Tr}\left[F_{\mu\nu}(x) F_{\mu\nu}(x) + \mathcal{O}(a^2)\right] \\ &= \frac{\beta}{8 \cdot 3} \sum_x a^4 \left[F^c_{\mu\nu}(x) F^c_{\mu\nu}(x) + \mathcal{O}(a^2)\right]. \end{aligned} \tag{1.74}$$

Comparing this to the gauge action evaluated with (1.41) yields a relation between β and the coupling constant for the continuum:

$$\beta = \frac{1}{6g^2}. \tag{1.75}$$

The Wilson action considered so far exhibits some arbitrariness in the discretisation scheme. As long as the continuum limit $a \to 0$ matches the continuum action, other additional terms can be used to fine tune the behaviour of the discretised action. In order to suppress discretisation errors, the so-called Lüscher-Weisz gauge action [LW85] has been used in this simulation. This action adds extra terms to the Wilson action (1.72) to cancel the $\mathcal{O}(a^2)$ corrections. The additional terms consist of longer gauge paths in the form of a rectangular path U_{rect} and a so-called parallelogram U_{para} (Figures 1.6.b and 1.6.c respectively). The paths are defined in the following way:

$$\begin{aligned} U_{\text{rect}} = U_{\text{rect}}(x : \mu, \nu) &= U_\mu(x) U_\mu(x + a\hat{\mu}) U_\nu(x + 2a\hat{\mu}) \\ &\quad \times U_{-\mu}(x + 2a\hat{\mu} + a\hat{\nu}) U_{-\mu}(x + a\hat{\mu} + a\hat{\nu}) U_{-\nu}(x + a\hat{\nu}) \end{aligned} \tag{1.76}$$

$$\begin{aligned} U_{\text{para}} = U_{\text{para}}(x : \mu, \nu, \rho) &= U_\mu(x) U_\rho(x + a\hat{\mu}) U_\nu(x + a\hat{\mu} + a\hat{\rho}) \\ &\quad \times U_{-\mu}(x + a\hat{\mu} + a\hat{\nu} + a\hat{\rho}) U_{-\rho}(x + a\hat{\nu} + a\hat{\rho}) U_{-\nu}(x + a\hat{\nu}) \end{aligned} \tag{1.77}$$

The improved Lüscher-Weisz gauge action then reads

$$\begin{aligned} S[U] = &\sum_{\text{p}} \frac{\beta_1}{3} \,\text{Re}\left[\text{Tr}(1 - U_{\text{p}})\right] \;+\; \sum_{\text{rect}} \frac{\beta_2}{3} \,\text{Re}\left[\text{Tr}(1 - U_{\text{rect}})\right] \\ &+ \sum_{\text{para}} \frac{\beta_3}{3} \,\text{Re}\left[\text{Tr}(1 - U_{\text{para}})\right]. \end{aligned} \tag{1.78}$$

[17] The Campbell-Baker-Hausdorff relation reads $\mathrm{e}^x \mathrm{e}^y = \mathrm{e}^{x+y+(1/2)[x,y]+\ldots}$

The summations run over 1×1 plaquettes, 2×1 rectangles and $1 \times 1 \times 1$ parallelograms respectively. The extensions are given from the starting lattice site x in $\hat{\mu}$, $\hat{\nu}$ and $\hat{\rho}$ direction. Here β_1 corresponds to β from the Wilson action. The coefficients β_2 and β_3 can be computed within the framework of tadpole improved perturbation theory [LM93]. The β-values used in this work are summarised in Table D.1.

Chapter 2

Baryons

The spectrum of the nucleons with their associated quantum numbers is experimentally well established. Ultimately we want to be able to calculate the spectrum of the nucleons from first principles. The underlying quantum field theory and the generating functional necessary for this task have been discussed in Chapter 1. Still missing is the connection between field theory and the actual particles. This connection is achieved through the operators that are used for our observables (1.17).

This chapter starts with an explanation of the multiplet structure of baryons in two different ways. First of all with a more historic approach by counting the various states and classifying them into multiplets according to their symmetries. Alternatively, we then consider the underlying group structure first and calculate the multiplets directly. This is followed by an assignment of some particles to the multiplets using a simple model for baryons.

The next section discusses the nucleon operators used in this work. This includes a confirmation of the correct quantum numbers.

In the last part we explicitly calculate the nucleon two-point function in terms of quark propagators. For this derivation we apply the techniques from the previous chapter.

2.1 Quarks and Multiplets

We will establish the multiplet structure of baryons in this section. The first approach will be a simple counting of states combined with a classification in multiplets due to symmetry properties [Bha88]. A somewhat shorter way of obtaining the size of the multiplets is based in group theory and uses Young tableaus [Clo79].

2.1.1 Symmetries and the counting of states

Apart from exotic states like quark-gluons hybrids or pentaquarks, the standard model of particle physics [H$^+$02] knows two types of hadrons: mesons being quark anti-quark pairs and baryons consisting of three quarks. The nucleon is built of three quarks (uud) or (udd) and thus is a baryon. Since baryons are fermions they have an anti-symmetric total wave function. The quantum

number colour is not directly observed in nature. Hence all particles we encounter are 'colourless' and their states are colour singlets.[1] As a consequence, the colour part of the wave function can be separated off and always provides an anti-symmetric factor. The rest of the wave function thus has to be symmetric. The remaining parts are the spatial, spin and flavour degrees of freedom. The total wave function can thus be written as

$$|\text{baryon}\rangle_{\text{A}} = |\text{colour}\rangle_{\text{A}} \times |\text{space, spin, flavour}\rangle_{\text{S}} \,. \tag{2.1}$$

Here A and S denote total anti-symmetry or symmetry respectively. The task is to identify symmetric combinations for the second part $|\text{space, spin, flavour}\rangle_{\text{S}}$ of the wave function.

Although all possible baryons consist of three quarks out of the 3 generations (u, d), (c, s) and (t, b) we limit ourselves to the light quarks u, d and s. The other quarks carry considerably more mass and only appear at much higher energies. We can therefore consider an approximate flavour SU(3).[2] However, this symmetry and thus the mass degeneracy within a multiplet is broken due to the higher mass of the strange quark in comparison to the up and down quark ($m_{\text{u}}, m_{\text{d}} = \mathcal{O}(10\,\text{MeV})$ and $m_{\text{s}} = \mathcal{O}(100\,\text{MeV})$).

We begin with looking at the possible *spin wave functions*. Each quark carries spin $\frac{1}{2}$. Therefore we have a total spin of either $S = \frac{1}{2}$ or $S = \frac{3}{2}$ for baryons and a total number of 2^3 combinations. The states with $S = \frac{3}{2}$ are symmetric with respect to the exchange of any two spins. We label these states with $\chi^{\text{S}}_{3/2}$, super- and subscript denoting symmetry and total spin. There are four possible combinations with $S_z = \frac{3}{2}, \frac{1}{2}, -\frac{1}{2}, -\frac{3}{2}$. In the case of total spin $S = \frac{1}{2}$ we have two types of mixed symmetric[3] states. The first possibility is the coupling of the spins of the first two quarks[4] to $S_{1,2} = 0$. We then couple the third quark to get a spin of $S = \frac{1}{2}$. These states are anti-symmetric under the interchange of quarks 1 and 2 ($1 \leftrightarrow 2$) but there is no overall symmetry under $2 \leftrightarrow 3$ or $1 \leftrightarrow 3$. Clearly there are two such states, namely $S_z = \frac{1}{2}$ and $S_z = -\frac{1}{2}$. We denote them $\chi^{\rho}_{1/2}$. The other possible mixed symmetric combinations are $\chi^{\lambda}_{1/2}$. Here quarks 1 and 2 couple to $S_{1,2} = 1$ and the third quark gives $S = \frac{1}{2}$. The wave function here is symmetric for $1 \leftrightarrow 2$. We again have two such states with $S_z = \pm\frac{1}{2}$. We can now summarise

$$2^3 = 8 = \underbrace{\mathbf{4}}_{\text{S}} + \underbrace{\mathbf{2}}_{\substack{\text{MS} \\ (\rho)}} + \underbrace{\mathbf{2}}_{\substack{\text{MS} \\ (\lambda)}} . \tag{2.2}$$

Here MS refers to the states with mixed-symmetry. Note that there is no totally anti-symmetric state.

Having listed the possible spin wave functions we now account for the *flavour combinations* of the three quarks. We limited ourselves to three flavours to begin

[1] This can be seen as a consequence of confinement. Confinement implies increasing long range interactions between colour charges. As there is no such interaction between hadrons, they must be colour neutral.

[2] Subsequently adding the quarks c,b and t extends to flavour SU(4), SU(5) and SU(6). However, these symmetries are badly broken due to the huge mass difference.

[3] i.e. no overall symmetry for all possible exchanges of any two spins.

[4] Equally we could use any other two quarks. They cannot be distinguished, thus the counting of states has to be independent of this choice.

with: u, d and s. This implies 3^3 different states. Arranging the possible flavours as columns for each quark

(1)	(2)	(3)
u	u	u
d	d	d
s	s	s

we can work out the possibilities. Clearly, we get 3 symmetric states (uuu), (ddd) and (sss), each representing one row. We can also have two identical and one of the remaining flavours: (uud), (uus), (ddu), (dds), (ssu) and (ssd). These combinations can be symmetrised in 1, 2 and 3. One such example is

$$\phi^{\mathrm{S}} = \frac{1}{\sqrt{3}}[\mathrm{uud} + \mathrm{udu} + \mathrm{duu}].$$

In an analogous way there is one possible symmetric state with all three flavours different (uds). Thus there are a total of 10 symmetric states. With three quarks and three flavours we find one totally anti-symmetric state using the Slater determinant. The remaining 16 states are again mixed symmetric. There are 8 of the ρ-type (anti-symmetric under $1 \leftrightarrow 2$) and 8 of the λ-type (symmetric with respect to $1 \leftrightarrow 2$). As before, we summarise:

$$3^3 = 27 = \underbrace{\mathbf{10}}_{\mathrm{S}} + \underbrace{\mathbf{8}}_{\substack{\mathrm{MS} \\ (\rho)}} + \underbrace{\mathbf{8}}_{\substack{\mathrm{MS} \\ (\lambda)}} + \underbrace{\mathbf{1}}_{\mathrm{A}}. \tag{2.3}$$

The next step now is to combine spin with flavour to an approximate *spin-flavour* SU(6) and classify the $2^3 \times 3^3 = 6^3 = 216$ states. What is therefore left, is to build symmetric states as on the r.h.s. of (2.1) with combinations of states from (2.2) and (2.3). We start with joining the 4 symmetric spin states and the 10 symmetric flavour states to form 40 symmetric spin-flavour states. We denote them by $^4\mathbf{10}$, the 4 corresponding to the $2S+1$ spin states for $S = \frac{3}{2}$. In a similar way, the mixed symmetric states can be joined to symmetric spin-flavour combinations with $S = \frac{1}{2}$. These 2×8 combinations are $(\chi^\rho \phi^\rho + \chi^\lambda \phi^\lambda)$. They are denoted by $^2\mathbf{8}$. The totally symmetric states then form a **56**-plet:

$$\underbrace{{}^4\mathbf{10}}_{S=3/2} + \underbrace{{}^2\mathbf{8}}_{S=1/2} = \mathbf{56} \quad (\mathrm{S}). \tag{2.4}$$

There would be a mass degeneracy between $^2\mathbf{8}$ and $^4\mathbf{10}$ without spin-dependent forces. The mass difference within the flavour octets $^2\mathbf{8}$ and decuplets $^4\mathbf{10}$ can for example be explained with the heavier strange quark. Besides forming symmetric states, the mixed-symmetric spin and flavour combinations can also form a totally anti-symmetric (under exchange of any two quarks) set of states. This multiplet is also denoted $^2\mathbf{8}$ and can be written as $(\chi^\rho \phi^\lambda - \chi^\lambda \phi^\rho)$. In addition, the anti-symmetric flavour state can be combined with the symmetric spin states to form a totally anti-symmetric multiplet. We have

$$\underbrace{{}^4\mathbf{1}}_{S=3/2} + \underbrace{{}^2\mathbf{8}}_{S=1/2} = \mathbf{20} \quad (\mathrm{A}). \tag{2.5}$$

56-plet	(S)	$^4\mathbf{10} : \chi^{\mathrm{S}}\phi^{\mathrm{S}}$	$^2\mathbf{8} : \frac{1}{\sqrt{2}}(\chi^\rho\phi^\rho + \chi^\lambda\phi^\lambda)$
70-plet	(ρ)	$^2\mathbf{10} : \chi^\rho\phi^{\mathrm{S}}$	$^4\mathbf{8} : \chi^{\mathrm{S}}\phi^\rho$
		$^2\mathbf{8} : \frac{1}{\sqrt{2}}(\chi^\rho\phi^\lambda + \chi^\lambda\phi^\rho)$	$^2\mathbf{1} : \chi^\rho\phi^{\mathrm{A}}$
70-plet	(λ)	$^2\mathbf{10} : \chi^\lambda\phi^{\mathrm{S}}$	$^4\mathbf{8} : \chi^{\mathrm{S}}\phi^\lambda$
		$^2\mathbf{8} : \frac{1}{\sqrt{2}}(\chi^\rho\phi^\rho - \chi^\lambda\phi^\lambda)$	$^2\mathbf{1} : \chi^\lambda\phi^{\mathrm{A}}$
20-plet	(A)	$^4\mathbf{1} : \chi^{\mathrm{S}}\phi^{\mathrm{A}}$	$^2\mathbf{8} : \frac{1}{\sqrt{2}}(\chi^\rho\phi^\lambda - \chi^\lambda\phi^\rho)$

Table 2.1: Spin-flavour wave functions of baryons, according to their permutation symmetry of any two quarks [Bha88].

The remaining 140 states split equally to mixed-symmetric ρ- and λ-types. They are

$$\begin{aligned} &{}^2\mathbf{10} + {}^4\mathbf{8} + {}^2\mathbf{8} + {}^2\mathbf{1} = \mathbf{70} \quad (\rho), \\ &\underbrace{{}^2\mathbf{10}}_{S=1/2} + \underbrace{{}^4\mathbf{8}}_{S=3/2} + \underbrace{{}^2\mathbf{8}}_{S=1/2} + \underbrace{{}^2\mathbf{1}}_{S=1/2} = \mathbf{70} \quad (\lambda). \end{aligned} \tag{2.6}$$

For completeness, Table 2.1 lists all spin-flavour combinations with the corresponding permutation symmetries. The complete set of multiplets for baryons finally reads

$$6^3 = 216 = \mathbf{56}_{\mathrm{S}} + \mathbf{70}_{\mathrm{MS}} + \mathbf{70}_{\mathrm{MS}} + \mathbf{20}_{\mathrm{A}}. \tag{2.7}$$

2.1.2 Multiplets from group theory

The previous section showed how to find the number of particles in a multiplet by looking at the symmetries and combining spin with flavour. As remarked before, we could also assume (a badly broken) flavour SU(4) (or even SU(6)). Combining that with spin, we would then have a spin-flavour SU(8) (or SU(12)). Instead of deriving the multiplets in the same tedious fashion, a more general method for arbitrary SU(N) is desired. An elegant technique is using Young tableaus.[5]

We know from group theory that the number of particles within the multiplets equals the dimensionality of the irreducible representations that arise from products of the representations of the group [Clo79]. For baryons and a spin-flavour SU(6), such a product would be $\mathbf{6}\otimes\mathbf{6}\otimes\mathbf{6}$. The rules for combining Young tableaus then tell us the dimensions of the irreducible representations. The Young tableau for the fundamental representation is a simple box

$$\boldsymbol{N} = \square\,. \tag{2.8}$$

The conjugate representation[6] in SU(N) is denoted by a column of $N-1$ boxes

[5] Sometimes also called Young diagrams.

[6] As would be necessary for mesons (quark anti-quark pairs): $\mathbf{6}\otimes\bar{\mathbf{6}}$.

$$\bar{\boldsymbol{N}} = \left\{ \begin{array}{ll} \square & 1 \\ \square & 2 \\ \square & 3 \\ \vdots & \\ \square & N-2 \\ \square & N-1 \end{array} \right. . \tag{2.9}$$

The product $\mathbf{6} \otimes \mathbf{6} \otimes \mathbf{6}$ then translates to

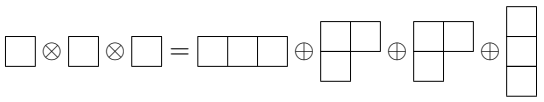

(2.10)

How to find the r.h.s. of (2.10) is subject of Appendix A.5. This result in terms of Young tableaus is essentially the same for any SU(N).[7] Note that Young tableaus with only one row are associated with a totally symmetric representation whereas a column represents a totally anti-symmetric multiplet. Again using the rules for Young tableaus (Appendix A.5) we can assign the multiplet structure

$$\mathbf{6} \otimes \mathbf{6} \otimes \mathbf{6} = \mathbf{56}_{\mathrm{S}} \oplus \mathbf{70}_{\mathrm{MS}} \oplus \mathbf{70}_{\mathrm{MS}} \oplus \mathbf{20}_{\mathrm{A}} \tag{2.11}$$

to (2.10). This corresponds to (2.7) as found by symmetry considerations.

2.1.3 Assignment of particles to multiplets

Sections 2.1.2 and 2.1.1 explained how multiplets can be found from an underlying symmetry. The number of particles, corresponding to the dimensionality of the multiplets, was explicitly derived for a spin-flavour SU(6). The next step in classifying the particles is to assign them to the various multiplets. In the case of SU(6), the found multiplets are given in (2.11). Note that in general such a classification is only approximate because any flavour SU(N) is broken in nature due to the different quark masses. This symmetry breaking, however, is not very strong for flavour SU(2) or SU(3) so their multiplet structure is still observable in nature.

Although the breaking of symmetries spoils a strict classification into multiplets, it can for the same reason be used for conclusions about the structure of the particles. The spin-flavour SU(6) is for example broken by spin-dependent forces and differences in the quark masses. This can explain the different masses of the particles within the same multiplet. It also shows that particles with the same quantum numbers (e.g. $N(939)$ and $N(1440)$) cannot be in the same multiplet. The same spin and flavour quantum numbers would cause the same masses which is evidently not the case for physical baryons [H$^+$02].

According to (2.1), we need the spatial wave functions and have to combine these with the spin-flavour wave functions to finally assign the particles to multiplets. One of the first baryon models used for describing the baryon structure was the oscillator model [Clo79, HK83, Bha88, CR00]. Within this model the symmetry is again extended, now to $SU(6) \times O(3)$. The model uses a Hamiltonian for non-relativistic motion of three quarks in some confining potential.

[7] As fundamental and conjugate representations differ from each other for SU($N \geq 3$), this only holds as there is no conjugate representation on the l.h.s. of (2.10).

(D_6, L_N^P)	J^P	$^{2S+1}D_3$				
$(\mathbf{56}, 0_0^+)$	$\frac{1}{2}^+$	$^2\mathbf{8}$	***N***(939)	Λ(1116)	Σ(1193)	Ξ(1318)
	$\frac{3}{2}^+$	$^4\mathbf{10}$	Δ(1232)	Σ(1385)	Ξ(1530)	Ω(1672)
$(\mathbf{56}, 0_2^+)$	$\frac{1}{2}^+$	$^2\mathbf{8}$	***N***(1440)	Λ(1600)	Σ(1660)	Ξ(?)
$(\mathbf{56}, 2_2^+)$	$\frac{3}{2}^+$	$^2\mathbf{8}$	N(1720)	Λ(1890)	Σ(?)	Ξ(?)
	$\frac{5}{2}^+$	$^2\mathbf{8}$	N(1680)	Λ(1820)	Σ(1915)	Ξ(2030)
		$^4\mathbf{10}$	Δ(1905)	Σ(?)	Ξ(?)	Ω(?)
	$\frac{7}{2}^+$	$^4\mathbf{10}$	Δ(1950)	Σ(2030)	Ξ(?)	Ω(?)
$(\mathbf{70}, 1_1^-)$	$\frac{1}{2}^-$	$^2\mathbf{1}$	Λ(1405)			
		$^2\mathbf{8}$	***N***(1535)	Λ(1670)	Σ(1620)	Ξ(?)
		$^4\mathbf{8}$	***N***(1650)	Λ(1800)	Σ(1750)	Ξ(?)
		$^2\mathbf{10}$	Δ(1620)	Σ(?)	Ξ(?)	Ω(?)
	$\frac{3}{2}^-$	$^2\mathbf{1}$	Λ(1520)			
		$^2\mathbf{8}$	N(1520)	Λ(1690)	Σ(1670)	Ξ(1820)
		$^4\mathbf{8}$	N(1700)	Λ(?)	Σ(?)	Ξ(?)
		$^2\mathbf{10}$	Δ(1700)	Σ(?)	Ξ(?)	Ω(?)
	$\frac{5}{2}^-$	$^4\mathbf{8}$	N(1675)	Λ(1830)	Σ(1775)	Ξ(?)

Table 2.2: Assignment for some of the known baryons in terms of a spin-flavour SU(6) basis. The particles covered in this work are in **bold letters**. D_n refers to the dimensionality with respect to SU(n). Numbers in parentheses are masses in MeV. Taken from [H$^+$02].

Although a non-relativistic treatment of the quarks is far from being realistic, the model was highly successful in baryon spectroscopy. After separating off the centre-of-mass motion by introducing Jacobi coordinates, the intrinsic degrees of freedom correspond to the motion of two independent oscillators. The spatial wave function then is a product of the two oscillator states with the usual principal quantum numbers. The orbital angular momentum L for example is found by coupling the momenta of the independent oscillators. The total angular momentum J of the particle is obtained after coupling L and S, the total spin of the particle. Within this model, it is then possible to denote spatial wave functions with their symmetries.[8] It is now straightforward to construct totally anti-symmetric states as required by (2.1) and assign the particles to the multiplets.

According to the Particle Data Book [H$^+$02] it is useful to classify baryons into bands. These bands have the same number N of quanta of excitation and are composed of several multiplets. We denote the multiplets by (D_6, L_N^P). D_6 is the dimensionality of the SU(6) multiplet, L the orbital angular momentum of the quarks and P the parity of the particles. Some bands with their multiplets and the particles therein are shown in Table 2.2. The $N = 0$ and $N = 1$ bands

[8] Examples for the wave functions can be found in the references given above.

only contain the $(\mathbf{56}, 0_0^+)$ and $(\mathbf{70}, 1_1^-)$ multiplets respectively. The $N = 2$ band contains five multiplets: $(\mathbf{56}, 0_2^-)$, $(\mathbf{70}, 0_2^+)$, $(\mathbf{56}, 2_2^+)$, $(\mathbf{70}, 2_2^+)$ and $(\mathbf{20}, 1_2^+)$. Baryons from the $(\mathbf{20}, 1_2^+)$ multiplet are not likely to ever be observed.

One of the drawbacks of this model is obvious from Table 2.2: the ordering of the states with respect to their parity cannot be reproduced correctly. The oscillator model predicts the states to have alternating parities. Clearly, the first excited nucleon with positive parity – the so-called Roper resonance $N(1440)$ – lies lower in energy than the corresponding negative parity states $N(1535)$ and $N(1650)$. The oscillator model, however, assigns two excitation quanta to the Roper resonance and only one excitation quantum to the states with negative parity. This failure in reproducing the spectrum of the nucleon correctly is common to all nucleon models. The Roper resonance either turns out too low or too high in energy. This motivates calculations from first principles as possible with lattice QCD. Results from such calculations might provide insight to the dynamics of the quarks inside the nucleon and thus favour one particular model or even lead to a new picture.

2.2 Baryons on the lattice – the nucleon operators

In Section 1.3 we have shown that correlation functions like (1.20) contain information about the energy levels of the inserted operators $\mathcal{O}$. Therefore, all we have to do for applying lattice QCD to hadron spectroscopy, is to define operators for the baryons under consideration. This section will introduce the nucleon interpolating fields[9] used in this work and explicitly derive the correlators in a form suitable for the lattice.

2.2.1 The set of operators

For this work, we are interested in the nucleon spectrum. To be more precise, we want to calculate the masses for the ground and first excited state of the positive and negative parity nucleon. So the states we are interested in are:

	$I(J^P)$		$I(J^P)$
$N(939)$	$\frac{1}{2}(\frac{1}{2}^+)$	$N(1535)$	$\frac{1}{2}(\frac{1}{2}^-)$
$N(1440)$	$\frac{1}{2}(\frac{1}{2}^+)$	$N(1650)$	$\frac{1}{2}(\frac{1}{2}^-)$

As for Table 2.2, J and P are total angular momentum and parity. I is the isospin of the particle. The quark content is (uud) for the proton and (udd) for the neutron. Nucleon interpolating fields $\mathcal{N}$ need to have the same quantum numbers as the physical particles and non-vanishing overlap with the particle states, i.e.

$$\langle 0|\,\mathcal{N}\,|\text{nucleon}\rangle \neq 0 \quad \text{and} \quad \big\langle \text{nucleon}|\,\bar{\mathcal{N}}\,|0\big\rangle \neq 0. \tag{2.12}$$

The choice of the interpolating fields is arbitrary to a large extent. One has to find the optimal operator with respect to the coupling (2.12) to the hadron in

[9] We use interpolating field or current synonymous for operator.

question. At the same time, we need an operator that can be evaluated without too much numerical effort. Therefore we will only consider local operators without derivative terms. One standard choice for the spin $\frac{1}{2}$ nucleon is [MM97]

$$\mathcal{N} = \epsilon_{cde} \left[u_c^{\mathrm{T}}(x)\, C\gamma_5\, d_d(x) - d_c^{\mathrm{T}}(x)\, C\gamma_5\, u_d(x) \right] u_e(x). \tag{2.13}$$

Here $C = \mathrm{i}\gamma_2\gamma_4$ is the charge conjugation matrix[10] and the indices c, d and e denote colour indices.[11] u and d are the quark fields for the respective flavours. Matrix notation is used for Dirac space where superscript T denotes transposition. The totally anti-symmetric tensor ϵ assures that we have a flavour singlet. To check that the operator in (2.13) indeed has the quantum numbers of the nucleon, we have to examine its symmetry and Dirac structure. Easiest to verify is the flavour content. It can be read off directly from the used quark fields. As the quark fields u and d both have spin $\frac{1}{2}$ and isospin $\frac{1}{2}$ the diquark part in square brackets of (2.13) is a singlet (due to the anti-symmetry in u and d) with spin $S = 0$ and $I = 0$. Hence, the total spin and isospin of the interpolating field (2.13) is $S = \frac{1}{2}$ and $I = \frac{1}{2}$ respectively, emerging from the third quark.

Using the anti-symmetry properties of ϵ and (A.13) we find the following:

$$\begin{aligned} &\epsilon_{cde} \left[u_c^{\mathrm{T}}(x)\, C\gamma_5\, d_d(x) - d_c^{\mathrm{T}}(x)\, C\gamma_5\, u_d(x) \right] u_e(x) \\ &\qquad = 2\epsilon_{cde} \left[u_c^{\mathrm{T}}(x)\, C\gamma_5\, d_d(x) \right] u_e(x). \end{aligned} \tag{2.14}$$

The factor of 2 can be dropped as it only changes the magnitude but not the functional behaviour of the two point function (1.20) which we use for extracting the mass. In this more compact form, spin and isospin content are not so explicit, but it is easier to implement. Instead of using only one interpolating field, we will apply a set of three different operators. All of them have the correct quantum numbers of the nucleon and they are widely used in the literature [Iof81, CDKS82, F$^+$82, Lei95, CJ97, Gup98, R$^+$02, MR03]:

$$\mathcal{N}_1(x) = \epsilon_{cde} \left[u_c^{\mathrm{T}}(x)\, C\gamma_5\, d_d(x) \right] u_e(x), \tag{2.15a}$$

$$\mathcal{N}_2(x) = \epsilon_{cde} \left[u_c^{\mathrm{T}}(x)\, C\, d_d(x) \right] \gamma_5\, u_e(x), \tag{2.15b}$$

$$\mathcal{N}_3(x) = \mathrm{i}\,\epsilon_{cde} \left[u_c^{\mathrm{T}}(x)\, C\gamma_4\gamma_5\, d_d(x) \right] u_e(x). \tag{2.15c}$$

Following the usual rules for 4-dimensional space-time, we find for the overlined operators:

$$\bar{\mathcal{N}}_1(x) = \epsilon_{cde} \left[\bar{u}_c(x)\, C\gamma_5\, \bar{d}_d^{\mathrm{T}}(x) \right] \bar{u}_e(x), \tag{2.16a}$$

$$\bar{\mathcal{N}}_2(x) = \epsilon_{cde} \left[\bar{u}_c(x)\, C\, \bar{d}_d^{\mathrm{T}}(x) \right] \bar{u}_e(x)\, \gamma_5, \tag{2.16b}$$

$$\bar{\mathcal{N}}_3(x) = \mathrm{i}\,\epsilon_{cde} \left[\bar{u}_c(x)\, C\gamma_4\gamma_5\, \bar{d}_d^{\mathrm{T}}(x) \right] \bar{u}_e(x). \tag{2.16c}$$

We use this set of interpolating fields instead of only one operator since any of the operators (2.15) (and similarly (2.16)) has a different overlap with ground and excited states of both parities. The optimal overlap with the physical state will be obtained with operators that are linear combinations of (2.15) and (2.16) respectively. How the determination of the optimal linear combination is implemented will be discussed in detail in Section 3.4.

[10] For a definition and some properties see Appendix A.2, equations (A.11) – (A.13).

[11] Einstein's summation convention again applies.

	$\mathcal{C}$	$\mathcal{P}$
$\psi(\boldsymbol{x},t)$	$C\,\bar{\psi}^{\mathrm{T}}(\boldsymbol{x},t)$	$\gamma_4\,\psi(-\boldsymbol{x},t)$
$\bar{\psi}(\boldsymbol{x},t)$	$-\psi^{\mathrm{T}}(\boldsymbol{x},t)\,C^{-1}$	$\bar{\psi}(-\boldsymbol{x},t)\,\gamma_4$

Table 2.3: Transformation properties of the quark and anti-quark fields ψ and $\bar{\psi}$ under charge conjugation $\mathcal{C}$ and parity $\mathcal{P}$.

2.2.2 Charge conjugation and parity transformation of the nucleon operators

With the transformation properties of the quark fields under $\mathcal{C}$ and $\mathcal{P}$ in Table 2.3 we will now show that all operators (2.15) transform in the same way under parity and charge conjugation, i.e. that they indeed couple to the same physical states. For the first interpolating field we find

$$\begin{aligned}\mathcal{N}_1(\boldsymbol{x},t) &\xrightarrow{\mathcal{P}} \epsilon_{cde}\,[u_c^{\mathrm{T}}(-\boldsymbol{x},t)\gamma_4^{\mathrm{T}}\,C\gamma_5\,\gamma_4 d_d(-\boldsymbol{x},t)]\,\gamma_4 u_e(-\boldsymbol{x},t)\\ &= \epsilon_{cde}\,[u_c^{\mathrm{T}}(-\boldsymbol{x},t)\,C\gamma_5\,\gamma_4\gamma_4\,d_d(-\boldsymbol{x},t)]\,\gamma_4 u_e(-\boldsymbol{x},t) = \gamma_4\,\mathcal{N}_1(-\boldsymbol{x},t).\end{aligned}$$

We have used the general properties of the gamma matrices for this result (c.f. Appendix A.2). Similarly we obtain for the other operators:

$$\begin{aligned}\mathcal{N}_2(\boldsymbol{x},t) &\xrightarrow{\mathcal{P}} \epsilon_{cde}\,[u_c^{\mathrm{T}}(-\boldsymbol{x},t)\gamma_4^{\mathrm{T}}\,C\,\gamma_4 d_d(-\boldsymbol{x},t)]\,\gamma_5\,\gamma_4 u_e(-\boldsymbol{x},t)\\ &= \epsilon_{cde}\,[u_c^{\mathrm{T}}(-\boldsymbol{x},t)\,C\,\gamma_4\gamma_4\,d_d(-\boldsymbol{x},t)]\,\gamma_4\gamma_5\,u_e(-\boldsymbol{x},t) = \gamma_4\,\mathcal{N}_2(-\boldsymbol{x},t),\end{aligned}$$

$$\begin{aligned}\mathcal{N}_3(\boldsymbol{x},t) &\xrightarrow{\mathcal{P}} \epsilon_{cde}\,[u_c^{\mathrm{T}}(-\boldsymbol{x},t)\gamma_4^{\mathrm{T}}\,C\gamma_4\gamma_5\,\gamma_4 d_d(-\boldsymbol{x},t)]\,\gamma_4 u_e(-\boldsymbol{x},t)\\ &= \epsilon_{cde}\,[u_c^{\mathrm{T}}(-\boldsymbol{x},t)\gamma_4\gamma_4\,C\gamma_4\gamma_5\,d_d(-\boldsymbol{x},t)]\,\gamma_4 u_e(-\boldsymbol{x},t) = \gamma_4\,\mathcal{N}_3(-\boldsymbol{x},t).\end{aligned}$$

We see that the operators $\mathcal{N}_i$ all transform in the same way. We will later find in Section 3.2 that they couple to both, positive and negative parity states. So the interpolating fields (2.15) can in general be used to calculate all nucleon states we are looking for.

In an analogous way we derive the transformation properties under charge conjugation:

$$\begin{aligned}\mathcal{N}_1(x) &\xrightarrow{\mathcal{C}} \epsilon_{cde}\,\left[\bar{u}_c(x)C^{\mathrm{T}}\,C\gamma_5\,C\bar{d}_d^{\mathrm{T}}(x)\right]C\bar{u}_e^{\mathrm{T}}(x)\\ &= -\,\epsilon_{cde}\,\left[\bar{u}_c(x)\,C\gamma_5\,\bar{d}_d^{\mathrm{T}}(x)\right]C\bar{u}_e^{\mathrm{T}}(x) = -C\,\bar{\mathcal{N}}_1^{\mathrm{T}}(x),\end{aligned}$$

$$\begin{aligned}\mathcal{N}_2(x) &\xrightarrow{\mathcal{C}} \epsilon_{cde}\,\left[\bar{u}_c(x)C^{\mathrm{T}}\,C\,C\bar{d}_d^{\mathrm{T}}(x)\right]\gamma_5\,C\bar{u}_e^{\mathrm{T}}(x)\\ &= -\,\epsilon_{cde}\,\left[\bar{u}_c(x)\,C\,\bar{d}_d^{\mathrm{T}}(x)\right]C\gamma_5\,\bar{u}_e^{\mathrm{T}}(x)\\ &= -\,\epsilon_{cde}\,\left[\bar{u}_c(x)\,C\,\bar{d}_d^{\mathrm{T}}(x)\right]C(\bar{u}_e(x)\,\gamma_5)^{\mathrm{T}} = -C\,\bar{\mathcal{N}}_2^{\mathrm{T}}(x),\end{aligned}$$

$$\begin{aligned}\mathcal{N}_3(x) &\xrightarrow{\mathcal{C}} \epsilon_{cde}\,\left[\bar{u}_c(x)C^{\mathrm{T}}\,C\gamma_4\gamma_5\,C\bar{d}_d^{\mathrm{T}}(x)\right]C\bar{u}_e^{\mathrm{T}}(x)\\ &= -\,\epsilon_{cde}\,\left[\bar{u}_c(x)\,C\gamma_4\gamma_5\,\bar{d}_d^{\mathrm{T}}(x)\right]C\bar{u}_e^{\mathrm{T}}(x) = -C\,\bar{\mathcal{N}}_3^{\mathrm{T}}(x).\end{aligned}$$

Again we find that all operators transform in the same way under charge conjugation. We also see that apart from a phase factor the nucleon operators transform like Dirac fields (see Table 2.3). This is expected since the diquark part includes a trace over Dirac indices whereas the quark still has a free index.

2.3 The lattice two-point correlation function

We now compute the two point function of the nucleon that will be put on the lattice. For a more compact notation, we use an interpolating field with general Dirac structure Γ and Γ'. The operators then read

$$\begin{aligned} \mathcal{N}_i(x) &= \epsilon_{cde} \left[u_c^{\mathrm{T}}(x)\, \Gamma_i\, d_d(x)\right] \Gamma'_i\, u_e(x), \\ \bar{\mathcal{N}}_i(x) &= \epsilon_{cde} \left[\bar{u}_c(x)\, \Gamma_i\, \bar{d}_d^{\mathrm{T}}(x)\right] \bar{u}_e(x)\, \Gamma'_i, \\ &\text{with } i = 1, 2, 3. \end{aligned} \tag{2.17}$$

To obtain our set of operators (2.15) and (2.16), the choice of the Γ-matrices is the following:

$$\Gamma_1 = C\gamma_5 \qquad \Gamma'_1 = 1, \tag{2.18a}$$

$$\Gamma_2 = C \qquad \Gamma'_2 = \gamma_5, \tag{2.18b}$$

$$\Gamma_3 = \mathrm{i}C\gamma_4\gamma_5 \qquad \Gamma'_3 = 1. \tag{2.18c}$$

The correlation function we are interested in propagates the nucleon from $(\mathbf{0}, 0)$ to $(\boldsymbol{x}, t)$. We also consider cross correlations between the $\mathcal{N}_i$, hence the general form of our correlation function is

$$C_{ij}(\boldsymbol{x}, t) = \left\langle \mathcal{N}_i(\boldsymbol{x}, t)\, \bar{\mathcal{N}}_j(\mathbf{0}, 0) \right\rangle, \tag{2.19}$$

with $i, j = 1, 2, 3$. Note that that our interpolating fields have a spinor structure and thus C_{ij} is a tensor-like object for any combination i, j. Writing Dirac indices explicitly and using (2.17), this reads

$$\begin{aligned} C_{ij}(\boldsymbol{x}, t)_{\alpha\alpha'} = {} & \epsilon_{cde}\epsilon_{c'd'e'} (\Gamma'_i)_{\alpha\beta} (\Gamma_i)_{\gamma\delta} (\Gamma'_j)_{\alpha'\beta'} (\Gamma_j)_{\gamma'\delta'} \times \\ & \left\langle u_{\beta c}(\boldsymbol{x}, t)\, u_{\gamma d}(\boldsymbol{x}, t)\, d_{\delta e}(\boldsymbol{x}, t)\, \bar{u}_{\beta' c'}(\mathbf{0}, 0)\, \bar{u}_{\gamma' d'}(\mathbf{0}, 0)\, \bar{d}_{\delta' e'}(\mathbf{0}, 0) \right\rangle. \end{aligned} \tag{2.20}$$

An illustration of this correlator in form of a quark line diagram can be seen in Figure 2.1. The fermionic contractions can be evaluated using Wick's theorem

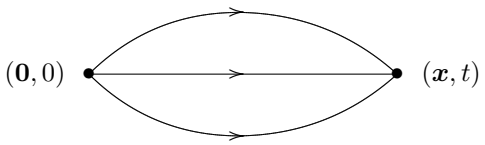

Figure 2.1: The quark line graph for the two-point function.

(1.63) after anti-commuting the quark fields appropriately:

$$\begin{aligned} C_{ij}(\boldsymbol{x},t)_{\alpha\alpha'} &= -\epsilon_{cde}\epsilon_{c'd'e'}(\Gamma_i')_{\alpha\beta}(\Gamma_i)_{\gamma\delta}(\Gamma_j')_{\alpha'\beta'}(\Gamma_j)_{\gamma'\delta'} \times \\ &\quad \left\langle u_{\beta c}(\boldsymbol{x},t)\bar{u}_{\beta' c'}(\mathbf{0},0)u_{\gamma d}(\boldsymbol{x},t)\bar{u}_{\gamma' d}(\mathbf{0},0)d_{\delta e}(\boldsymbol{x},t)\bar{d}_{\delta' e'}(\mathbf{0},0)\right\rangle \\ &= -\epsilon_{cde}\epsilon_{c'd'e'}(\Gamma_i')_{\alpha\beta}(\Gamma_i)_{\gamma\delta}(\Gamma_j')_{\alpha'\beta'}(\Gamma_j)_{\gamma'\delta'} \times \\ &\quad \Big\langle \big[\mathcal{D}^{-1}_{\beta c,\beta' c'}(\boldsymbol{x},t,\mathbf{0},0)\mathcal{D}^{-1}_{\gamma d,\gamma' d'}(\boldsymbol{x},t,\mathbf{0},0) \\ &\quad - \mathcal{D}^{-1}_{\beta c,\gamma' d'}(\boldsymbol{x},t,\mathbf{0},0)\mathcal{D}^{-1}_{\gamma d,\beta' c'}(\boldsymbol{x},t,\mathbf{0},0)\big]\mathcal{D}^{-1}_{\delta e,\delta' e'}(\boldsymbol{x},t,\mathbf{0},0)\Big\rangle_G. \end{aligned} \tag{2.21}$$

The leading minus sign is due to the different ordering of the quark fields. We have omitted flavour indices for the Dirac propagator $\mathcal{D}^{-1}$ as we assume $m_u = m_d$. The index G again abbreviates the remaining gauge integration from the path integral (1.62). With (2.21) we derived the correlation functions that can be implemented on the lattice. From the simulation we then obtain data sets that we compare to the behaviour (1.21) in Hilbert space.

Chapter 3

Technicalities

The focus of this chapter is to explain the technical details of the simulation that are essential for extracting the results. This incorporates lattice techniques as well as statistical methods.

We begin with common techniques to project to definite momentum and parity. The former is necessary since energy levels as in (1.21) always involve the mass of the particle and some kinetic part whereas we are only interested in the rest mass. The latter is important because our operators cannot distinguish between positive and negative parity states. To circumvent this unwanted mixing we need to project on a definite parity.

Another lattice technique used in this work is Jacobi smearing [A$^+$93, B$^+$97, AGJ$^+$94]. By this term one refers to the 'smearing' of the wave function at the source and sometimes also at the sink of the propagator, which leads to a more realistic wave function.

The previous chapter introduced a set of nucleon operators. To find the optimal linear combination of those, we use a variational method [LW90]. This method also simplifies the fitting function necessary to obtain the masses of the particles.

The last two sections of this chapter discuss the actual fitting procedure. This involves so-called effective mass plots and least squares fitting. In order to improve the statistics of our data, we used the jackknife method. This method is also important for the calculation of statistical errors for our results.

3.1 Momentum projection

Our goal is to identify the mass spectrum of the nucleon. We therefore calculate correlation functions like (2.19) and identify them with a sum of exponentials (1.21). The time dependence of these exponentials then contains the information about the energy spectrum of the correlator. The relativistic energy-momentum relation[1]

$$E^2 = m^2 + \boldsymbol{p}^2 \tag{3.1}$$

then yields the rest mass m of the state, where in (3.1) E and $\boldsymbol{p}$ are the energy and momentum of the particle. Note that $\boldsymbol{p}$ only assumes discrete values on the

[1] We use 'natural' units where $c = 1$.

lattice:[2]

$$\boldsymbol{p} = \frac{2\pi}{N}\boldsymbol{n}\,, \quad n^i = 0, 1, \ldots, N-1,\ i = 1, 2, 3. \tag{3.2}$$

From (3.1) we see that we have to know the momentum $\boldsymbol{p}$ of the state to extract its mass. The correlation function on the other hand incorporates particles propagating from $(\mathbf{0}, 0)$ to $(\boldsymbol{x}, t)$ with all kinds of momenta. Thus we need to project our states to a definite momentum $\boldsymbol{p}$. The basic idea to achieve this, is to Fourier transform the correlation function.

Let the Fourier transform of an operator $\mathcal{O}$ and its inverse be defined by:

$$\begin{aligned} \mathcal{O}^{\mathrm{P}}(\boldsymbol{p}, t) &= \frac{1}{N^{3/2}} \sum_{\boldsymbol{x}} e^{-\mathrm{i}\boldsymbol{p}\boldsymbol{x}}\, \mathcal{O}(\boldsymbol{x}, t)\,, \\ \mathcal{O}(\boldsymbol{x}, t) &= \frac{1}{N^{3/2}} \sum_{\boldsymbol{p}} e^{\mathrm{i}\boldsymbol{p}\boldsymbol{x}}\, \mathcal{O}^{\mathrm{P}}(\boldsymbol{p}, t)\,. \end{aligned} \tag{3.3}$$

We can insert this into (2.19) and write our source and sink operators as Fourier sums

$$\begin{aligned} C_{ij}(\boldsymbol{x}, t) &= \left\langle \mathcal{N}_i(\boldsymbol{x}, t)\, \bar{\mathcal{N}}_j(\mathbf{0}, 0) \right\rangle \\ &= \frac{1}{N^3} \sum_{\boldsymbol{q}, \boldsymbol{q}'} e^{-\mathrm{i}\boldsymbol{q}\boldsymbol{x}} \left\langle \mathcal{N}_i^{\mathrm{P}}(\boldsymbol{q}, t)\, \bar{\mathcal{N}}_j^{\mathrm{P}}(\boldsymbol{q}', 0) \right\rangle . \end{aligned} \tag{3.4}$$

If we now evaluate the correlator (3.4) similar to (1.21) we obtain

$$\begin{aligned} &\frac{1}{Z}\frac{1}{N^3} \sum_{n,m=0}^{\infty} \sum_{\boldsymbol{q}, \boldsymbol{q}'} e^{-\mathrm{i}\boldsymbol{q}\boldsymbol{x}} \langle n | \mathcal{N}_i^{\mathrm{P}}(\boldsymbol{q}, t) | m \rangle\, \mathrm{e}^{-E_m t} \left\langle m | \bar{\mathcal{N}}_j^{\mathrm{P}}(\boldsymbol{q}', 0) | n \right\rangle \mathrm{e}^{-E_n (T-t)} \\ &= \frac{1}{Z}\frac{1}{N^3} \sum_{\boldsymbol{q}', \boldsymbol{q}} e^{-\mathrm{i}\boldsymbol{q}\boldsymbol{x}} \Big(\langle 0 | \mathcal{N}_i^{\mathrm{P}}(\boldsymbol{q}, t) | \boldsymbol{q}, i \rangle \left\langle \boldsymbol{q}, i | \bar{\mathcal{N}}_j^{\mathrm{P}}(\boldsymbol{q}', 0) | 0 \right\rangle \mathrm{e}^{-E_{\boldsymbol{q}, i} t} \\ &\qquad + \langle \boldsymbol{q}', j | \mathcal{N}_i^{\mathrm{P}}(\boldsymbol{q}, t) | 0 \rangle \left\langle 0 | \bar{\mathcal{N}}_j^{\mathrm{P}}(\boldsymbol{q}', 0) | \boldsymbol{q}', j \right\rangle \mathrm{e}^{-E_{\boldsymbol{q}', j}(T-t)} + \ldots \Big) \end{aligned} \tag{3.5}$$

with

$$Z = 1 + \mathrm{e}^{-E_1 T} + \mathrm{e}^{-E_2 T} + \cdots\ .$$

Here $|\boldsymbol{q}, i\rangle$, $|\boldsymbol{q}', j\rangle$ are the lowest states in energy to the operators $\mathcal{N}_i^{\mathrm{P}}(\boldsymbol{q}, t)$ and $\bar{\mathcal{N}}_j^{\mathrm{P}}(\boldsymbol{q}', 0)$ with their momenta explicitly specified. Their corresponding energies are $E_{\boldsymbol{q}, i}$ and $E_{\boldsymbol{q}', j}$. Note that all operators are constructed to have overlap with the nucleon, thus the matrix elements may be non-vanishing even for $i \neq j$. On the other hand we see that the matrix elements in (3.5) are non-vanishing only for $\boldsymbol{q} = \boldsymbol{q}'$, so that we finally get

$$\begin{aligned} &\frac{1}{Z} \sum_{\boldsymbol{q}} e^{\mathrm{i}\boldsymbol{q}\boldsymbol{x}} \Big(\langle 0, i | \mathcal{N}_i^{\mathrm{P}}(\boldsymbol{q}, t) | \boldsymbol{q}, i \rangle \left\langle \boldsymbol{q}, i | \bar{\mathcal{N}}_j^{\mathrm{P}}(\boldsymbol{q}, 0) | 0, i \right\rangle \mathrm{e}^{-E_{\boldsymbol{q}, i} t} \\ &\qquad + \langle \boldsymbol{q}, j | \mathcal{N}_i^{\mathrm{P}}(\boldsymbol{q}, t) | 0, j \rangle \left\langle 0, j | \bar{\mathcal{N}}_j^{\mathrm{P}}(\boldsymbol{q}, 0) | \boldsymbol{q}, j \right\rangle \mathrm{e}^{-E_{\boldsymbol{q}, j}(T-t)} + \ldots \Big). \end{aligned} \tag{3.6}$$

We have dropped the constant volume factor $1/N^3$ which is absorbed in the pre-factor and does not alter the exponential decay we are interested in. We

[2] Also see Appendix A.4.

now Fourier transform the correlator (3.6) and find (again dropping all volume factors)

$$\begin{aligned} C_{ij}(\boldsymbol{p},t)^{\mathrm{P}} &= \sum_{\boldsymbol{x}} \mathrm{e}^{-\mathrm{i}\boldsymbol{p}\boldsymbol{x}}\, C_{ij}(\boldsymbol{x},t) \\ &= \langle 0,i|\mathcal{N}_i^{\mathrm{P}}(\boldsymbol{p},t)|\boldsymbol{p},i\rangle \left\langle \boldsymbol{p},i|\bar{\mathcal{N}}_j^{\mathrm{P}}(\boldsymbol{p},0)|0,i\right\rangle \mathrm{e}^{-E_{\boldsymbol{p},i}t} \\ &+ \langle \boldsymbol{p},j|\mathcal{N}_i^{\mathrm{P}}(\boldsymbol{p},t)|0,j\rangle \left\langle 0,j|\bar{\mathcal{N}}_j^{\mathrm{P}}(\boldsymbol{p},0)|\boldsymbol{p},j\right\rangle \mathrm{e}^{-E_{\boldsymbol{p},j}(T-t)} + \dots . \end{aligned} \tag{3.7}$$

Equation (3.7) then is our two-point correlation function with definite momentum $\boldsymbol{p}$ of the particle states. Thus to extract the particle rest mass from the correlator (3.7) we have to set $\boldsymbol{p} = 0$, i.e. we sum over all lattice sites. This projects to zero momentum suitable for (3.1). We will drop the superscript P from now on since the sum indicates the Fourier transform and write $C_{ij}(t)$ instead.

3.2 Parity projection

We have already mentioned that our set of operators couples to both, positive and negative parity states [SBO02]. In this section we will verify that this is indeed the case and also show how this can be dealt with in the calculation of the correlation function.

We have seen in Section 2.2.2 that the nucleon operators (2.15) transform like spinors

$$\mathcal{N}_i(\boldsymbol{x},t) \quad \xrightarrow{\mathcal{P}} \quad +\gamma_4\, \mathcal{N}_i(-\boldsymbol{x},t). \tag{3.8}$$

By multiplying the operators with γ_5 from the left, we obtain interpolation fields that transform alike but with a relative sign (use (A.9))

$$\gamma_5\, \mathcal{N}_i(\boldsymbol{x},t) \quad \xrightarrow{\mathcal{P}} \quad -\gamma_4\, \gamma_5\, \mathcal{N}_i(-\boldsymbol{x},t). \tag{3.9}$$

Following standard nomenclature [MM97, SBO02], the sets of operators are constructed to have positive (3.8) and negative (3.9) parity. Denoting the correlator (2.19) with C_{ij} if it includes interpolating fields as in (3.8) and with C_{ij}^5 in the case of operators like (3.9), we find

$$C_{ij}(t) = -\gamma_5\, C_{ij}^5(t)\, \gamma_5\,. \tag{3.10}$$

The important point to note about this relation between the correlators is that it shows that our set of operators (2.15) couples to *both* parities. To project onto definite parity, we define the projection operator $P^{\pm}$

$$P^{\pm} \equiv \frac{1}{2}(1 \pm \gamma_4). \tag{3.11}$$

Operators in momentum space multiplied with this projector are parity eigenstates if we have $\boldsymbol{p} = 0$, as can easily be verified

$$\begin{aligned} \sum_{\boldsymbol{x}} \mathcal{N}_i^{\pm}(\boldsymbol{x},t) = \sum_{\boldsymbol{x}} P^{\pm}\mathcal{N}_i(\boldsymbol{x},t) \quad \xrightarrow{P} \quad & \sum_{\boldsymbol{x}} \frac{1}{2}(1 \pm \gamma_4)\gamma_4 \mathcal{N}_i(-\boldsymbol{x},t) \\ & = \pm \sum_{\boldsymbol{x}'} \frac{1}{2}(1 \pm \gamma_4)\mathcal{N}_i(\boldsymbol{x}',t) \\ & = \pm \sum_{\boldsymbol{x}} \mathcal{N}_i^{\pm}(\boldsymbol{x},t). \end{aligned} \tag{3.12}$$

The sum over $\boldsymbol{x}$ here is the Fourier transform for momentum $\boldsymbol{p} = 0$. Between the first and second line of (3.12) we absorb the relative sign in the coordinates (due to the parity transformation) in the summation over all sites. Using the projection operator $P^{\pm}$ we can now write down the two-point correlation function with definite momentum $\boldsymbol{p} = 0$ and definite parity

$$C_{ij}^{\pm}(t) = \sum_{\boldsymbol{x}} \left\langle P^{\pm} \mathcal{N}_i(\boldsymbol{x}, t) \bar{\mathcal{N}}_j(\boldsymbol{0}, 0) \right\rangle . \tag{3.13}$$

Note that it is sufficient to project one operator. Another way of finding the projection onto definite parity is evaluating the correlation function using a summation over all spin states for the matrix elements. The general form of the correlation function (2.19) then is [F+82, MM97, SBO02]

$$C_{ij}(t) = (1 + \gamma_4) A \mathrm{e}^{-Et} + (1 - \gamma_4) A \mathrm{e}^{-E(T-t)} + \dots , \tag{3.14}$$

where we have suppressed higher terms. A is proportional to the coupling between the interpolating operators and the second term is the anti-particle propagating backward in time. The Dirac structure $(1 \pm \gamma_4)$ can be motivated by looking at solutions to the free Dirac equation. Let ψ_s be such a solution with spin s, the sum over all spins then yields [PS95]

$$\sum_s \psi_s \bar{\psi}_s = \gamma \cdot p \pm m = (\gamma_4 \pm 1) m + \boldsymbol{\gamma} \cdot \boldsymbol{p}, \tag{3.15}$$

where $+$ is for particles and $-$ for anti-particles respectively. Note again that we need zero spatial momentum for our choice of the projection operator. Our correlator (2.19) contains a similar term for our vector-like interpolating operators. Since the sign of γ_4 is reversed for negative parity states, our operators, including both parities, couple to (compare (3.10))

$$\begin{aligned} C_{ij}(t) = {} & (1 + \gamma_4) A^{+} \mathrm{e}^{-E^{+}t} + (1 - \gamma_4) A^{+} \mathrm{e}^{-E^{+}(T-t)} \\ & + (1 - \gamma_4) A^{-} \mathrm{e}^{-E^{-}t} + (1 + \gamma_4) A^{-} \mathrm{e}^{-E^{-}(T-t)} + \dots . \end{aligned} \tag{3.16}$$

Here the indices $+$ and $-$ denote positive and negative parity contributions. Thus by applying the projection operator we pick up states of opposite intrinsic parities propagating forward and backward in time. In this work we will always consider positive parity states in the forward time direction and extract the states of opposite parity by fixing the direction of propagation. Hence the correlation function we find on the lattice will be

$$\sum_{\boldsymbol{x}} \left\langle P^{+} \mathcal{N}_i(\boldsymbol{x}, t) \bar{\mathcal{N}}_j(\boldsymbol{0}, 0) \right\rangle = (1 + \gamma_4) A^{+} \mathrm{e}^{-E^{+}t} + (1 + \gamma_4) A^{-} \mathrm{e}^{-E^{-}(T-t)} + \dots . \tag{3.17}$$

The correlation function that will ultimately be used is obtained by taking the trace of (3.17) in Dirac space. This scalar quantity then reads

$$\sum_{\boldsymbol{x}} \mathrm{Tr} \left\langle P^{+} \mathcal{N}_i(\boldsymbol{x}, t) \bar{\mathcal{N}}_j(\boldsymbol{0}, 0) \right\rangle = 4 A^{+} \mathrm{e}^{-E^{+}t} + 4 A^{-} \mathrm{e}^{-E^{-}(T-t)} + \dots . \tag{3.18}$$

The l.h.s. is implemented on the lattice for simulation. The r.h.s. of (3.18) is the expected time dependent signal in the obtained data sets.

3.3 Smearing of quark fields

Physical baryons are not point-like but rather have an extension of the order of 1 fm. However, our interpolating fields (2.15) discussed so far are point-like, local fields only. We considered the interpolating fields in terms of their flavour, spin and isospin content but did not take into account the spatial structure of the baryons. This reduces the overlap between the operators and the physical states and thus decreases the signal to noise ratio. One possibility to have better overlap of the nucleon operators and their states would be to use non-local interpolating fields:

$$\mathcal{N}_i(x,y,z) = \epsilon_{cde} \sum_{\boldsymbol{x},\boldsymbol{y},\boldsymbol{z}} \varphi(\boldsymbol{x},\boldsymbol{y},\boldsymbol{z}) \left[u_c^{\mathrm{T}}(\boldsymbol{x},t)\, \Gamma_i\, d_d(\boldsymbol{y},t)\right] \Gamma_i'\, u_e(\boldsymbol{z},t), \tag{3.19}$$

where $\varphi(\boldsymbol{x},\boldsymbol{y},\boldsymbol{z})$ is the true nucleon wave function. Using delta functions for $\varphi(\boldsymbol{x},\boldsymbol{y},\boldsymbol{z}) = \delta(\boldsymbol{x}-\boldsymbol{y})\,\delta(\boldsymbol{y}-\boldsymbol{z})$, we recover the original set of operators. As we do not know the wave function in (3.19), we attempt to approximate it by smearing the quark fields. That is the quark fields are no longer point-like but instead localised around the lattice site $(\boldsymbol{x},t)$ in a spatial region of radius r, i.e. distributed over a range of lattice sites.

We use the gauge covariant Jacobi smearing [A$^+$93, AGJ$^+$94, B$^+$97] to avoid the gauge-fixing problem. This method smears the quark field in a plane at $x_4 = t$

$${}^S\psi(\boldsymbol{x},t) = \sum_{\boldsymbol{y}} {}^S H(\boldsymbol{x},\boldsymbol{y},U,t)\psi(\boldsymbol{y},t), \tag{3.20}$$

where H is the smearing kernel and S is the smearing label (S for smeared or P for point-like). H is chosen to be gauge covariant and hermitian

$${}^S H^\dagger = {}^S H. \tag{3.21}$$

The smeared anti-quark fields are defined as

$${}^S\bar{\psi}(\boldsymbol{x},t) = \sum_{\boldsymbol{y}} \bar{\psi}(\boldsymbol{y},t)\, {}^S H(\boldsymbol{y},\boldsymbol{x},U,t). \tag{3.22}$$

Our smeared propagator then reads

$${}^{S'S}\mathcal{D}^{-1}(\boldsymbol{y},t,\boldsymbol{x},0) = \sum_{\boldsymbol{x}',\boldsymbol{y}'} {}^{S'} H(\boldsymbol{y},\boldsymbol{y}',U,t)\, \mathcal{D}^{-1}(\boldsymbol{y}',t,\boldsymbol{x}',0)\, {}^S H(\boldsymbol{x}',\boldsymbol{x},U,0). \tag{3.23}$$

Note that we can have different smearing for source and sink fields, thus $S' = P$ is also possible.

The practical implementation of the smearing is done by applying a truncated Jacobi iterative solution to the Klein-Gordon equation [A$^+$93]. The kernel ${}^S H$ then reads

$$\begin{aligned} {}^S H(\boldsymbol{x},\boldsymbol{y},U,t) &= \sum_{j=0}^{N_{\mathrm{smear}}} \kappa^j \big(K(\boldsymbol{x},\boldsymbol{y},t)\big)^j, \\ K(\boldsymbol{x},\boldsymbol{y},t) &= \sum_{\mu=1}^{3} \left[U_\mu(\boldsymbol{x},t)\delta_{\boldsymbol{x}+\mu,\boldsymbol{y}} + U_{-\mu}(\boldsymbol{x},t)\delta_{\boldsymbol{x}-\mu,\boldsymbol{y}}\right]. \end{aligned} \tag{3.24}$$

β_1	N_{smear}	κ
7.90	18	0.21
8.35	32	0.21

Table 3.1: Listing of the smearing parameters N_{smear} and κ used for our lattices.

N_{smear} is the number of iterations and, being increased, increases the size of the smeared object. The second parameter in (3.24), κ, controls the coarseness of the iteration. Both parameters are used to tune the average radius r of the smeared quark fields and depend on the lattice constant a. We define the radius r as

$$r^2 = \frac{\sum_{\boldsymbol{x}} (\boldsymbol{x}-\boldsymbol{y})^2 \, |{}^S H(\boldsymbol{x},\boldsymbol{y},U,t)|^2}{|{}^S H(\boldsymbol{x},\boldsymbol{y},U,t)|^2}. \tag{3.25}$$

The radius r describes the width of the quark wave function and we keep r at the value of $r \sim 0.35$ fm for all lattice spacings. The corresponding values for the parameters N_{smear} and κ used in our simulation can be found in Table 3.1. The final source is approximately Gaussian with a width of $2r = 0.7$ fm.

3.4 The variational method

We have introduced a set of operators (2.15) in Section 2.2.1 and discussed that these interpolating fields couple to ground and excited states of the nucleon. The 2-point functions of these operators have been used to extract the low energy spectrum of the nucleon with the so-called Maximum-Entropy Method (MEM) [Y$^+$02, SSHA03] or with Bayesian priors [L$^+$03]. Also common are multi-exponential fits [R$^+$02, MR03] or using a variational approach [B$^+$03, M$^+$03].

The MEM is a fitting technique based on Bayesian probabilities [L$^+$02]. The masses of the particles are extracted from a reconstructed spectral distribution function. Although MEM has proven to be quite powerful when reconstructing Fourier series [Ski89], it is unclear how reliable it is for spectra in lattice QCD since the results seem to depend crucially on the prior knowledge entering the fit [Lan, Mor03].

The other approaches rely on fitting the correlation function (3.18) to the data sets. The correlation function usually is a superposition of the various states contributing. In case of the method using Bayesian priors, a constrained fitting technique is again applied [Mor02, L$^+$02]. Here one starts with fitting the ground state where a clear signal is obtained in its asymptotic region. This result is then used as a prior to a fit including also excited states.

Multi-exponential fits attempt to find the ground and excited states simultaneously, i.e. a double exponential fit is applied to find the two lowest states. This approach is difficult since the higher masses lead to a faster decay of the Euclidean propagator, resulting in short fit ranges for the excited state, limited to small times t. Thus multi-exponential fits have a bad signal to noise ratio for the excited states. Single exponential fits are more easy to control but require separate data sets for each particle mass to be fitted. This implies nucleon

interpolating fields with a clear overlap to one state only. At this point, the variational approach enters.

The variational method [MT83, LW90] is used to disentangle the physical states and provides data sets with mainly one contribution. This disentanglement will also give the optimal linear combinations of our operators $\mathcal{N}$ (2.15) mentioned in Section 2.2.1. Denoting the optimal operators by $\tilde{\mathcal{N}}_\alpha$, the superposition we are looking for is

$$\tilde{\mathcal{N}}_\alpha = \sum_{i=1}^{r} c_i^\alpha \, \mathcal{N}_i. \tag{3.26}$$

In our case the truncation of the sum in (3.26) will appear at $r = 3$ due to the limited set of operators. The correlation function of the optimal operators is then related to the correlation function of the basis operators $\mathcal{N}_i$:

$$\begin{aligned} \tilde{C}_{\alpha\beta}(t) &= \sum_{\boldsymbol{x}} \left\langle \tilde{\mathcal{N}}_\alpha(\boldsymbol{x}, t) \, \bar{\tilde{\mathcal{N}}}_\beta(\mathbf{0}, 0) \right\rangle \\ &= \sum_{\boldsymbol{x}} \sum_{i,j} c_i^\alpha (c_j^\beta)^* \left\langle \mathcal{N}_i(\boldsymbol{x}, t) \, \bar{\mathcal{N}}_j(\mathbf{0}, 0) \right\rangle \\ &= \sum_{i,j} c_i^\alpha (c_j^\beta)^* \, C_{ij}(t). \end{aligned} \tag{3.27}$$

This corresponds to a change of basis of the operators in the correlation function (2.19). Note that we can limit ourselves to $\alpha = \beta$ since all other cross-correlations now vanish if the $\tilde{\mathcal{N}}_\alpha$ give good approximations of the physical states – physical operators for different states have vanishing overlap. The variational method ([MT83] and references therein) of finding the optimal operators can be derived from varying the coefficients c_i^α such that the ratio

$$R_\alpha(t, t_0) = \frac{\sum_{\boldsymbol{x}} \left\langle \tilde{\mathcal{N}}_\alpha(\boldsymbol{x}, t) \, \bar{\tilde{\mathcal{N}}}_\alpha(\mathbf{0}, 0) \right\rangle}{\sum_{\boldsymbol{x}} \left\langle \tilde{\mathcal{N}}_\alpha(\boldsymbol{x}, t_0) \, \bar{\tilde{\mathcal{N}}}_\alpha(\mathbf{0}, 0) \right\rangle} = \frac{\sum_{i,j} c_i^\alpha (c_j^\alpha)^* \, C_{ij}(t)}{\sum_{i,j} c_i^\alpha (c_j^\alpha)^* \, C_{ij}(t_0)} \tag{3.28}$$

is maximised. In the case when R_α is maximal, the state that is lowest in energy dominates the ratio for large t. t_0 is chosen close to 0. It is used for normalisation and can be varied to increase the signal to noise ratio. Using a vector notation this is equivalent to

$$\frac{\partial}{\partial c^\alpha} \frac{(c^\alpha)^{\mathrm{T}} C(t) (c^\alpha)^*}{(c^\alpha)^{\mathrm{T}} C(t_0) (c^\alpha)^*} = 0 \Longleftrightarrow C(t) \cdot (c^\alpha)^* = \frac{(c^\alpha)^{\mathrm{T}} C(t) (c^\alpha)^*}{(c^\alpha)^{\mathrm{T}} C(t_0) (c^\alpha)^*} \, C(t_0) \cdot (c^\alpha)^* \tag{3.29}$$

and corresponds to the generalised eigenvalue problem

$$C(t) \cdot v_\alpha = \lambda_\alpha(t) \, C(t_0) \cdot v_\alpha, \tag{3.30}$$

where λ_α are eigenvalues to the eigenvectors v_α and $C(t_0)$ is used as a normalisation matrix. Lüscher and Wolff have shown [LW90] that the eigenvalues $\lambda_\alpha(t)$ of the generalised eigenvalue problem (3.30) decay exponentially with the mass of the corresponding physical state as decay parameter. The eigenvalues are ordered such that $\lambda_1 \geq \lambda_2 \geq \cdots \geq \lambda_r$, we then have for $\alpha \leq r$

$$\lambda_\alpha(t) \overset{t \to \infty}{=} A_\alpha \mathrm{e}^{-E_\alpha (t - t_0)} \left[1 + \mathcal{O}(\mathrm{e}^{-\Delta E_\alpha (t - t_0)}) \right]. \tag{3.31}$$

The energies are ordered such that E_1 is the ground state energy, E_2 the first excited state energy e.t.c. Here ΔE_α is the difference to higher states in energy that are not taken into account. The proof to (3.31) can be found in [LW90]. Bearing in mind the backward propagating particles and projection to definite parity we have

$$\lambda_\alpha^+(t) = A_\alpha^+ \mathrm{e}^{-E_\alpha^+(t-t_0)} + A_\alpha^- \mathrm{e}^{-E_\alpha^-(T-t-t_0)}, \tag{3.32}$$

where higher order corrections are suppressed.

We have seen that by solving the generalised eigenvalue problem (3.30) our operators combine to 'physical' operators. We are then able to extract the masses for pure states. However, the number of initial interpolating fields $\mathcal{N}_i$ limits the number of physical states accessible (3.31). Hence we can only extract the ground state and the first excited state faithfully.

Note that not only the eigenvalues of the correlation matrix C_{ij} provide interesting information. From (3.29) and (3.30) we see that the components of the eigenvectors v_α can be identified with the coefficients of the superposition (3.26)

$$c_i^\alpha = (v_\alpha^*)_i. \tag{3.33}$$

We can thus find the decomposition of the optimal operators $\tilde{\mathcal{N}}_\alpha$ in terms of our set of operators $\mathcal{N}_i$. The mixing coefficients c_i^α to the physical operators can be used to infer the physics of the nucleon system. This will be addressed in Section 4.4.

3.5 Fitting techniques

We want to extract the baryon masses from the exponential fall-off (3.32) of the eigenvalues of the correlation matrix (3.18). The correlation functions $C_{ij}(t)$ are therefore measured over the full time extent T of the lattice. This is done for N gauge configurations U_n $(n = 1, 2, \ldots, N)$ obtained from Monte Carlo simulation. As explained in Sections 3.1 and 3.2 we apply a projection to definite momentum and parity. The variational method discussed in the previous section is then used to disentangle the physical states. That means we numerically solve the generalised eigenvalue problem (3.30). The resulting data sets are analysed during the fitting procedure.

3.5.1 The method of least squares

We use least squares fitting [Lyo91, H$^+$02] for our work. From the discussion in Section 3.4, we know that the fitting function λ_α is of exponential form (3.32) with two parameters A_α and E_α.[3] The numerically found eigenvalues from the variational approach are denoted with Λ_α. Assuming independent and Gaussian distributed data points, the method of maximum likelihood is equivalent to the least squares method. The latter minimises the χ^2-function

$$\chi^2 = \sum_{t=t_{\min}}^{t_{\max}} \frac{\big(\overline{\Lambda}_\alpha(t) - \lambda_\alpha(t)\big)^2}{\sigma_\alpha(t)^2}. \tag{3.34}$$

[3]Note that we apply the fit for positive and negative parity states separately. This is achieved by flipping the time direction $(T - t) \to \tilde{t}$. For brevity we drop the $\pm$ for the different states in the following.

Here σ_α and $\overline{\Lambda}_\alpha$ are the error and the mean value of the data points Λ_α.[4] The times $t_{\min}$ and $t_{\max}$ limiting the fit range are chosen such that only the asymptotic region of the exponential decay is considered. How the fit range is determined in order to have a good signal to noise ratio is discussed in Section 3.5.2. Although (3.34) also holds if the measurements Λ_α are not Gaussian distributed, it is no longer valid in case the data for different t is not independent. Our simulation provides independent data sets only for Monte Carlo time, i.e. the configurations U_n themselves are independent. However, the measurements are not independent with respect to the propagation in lattice time t. We therefore have to take the covariance matrix $(\mathrm{Cov})(t,t')$ into account

$$(\mathrm{Cov})(t,t') = \frac{1}{N(N-1)} \sum_{n=1}^{N} \left(\Lambda_\alpha^{(n)}(t) - \overline{\Lambda}_\alpha(t)\right) \left(\Lambda_\alpha^{(n)}(t') - \overline{\Lambda}_\alpha(t')\right). \quad (3.35)$$

The parameters A_α and E_α are then defined by minimising

$$\chi^2 = \sum_{t,t'} \left[\overline{\Lambda}_\alpha(t) - \lambda_\alpha(t)\right] (\mathrm{Cov})^{-1}(t,t') \left[\overline{\Lambda}_\alpha(t') - \lambda_\alpha(t')\right], \quad (3.36)$$

where t, t' are limited to the fit range. The quality of the two parameter fit can be seen from the value of χ^2 per degrees of freedom. Although ideally 0, a χ^2/d.o.f. that is too small can indicate large errors on the data sets. A χ^2/d.o.f. which is too large shows that the fit does not resemble the data. In general we expect the value of χ^2/d.o.f. in the order of 1. This should correspond to a fitted function λ_α within one σ_α of the measured data (as can be seen from (3.34)).

3.5.2 Effective masses

The two parameter fit (3.36) requires an appropriately chosen fit range from $t_{\min}$ to $t_{\max}$. This can neither be determined directly from the exponential decay (3.32) nor be set globally for all lattice sizes and quark masses used.

In general, the fit range should be as large as possible to cover many data points and use all information accessible. It should be limited to the asymptotic region of the exponential decay[5] but it should not include any contributions from higher states. We define an effective mass

$$m_{\mathrm{eff}}(t+1/2) \equiv \ln \left| \frac{\lambda_\alpha(t)}{\lambda_\alpha(t+1)} \right|. \quad (3.37)$$

Together with (3.32) we see that $m = m_{\mathrm{eff}}$ for only one state dominating the exponential decay. Thus the fit range is equivalent to a plateau in the effective mass plot, i.e. m_{eff} is time independent (see the r.h.s. of Figure 3.1). If the effective mass is still time dependent for small t, higher states still contribute. A time dependence for larger t is due to a bad signal to noise ratio.

In addition to inspecting the effective mass plots the χ^2/d.o.f. can also be used as a tool for finding the fit range. Values for χ^2/d.o.f. that are not reasonable can point to a wrong fit range.

[4] The exact definitions of mean value and variance are given in Section 3.6

[5] Note that our formulae are only exact in the limit $t, T \to \infty$.

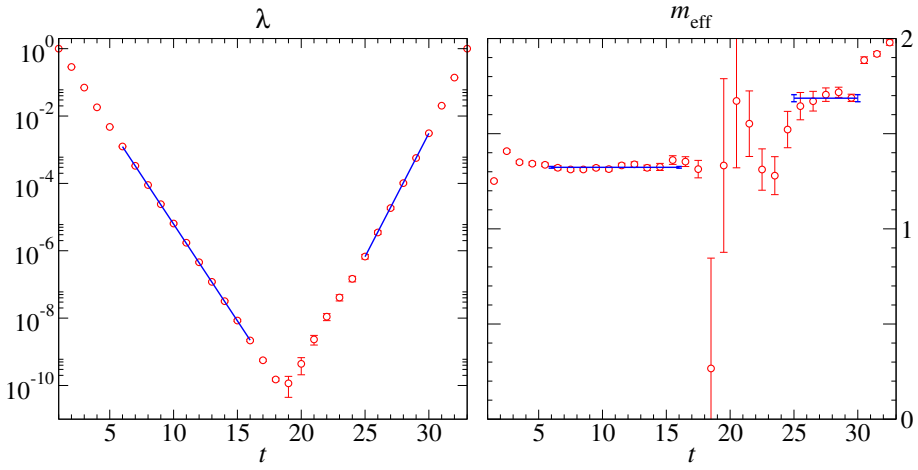

Figure 3.1: The l.h.s. shows an example plot for an eigenvalue λ (3.32). The r.h.s. is the corresponding effective mass plot. A plateau in this graph indicates the asymptotic region of (3.32) and thus the fit range. Also included as solid lines are possible fits to both parities with the corresponding fit ranges $(6\ldots16,\ 25\ldots30)$. $[16^3 \times 32$, $\beta_1 = 7.90$, $am_{\mathrm{q}} = 0.16$, smeared–smeared$]$

Using the variational method from Section 3.4, another approach for finding the fit range lies in inspecting the time behaviour of the eigenvectors v_α. For physical, undisturbed states these again need to be time independent. However, we did not find a significant difference for both methods. Hence we used the more common technique via the effective mass.

3.6 Calculation of errors with the jackknife method

We obtain our observables as parameters of least squares fits (3.36). The fits are applied to secondary quantities which are functions of averages $\overline{\Lambda}_\alpha$, i.e. the eigenvalues of the correlation matrix. In addition, the variance of the data also enters the fit and there is no naive way to obtain error estimates for the fit parameters. We need a method to obtain independent measurements that can each be used for fitting and thus be able to calculate statistical errors.

For primary quantities, directly obtained as averages, this can be circumvented using a method called binning, i.e. subsequent blocks of configurations are considered as bins and the bin averages are considered as independent measurements. However, this is not practicable for secondary quantities as we would need very large samples of data. Instead we use a *jackknife analysis* to obtain the masses and their corresponding uncertainties.

The jackknife analysis is a resampling technique where the statistical analysis is done on subsets of the original data. The subsets, called jackknife blocks, are obtained from the full set of data points by systematically omitting a number of

l samples. Let the set of the N independent measurements be $X_1, X_2, \ldots, X_N$. The jackknife blocks Y_i then are

$$Y_i \equiv (X_1, X_2, \ldots, X_{(i-1)l}, X_{il+1}, \ldots, X_N) \ , \quad i = 1, 2, \ldots, N^{\mathrm{j}},$$

where $N^{\mathrm{j}} = N/l$ is the number[6] of possible subsets. The secondary quantities θ are now determined on the subsets Y_i

$$\theta_i = \theta(Y_i).$$

The average value of the secondary quantity then is

$$\bar{\theta} = \frac{1}{N^{\mathrm{j}}} \sum_{i=1}^{N^{\mathrm{j}}} \theta_i \tag{3.38a}$$

with a variance defined by

$$S_\theta^2 = \frac{N^{\mathrm{j}} - 1}{N^{\mathrm{j}}} \sum_{i=1}^{N^{\mathrm{j}}} \Big(\theta_i - \bar{\theta} \Big)^2. \tag{3.38b}$$

In our case the secondary quantities θ are the fit parameters A_α and E_α from (3.32) and (3.36). Hence we fit (3.32) to all of the N^{j} jackknife blocks. Instead of using the simple average $\overline{\Lambda}_\alpha$ and the standard error $\sigma_\alpha = S/\sqrt{N}$ we have to compute the corresponding jackknife quantities

$$\overline{\Lambda}_\alpha^{(i)}(t) = \frac{1}{N^{\mathrm{j}}} \sum_{\Lambda_\alpha \in Y_{i,\alpha}} \Lambda_\alpha(t), \tag{3.39a}$$

and use these for fitting the parameters A_α and E_α for each jackknife block. Here the jackknife blocks Y_i contain $N - l$ measurements of $\Lambda_\alpha(t)$. The covariance matrix (3.35) changes in an analogous way to

$$(\mathrm{Cov})^{(i)}(t, t') = \frac{N^{\mathrm{j}} - 1}{N^{\mathrm{j}}} \sum_{\Lambda_\alpha \in Y_{i,\alpha}} \Big(\Lambda_\alpha(t) - \overline{\Lambda}_\alpha^{(i)}(t) \Big) \Big(\Lambda_\alpha(t') - \overline{\Lambda}_\alpha^{(i)}(t') \Big) . \tag{3.39b}$$

With equations (3.39), (3.32) and (3.36) we find N^{j} values for each parameter A_α and E_α. The result of the simulation will then be

$$\begin{aligned} A_\alpha^{\mathrm{sim}} &= \overline{A}_\alpha \pm S_A/\sqrt{N^{\mathrm{j}}} \quad \text{and} \\ E_\alpha^{\mathrm{sim}} &= \overline{E}_\alpha \pm S_E/\sqrt{N^{\mathrm{j}}} \end{aligned}$$

with (3.38a) and (3.38b). Note the difference between the parameters obtained from the subsets (3.38) and of the average (variance) of the jackknife blocks (3.39). Throughout this work we have used $l = 1$.

[6] N^{j} has to be an integer number, limiting the possibilities for l or in turn reducing the number of measurements in the full set to multiples of l (discarding some measurements).

Chapter 4

Results

The previous chapters have discussed all theoretical and some computational tools necessary to do a simulation in lattice QCD. This chapter will now present the results we obtained. All calculations are done in the quenched approximation using propagators that were generated with chirally improved fermions and the Lüscher-Weisz gauge action.

We start with a simple test, for simplicity limited to one operator only. We check that the exponential decay is reproduced and that the momentum projection works.

The next section presents the results for all cross-correlations of our set of operators, analysed with the variational approach. This is done for different lattices and for different kinds of smearing. Along with that, the results for the masses extracted from the exponential decay are presented.

Using the results obtained at different quark masses, we continue with chiral extrapolations for the states found. This is compared to the experimental values for the corresponding states.

We then interpret the content of the optimal operators in terms of the multiplet structure of baryons. Here the variational method provides the necessary information in form of mixing coefficients.

Naturally, the lattice technique has some limitations. Hence one section examines how strongly we suffer from finite size effects and how our results scale for different lattice sizes.

The last section will finally compare our results to other groups.

4.1 The pure $\mathcal{N}_1$–$\mathcal{N}_1$ correlator

We start the simulation with an exploratory test to see if we can control the techniques and tools described in the previous chapters. Instead of using all three operators (2.15) straight away, we limit the initial tests to one operator (2.15a) only. We use

$$\mathcal{N}_1(x) = \epsilon_{cde} \left[u_c^{\mathrm{T}}(x)\, C\gamma_5\, d_d(x) \right] u_e(x),$$

the most common operator for nucleon spectra. As mentioned in Section 3.2, we project onto definite parity with P^+ (3.11). Although our parity projection is only exact for zero momentum, we use different momenta to see if the momentum

projection (Section 3.1) is implemented correctly. The momenta we use are $\boldsymbol{p} = 2\pi/N \cdot \boldsymbol{n}$, where

$$\boldsymbol{n} = \begin{pmatrix}0\\0\\0\end{pmatrix}, \begin{pmatrix}1\\0\\0\end{pmatrix}, \begin{pmatrix}0\\1\\0\end{pmatrix}, \begin{pmatrix}0\\0\\1\end{pmatrix}, \begin{pmatrix}1\\1\\0\end{pmatrix}, \begin{pmatrix}1\\0\\1\end{pmatrix}, \begin{pmatrix}0\\1\\1\end{pmatrix}, \begin{pmatrix}1\\1\\1\end{pmatrix}, \begin{pmatrix}2\\0\\0\end{pmatrix}, \begin{pmatrix}0\\2\\0\end{pmatrix}, \begin{pmatrix}0\\0\\2\end{pmatrix}.$$

Thus the correlation function calculated is

$$C_{11}(t) = \sum_{\boldsymbol{x}} \mathrm{e}^{-\mathrm{i}\boldsymbol{p}\boldsymbol{x}} \operatorname{Tr} \left\langle P^{+}\, \mathcal{N}_1(\boldsymbol{x}, t)\, \bar{\mathcal{N}}_1(\boldsymbol{0}, 0) \right\rangle . \tag{4.1}$$

Note that the configurations are such that Jacobi smearing (Section 3.3) is always applied to the source and can be turned on or off for the sink of the correlation function.

Calculations are done at two different β-values and two different lattice sizes given in Table D.1. The number of bare quark masses m_{q} and configurations available are summarised in Table D.2. The following analysis is done with the jackknife method treating the correlation functions for every configuration as independent measurements (Section 3.6). Errors given are jackknife errors for $l = 1$. The results are consistent for all lattices. Examples below are for lattice size $16^3 \times 32$ with $\beta_1 = 7.90$ and point-like sinks.

4.1.1 Exponential decay and effective masses

The correlation function (4.1) is expected to have a functional form like

$$A^{+}\mathrm{e}^{-E^{+}t} + A^{-}\mathrm{e}^{-E^{-}(T-t)} + \ldots ,$$

where we have suppressed higher orders. The energies E^{+} and E^{-} should differ and depend on the momentum we project to. This can clearly be seen from the l.h.s. of Figure 4.1. The mass difference between positive and negative parity states results in an asymmetry of the correlation function.[1] In addition, higher energies due to higher momenta cause a different slope of the correlation function. The slope is steeper for higher momentum. Going to lower bare quark masses m_{q}, the signal becomes less pronounced. In addition, the errors on the measurements increase. Both can be seen comparing the upper ($am_{\mathrm{q}} = 0.20$) and lower ($am_{\mathrm{q}} = 0.04$) plots.[2] The signal to noise ratio is reduced (compare the time slices around $t = 15 \ldots 20$). This is a first indication of the fact that lattice calculations become more difficult with decreasing quark mass m_{q}.

A better tool for looking at the signal to noise ratio, and particularly useful for finding the fit range (Section 3.5.2), is the effective mass,

$$m_{\mathrm{eff}}(t + 1/2) = \ln \left| \frac{C_{11}(t)}{C_{11}(t+1)} \right| .$$

Corresponding plots are shown on the r.h.s. of Figure 4.1. We again see higher (effective) masses for higher momenta. For time slices $t < 5$ we clearly have contributions from higher states, i.e. the effective mass is initially higher and

[1] The minimum of the correlation function is not centred in time direction.

[2] We use lattice units for the masses. For physical units we need to determine the lattice constant a and insert c and $\hbar$ appropriately.

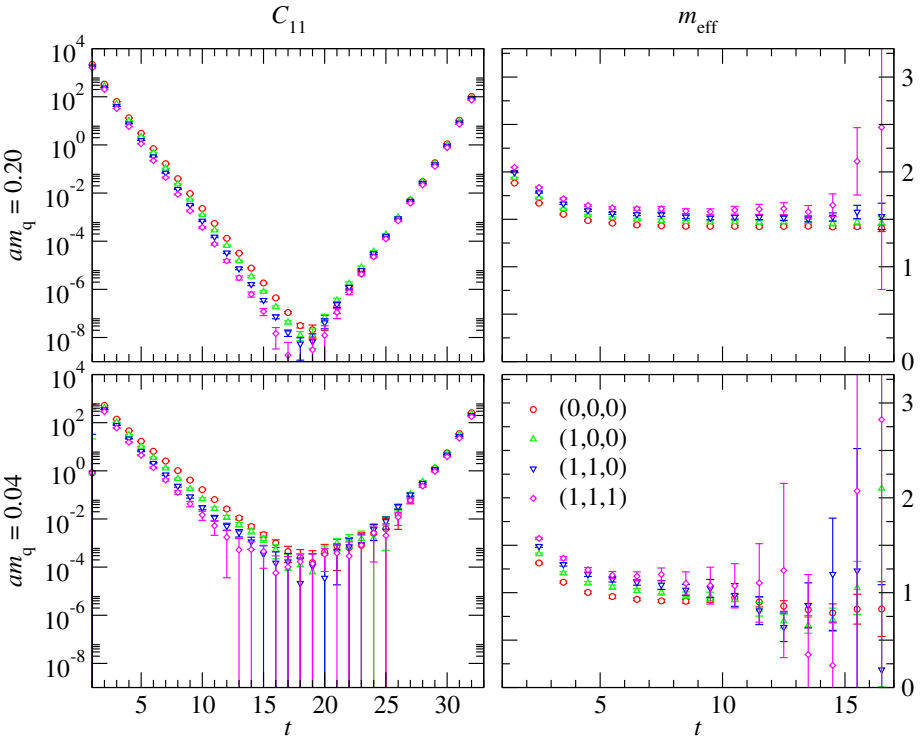

Figure 4.1: The l.h.s. shows the correlation function $C_{11}(t)$ (4.1) for different momenta with the matching vectors $\boldsymbol{n}$ given in the legend, the r.h.s. are the corresponding effective masses. The upper plots are for a bare quark mass of $am_{\mathrm{q}} = 0.20$, the lower ones for $am_{\mathrm{q}} = 0.04$. Note that the effective masses are only shown for positive parity. [$16^3 \times 32$, $\beta_1 = 7.90$, $am_{\mathrm{q}} = 0.20, 0.04$, smeared–point]

decreases. This can be explained with an admixture of states for small times where the states higher in energy decay more rapidly. The plateau within the effective mass plot indicates the fit range of the $\mathcal{N}_1$-state. In case of $am_{\mathrm{q}} = 0.20$ this is roughly from 6 to 16. Note the bigger errors for higher momenta and the less pronounced plateaus. The higher momenta enter the correlation function (4.1) as phase factors. These phase factors reduce cancellations of fluctuations between the different configurations and thus weaken the signal. In addition, as mentioned before, we do not get 'pure' states from our parity projection for $\boldsymbol{p} \neq 0$. This means we expect contributions from positive and negative parity states in both time directions. However, we do not find strong evidence for this possible mixing of parities.

Comparing again the upper ($am_{\mathrm{q}} = 0.20$) and the lower ($am_{\mathrm{q}} = 0.04$) plot we clearly observe the decreased signal to noise ratio. The plateaus are much shorter though still visible. We also see a strong dependence of the particle mass on the quark mass. While the effective mass of the $\mathcal{N}_1$-state is approximately $am_{\mathrm{eff}} = 1.5$ for $am_{\mathrm{q}} = 0.20$ it is much lower for smaller m_{q}. Thinking of m_{q} as the mass of the constituent quarks in the particle this is not surprising. The

plots show that the fit range has to be determined carefully and that it depends on m_{q}.

4.1.2 Dispersion relation

We have seen that the effective masses differ for the different momenta. A more quantitative test for the momentum projection is to check the relativistic energy-momentum relation

$$E^2 = m^2 + \boldsymbol{p}^2.$$

A plot of this dispersion relation should show a linear rise in E^2 for an increasing square of the momentum. In Figure 4.2 we evidently reproduce this linear behaviour. The energies shown in this plot are extracted from uncorrelated exponential fits (3.34) to the correlation function C_{11}. Note that we do not attempt to find the best fit ranges. Instead we use a very simple algorithm based on the fact that the fit range is more sensitive to the lower bound of the fit range. In this region contribution from higher states enter. Hence we keep t_{max} of the fit range fixed and vary t_{min} as long as the energy obtained by the fit still changes for more than 2.5%. The energies and their errors given in the plot are thus merely estimates. We do not quote results for smaller bare quark masses as the fit would require more care for this mass region.

Instead of plotting the dispersion relation, it is also possible to extract a quantity sometimes called 'speed of light'

$$c(\boldsymbol{p}) = \frac{E^2 - m^2}{\boldsymbol{p}^2}.$$

In case of small discretisation errors, this should yield $c = 1$ for all momenta

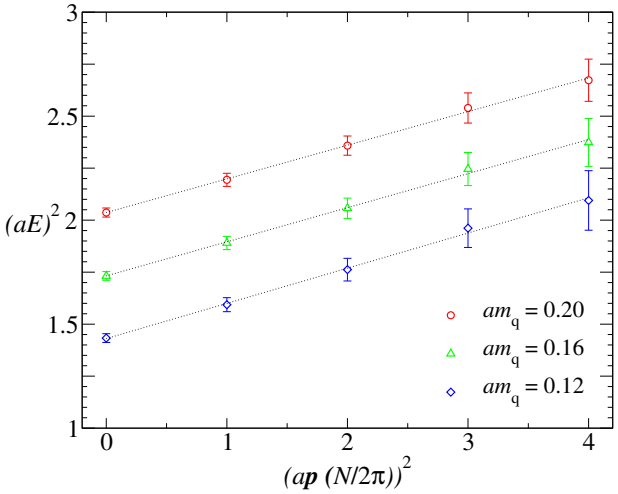

Figure 4.2: This plot shows the dispersion relation for the $\mathcal{N}_1$–$\mathcal{N}_1$ correlator for bare quark masses $am_{\mathrm{q}} = 0.20, 0.16$ and 0.12. The linear behaviour can clearly be seen. [$16^3 \times 32$, $\beta_1 = 7.90$, $am_{\mathrm{q}} = 0.20, 0.16, 0.12$, smeared–point]

according to the continuum dispersion relation. For the points shown in Figure 4.2 we typically have $c = 1.07 \pm 0.24$ (see Table D.3). If we take into account that this is only meant as test for momentum projection, using uncorrelated fits (3.34) and without special care for the fit ranges, this agrees well with the continuum value. Apart from the errors, this is compatible with [Sch02].

4.2 The full set of correlators

We now turn to the full set of three operators (2.15) with all possible cross-correlations (3.18)

$$C_{ij}^{\pm}(t) = \sum_{\boldsymbol{x}} \mathrm{Tr} \left\langle P^{\pm} \mathcal{N}_i(\boldsymbol{x}, t) \bar{\mathcal{N}}_j(\mathbf{0}, 0) \right\rangle . \tag{4.2}$$

We compute the correlation matrix C_{ij} for both possible parity projections, $P^{\pm}$ (3.11), and use the fact that $C_{ij}^{+}(t)$ and $C_{ij}^{-}(t)$ are related by time-reversal. We combine these two data sets to decrease the fluctuations and effectively have positive parity states propagating forward in time. In order to obtain 'pure' parity states from the projection, we apply a Fourier transform in (4.2) to have vanishing momentum in all cases (Section 3.2).

As discussed in Section 3.4, the correlation matrix C_{ij} is not analysed directly. Instead we use the eigenvalues (3.32)

$$\lambda_\alpha(t) = A_\alpha^{+} \mathrm{e}^{-E_\alpha^{+}(t-t_0)} + A_\alpha^{-} \mathrm{e}^{-E_\alpha^{-}(T-t-t_0)} \tag{4.3}$$

of the generalised eigenvalue problem (3.30) for our analysis.

The correlation matrix C_{ij} is calculated for all available lattices (Table D.2). We always have Jacobi smeared sources (Section 3.3) and use point-like as well as smeared sinks.

4.2.1 Eigenvalues and effective masses from the variational method

We obtain the correlation matrix C_{ij} for every configuration and average it over the different jackknife blocks.[3] The next step is to solve the generalised eigenvalue problem (3.30)

$$C^{-1}(t_0) \cdot C(t) \cdot v_\alpha = \lambda_\alpha(t)\, v_\alpha \tag{4.4}$$

for every jackknife block. Here we used matrix notation and $C(t)$ stands for both, C^{+} and C^{-}. The eigenvalues are normalised at $t_0 = 1$ (see Section 4.2.2) and, according to Section 3.4, sorted such that $\lambda_1 \geq \lambda_2 \geq \lambda_3$. Hence the state dominating λ_1 is lowest in mass (4.3). As mentioned above, we average the eigenvalues from different parity projections (λ^{+} is extracted from C^{+}, λ^{-} from C^{-} respectively)

$$\lambda_\alpha(t) = \frac{1}{2} \left[\lambda_\alpha^{+}(t) + \lambda_\alpha^{-}(T-t+2) \right] , \quad t = 1, 2, \ldots, T.$$

Note that we have periodic boundary conditions $\lambda_\alpha(T+1) = \lambda_\alpha(1)$. Taking this average reduces fluctuations within the data, but does not affect the statistics.

[3] Where we omit $l = 1$ configurations for each jackknife block.

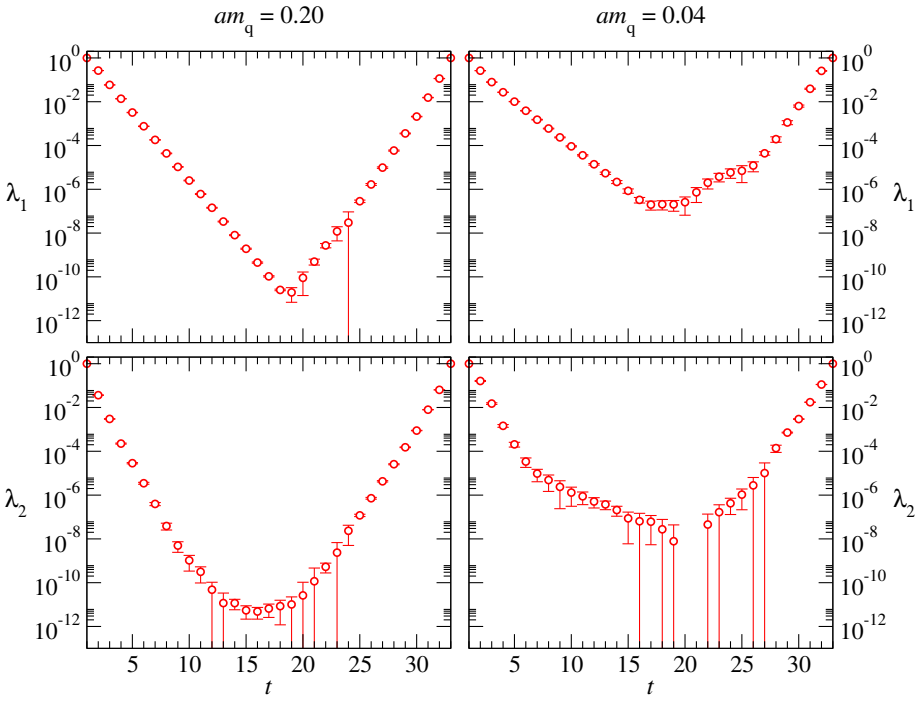

Figure 4.3: Plots of the eigenvalues λ_1 (upper row) and λ_2 (lower row) for two masses (l.h.s. $am_q = 0.20$, r.h.s. $am_q = 0.04$). We find decreasing overlap combined with larger errors when going to smaller bare quark masses. The third eigenvalue does not provide a useful signal and is omitted. [$16^3 \times 32$, $\beta_1 = 7.90$, $am_q = 0.20, 0.04$, smeared–point]

Eigenvalues

We perform the jackknife analysis as discussed in Section 3.6 to obtain statistical errors for the eigenvalues. Examples of the eigenvalues are shown in Figure 4.3 where the l.h.s. plots are for higher bare quark masses m_q. At large quark masses, the results are clean exponential decays with negligible errors for the positive parity ground state and the first two negative parity states. The signal for the second positive parity state is not quite as good. The third eigenvalue is plagued with contributions from higher states and does not provide a signal.[4] This behaviour can be understood from Equation (3.31), since the difference between the energies from this eigenvalue and the neglected states is small. In general, the signal for the lowest positive parity state is the most pronounced and can be followed to very small masses m_q (in case of the $16^3 \times 32$ lattices down to $\sim am_q = 0.015$). The signal to noise ratio decreases more rapidly for the three other states, in particular for the smaller $12^3 \times 24$ lattice.

[4] For some time slices and masses m_q we find eigenvalues that are smaller than 0, hence logarithmic plots of λ_3 are almost empty.

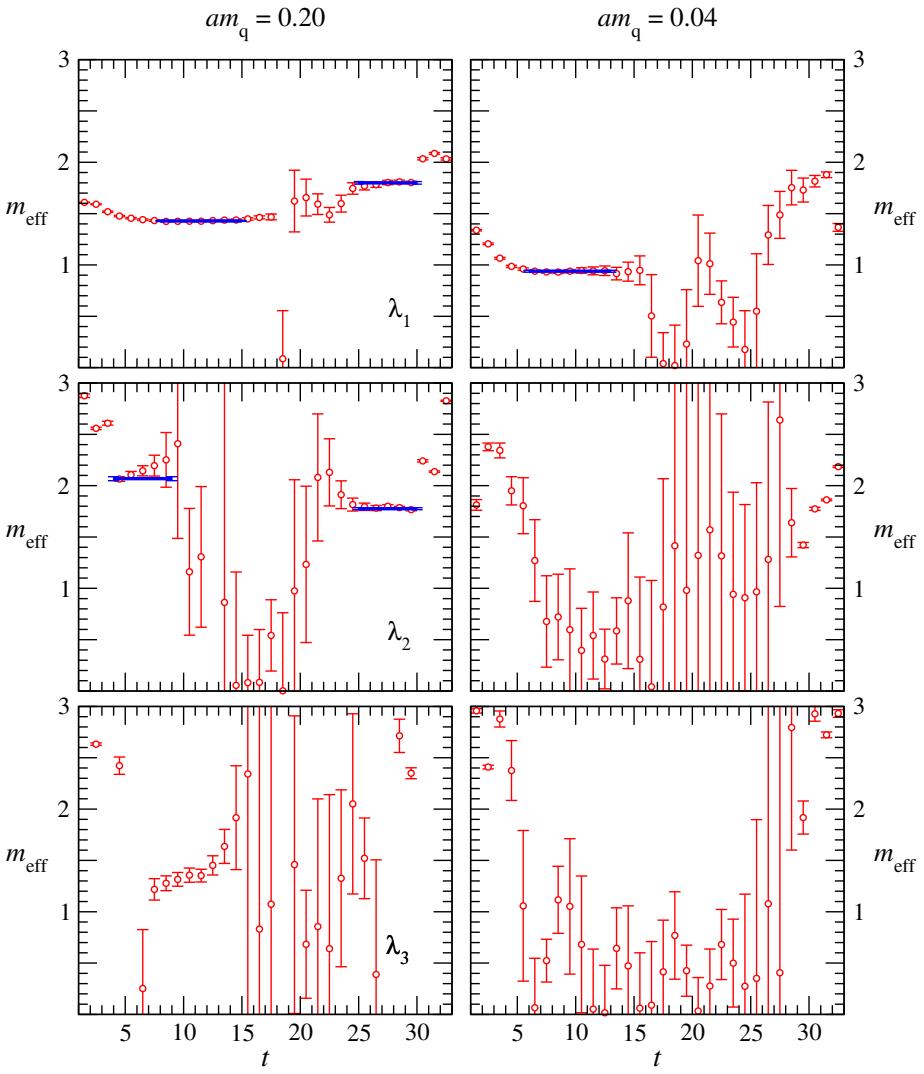

Figure 4.4: This plot shows effective masses to all three eigenvalues (λ_1, λ_2 and λ_3 from top to bottom) for two different quark masses. The solid lines indicate fit ranges and results from the fits. We initially find nice plateaus that decrease in length and quality for smaller quark masses (left to right). [$16^3 \times 32$, $\beta_1 = 7.90$, $am_q = 0.20, 0.04$, smeared–point]

Effective masses

As in Section 4.1.1 the quality of the signal is more obvious in the plots for the effective masses. We show examples for two masses and the $16^3 \times 32$ lattice in Figure 4.4. Solid lines indicate the fit ranges where the masses are extracted. Error bars on these lines indicate the statistical uncertainty of the fit. For larger masses of the Dirac operator (the plots on the left) we see a clear signal for the

ground states (upper plot) and the first excited state (middle plot). The states with positive parity are found at small t while the negative parity states are found for $t > 20$. Going to smaller bare masses shown in the plots on the r.h.s., the plateaus are shorter and less pronounced. In the case of Figure 4.4 we only see the positive parity ground state while the other states vanish. For completeness, the effective masses for the third eigenvalue are included (lower plots), but there is no useful signal for any of the masses m_q. Here contributions from higher states and vacuum modes are too large. The suggested plateau in the l.h.s. plot is below the mass of the lowest state and thus not a physical state. Consequently we do not attempt to extract any information from the third eigenvalue λ_3, regardless of the parity.

The effect of smearing

We have two sets of data for all lattices, i.e. point-like and Jacobi smeared sinks with the sources always Jacobi smeared. The difference between the two methods can be seen in Figure 4.5. We find that smearing increases the overlap with the positive parity ground state. This can be seen in the inserts in Figure 4.5 where we have less contributions from higher states for small t. This fact is less obvious for smaller quark masses. The other states are not improved, their fit ranges rather reduce or the states are less pronounced. Hence we will use smeared results for the positive parity ground state and non-smeared data for the remaining states. Nevertheless, fits are made to all sets of data, smeared and point-like sinks, to check for consistency. In addition, the different overlap of the states for point-like and smeared sinks is also visible from the fit parameter A_α. This parameter is linked to the fraction of the fitted state in the eigenvalue. Larger A_α indicate better overlap. This issue is addressed again in Section 4.2.3.

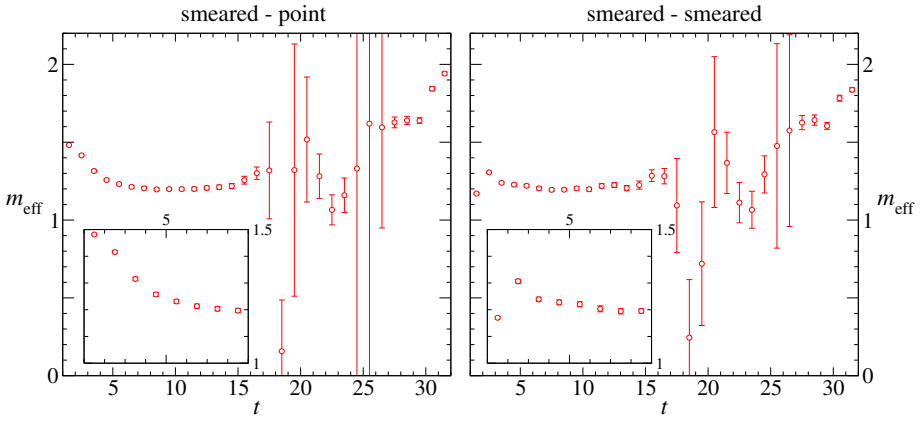

Figure 4.5: These plots show the effective mass of the first eigenvalue of configurations with point-like (l.h.s.) and smeared sinks (r.h.s.). Only the overlap with the positive parity ground state is improved. The inserts show an enlargement of the interesting region. [$16^3 \times 32$, $\beta_1 = 7.90$, $am_q = 0.12$, smeared–point and smeared–smeared]

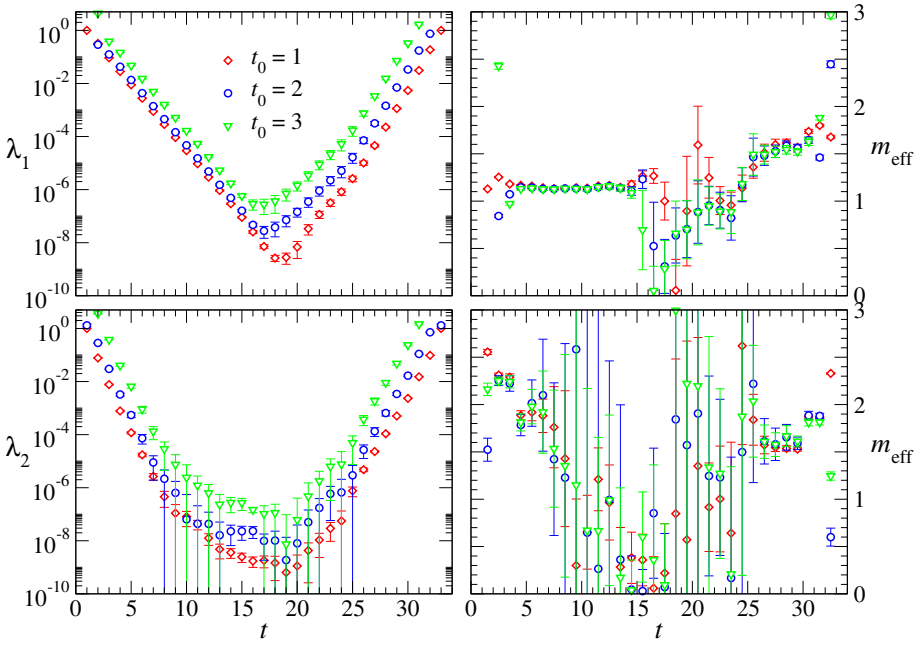

Figure 4.6: This plot shows a choice of three t_0 for a different normalisation of the eigenvalues. The l.h.s. shows eigenvalues λ_1 and λ_2 whereas the corresponding effective masses are on the r.h.s. [$16^3 \times 32$, $\beta_1 = 7.90$, $am_{\mathrm{q}} = 0.10$, smeared–smeared]

4.2.2 Normalisation of the eigenvalues

The variational approach discussed in Section 3.4 results in a generalised eigenvalue problem (3.30). This includes the matrix $C(t_0)$ as a normalisation factor. In general, the parameter t_0 can be used to tune the signal to noise ratio of the resulting eigenvalues. Figure 4.6 shows three different choices $t_0 = 1, 2, 3$.[5] We find a dependence of the data on the choice of t_0. However, the effect on the effective masses is small. Especially, the signal cannot be improved for any of the states for $t_0 \neq 1$. In addition, this choice is advantageous since it can be used reasonably well for both parities and thus reduces the computational effort.

4.2.3 Baryon Masses

The masses of the states are extracted from least squares fits to the eigenvalues λ_1 and λ_2. Therefore, the jackknife method provides us with N^{j} independent measurements that are necessary to determine statistical errors. Note that we use the terms mass and energy synonymous since there is no difference for zero momentum. Instead of using (4.3) as a fit function, we only use

$$\lambda_\alpha(t) \quad = \quad A_\alpha \mathrm{e}^{-E_\alpha(t-t_0)}. \tag{4.5}$$

[5] Strictly, this is only correct for the positive parity branch. Due to the time reflection for negative parity states this is equivalent to $t_0 = 1, T-1, T-2$ for the other branch.

We subsequently apply this fit to the l.h.s. and r.h.s. part of the eigenvalues, corresponding to the different parities. This is sufficient since the exponential decay of a state of one parity can be neglected as a contribution to the opposite parity. This reduces the procedure to a two parameter fit.

As already mentioned, some effort is necessary to determine the fit ranges. We inspect the plots of the effective masses for every bare quark mass and lattice used, to individually obtain the fit range. As the quality of the plateaus is poor for small quark masses, we start from the largest value for m_{q} and use this as a guide for smaller masses. In general, large fit ranges are desirable to use as much information as possible. The lower bound of the fit range, t_{min}, is more important and has considerable impact on the outcome of the fit. This fact is understood since possible contributions from higher states only have impact for small time slices. Thus, when going to lower quark masses, we try and keep t_{min} fixed as far as possible. We also avoid changing the length of the fit range for more than one time slice since this causes discontinuous results for the fit parameters A_α and E_α when comparing different masses. In addition to inspecting the plateaus in the effective mass plots, we use the value of χ^2/d.o.f. as a control parameter to decide if the fit is reasonable (c.f. Section 3.5). For examples of fits and ranges refer to Figures 3.1 and 4.4. All fit ranges and results for A_α and E_α as well as the χ^2/d.o.f. are given in Tables D.4–D.9. Figure 4.7 shows the obtained baryon masses plotted against the quark mass – both in lattice units – for one the $16^3 \times 32$, $\beta_1 = 7.90$ lattice. We only include values that conform to our constraints on the fit procedure explained above. The lowest

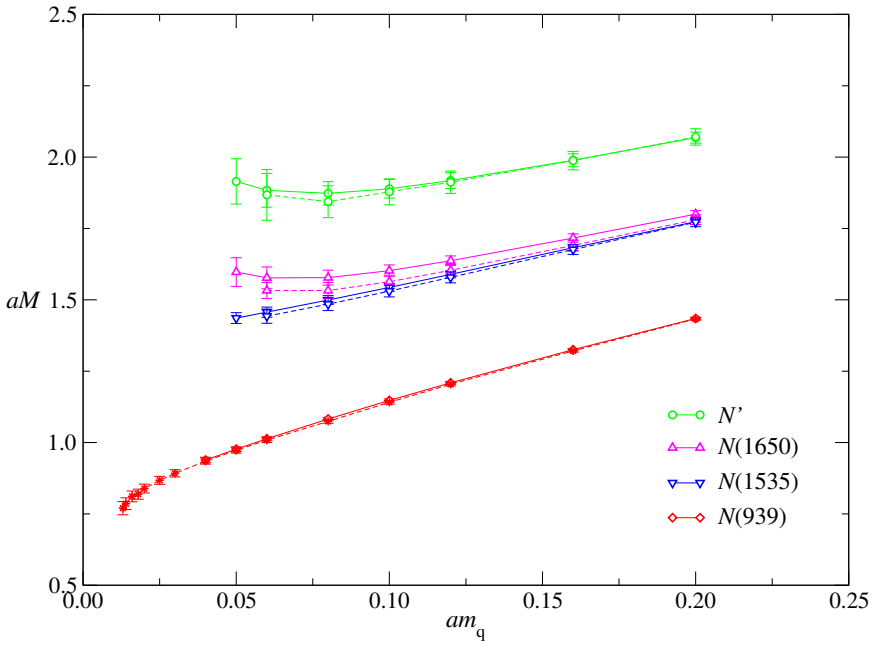

Figure 4.7: Baryon masses as a function of the quark mass in lattice units. Solid lines refer to point-like, broken lines to smeared sinks respectively. [$16^3 \times 32$, $\beta_1 = 7.90$, smeared–point and smeared–smeared]

state is the positive parity ground state. In Section 4.3 this state is identified with the nucleon $N(939)$. It provides by far the best signal and can be followed to very small quark masses until the plateau vanishes. The next two states higher in mass correspond to the negative parity states. They are confirmed to be $N(1535)$ and $N(1650)$. Both states can clearly be separated. However, the hyper-fine splitting due to spin dependent forces reduces towards larger quark masses. This has a physical reason since in this limit the interquark potential which is similar for both states dominates. The highest state is a positive parity state, obtained from λ_2. Looking at the ordering of the parities, we can already rule out that this state is the Roper $N(1440)$ resonance since the Roper is lower in mass than the negative parity states since it should be lower in mass. We denote this state by N'.

In general, we find increasing errors for smaller quark masses, related to the poorer signal to noise ratio (also see Section 4.2.1). The uncertainties for the excited states are again a bit larger than for the ground states. This fact is also discussed in the next paragraph. The results as discussed in Figure 4.7 are essentially the same for the other lattices used. Scaling or volume effects will be addressed in Section 4.5.

In addition to the mass E_α of the state, the second parameter of the fit (4.5), A_α, can also be interpreted. This parameter is the amplitude of the exponential decay of the state given by the eigenvalue. The amplitudes of all contributions to the eigenvalue, i.e. including all higher states, add up to 1 due to the normalisation (3.30). From Equation (3.31) we know that the lowest eigenvalue λ_1 contains the least contributions from other states since ΔE is large. Thus we expect the amplitudes close to one for the states given by λ_1. We extract the states $N(939)$ and $N(1650)$ from this eigenvalue and indeed the amplitudes are highest for these two states (refer to Tables D.4–D.9). The states N' and $N(1535)$ are extracted from λ_2 and have considerably lower amplitudes. Thus the admixture of higher states, as expected from smaller values ΔE, can be seen. Note that from the ordering of the eigenvalues ($\lambda_1 \geq \lambda_2 \geq \lambda_3$) and Equation (3.31) we expect the energies of the states ordered such that $E_1 \leq E_2 \leq E_3$. However, this is only found for the states with positive parity – negative parity states exhibit a reversed ordering. This reversal can only be understood if we assume large contributions from higher states to the eigenvalue connected to the $N(1535)$ state. The negative parity states are normalised at $t = 33$, thus an initial contribution of higher states pushes the eigenvalue corresponding to $N(1535)$ below the one of the $N(1650)$ state. The small mass splitting between the two states causes the slope of the two eigenvalues to have a similar magnitude so that the ordering is not reversed. Evidence for contributions of higher states can be found in the effective mass plot in Figure 4.4. Here we find rather large effective masses in the second eigenvalue compared to the first eigenvalue for $t > 30$. Additional indications for a more complex behaviour of this state occur in Section 4.4 where we address the contents of our operators. There we also find a significant change within the contributions to the second eigenvalue (see the r.h.s. of Figure 4.11).

We also remark that the overlap for the positive parity ground state is larger for Jacobi smeared sinks. The amplitudes for the other states are higher in the case of point-like sinks. Hence we again have a justification to use data sets with smeared sinks for the final results of the positive parity ground state and point-like sinks otherwise.

4.2.4 Conversion to physical scale

Our discussion was so far limited to results in lattice units only. All masses, momenta and volumes stated contained the lattice spacing a as factor. For a proper physical interpretation and meaningful results it is necessary to determine a for every value of β_1. The physical scale depends on β_1 since it is related to the gauge coupling of QCD (see Section 1.9).

There are two methods for determining the lattice constant a. It can be derived from the Sommer parameter r_0 which is related to the static potential between two quarks [GHS02]. An alternative possibility is to use another physical observable, such as e.g. a particle mass, that is accessible by experiments and whose extraction from lattice calculations is under control. The result from the lattice and its experimental value are then compared to provide the conversion factor a.

We use the latter approach. The observable used for setting the scale is the mass of the ρ meson. The necessary data (c.f. Table D.10) is taken from the calculations done in conjunction with [Sch02] and [Hie04]. The mass of the ρ meson is plotted against the quark mass and linearly extrapolated to the chiral limit (Section 4.3), as seen in Figure 4.8. The experimental value of 770 MeV [H$^+$02] is now used to set the scale. The uncertainties are obtained by fitting the data points plus and minus their errors. This provides upper and lower bounds for the lattice constant a. The results are shown in Table 4.1. A detailed description and more results can be found in [Hie04]. For the present work the given values are sufficient and a distinction between lattice sizes for $\beta_1 = 7.90$ and different smearing is not necessary.

4.3 The chiral limit

The goal of any simulation is the comparison to the experiment. After setting the scale in the previous section we can now convert the lattice units into physical units. However, the masses of the states found in Section 4.2.3 are not yet meaningful since the quark masses that enter the simulation are unphysically high. The lowest quark masses for which we still find a reasonable signal are at least three times larger than the physical quark masses of the up and down quarks. The unphysical quark masses cannot be avoided at present because it is not affordable to compute the Dirac propagator for such low masses as discussed in Section 1.8.2. Furthermore finite size effects become more drastic at smaller quark masses such that also the lattice size needs to be increased for smaller quark masses. Moreover, the signals obtained from the simulation become poor for small masses as shown in Sections 4.2.1 and 4.2.3. The lack of results at the

$V \times T$	β_1	a [fm]	L [fm]
$16^3 \times 32$	7.90	0.156 ± 0.003	2.5
$12^3 \times 24$	7.90		1.9
$16^3 \times 32$	8.35	0.111 ± 0.002	1.8

Table 4.1: Lattice constants a and sizes L for the lattices.

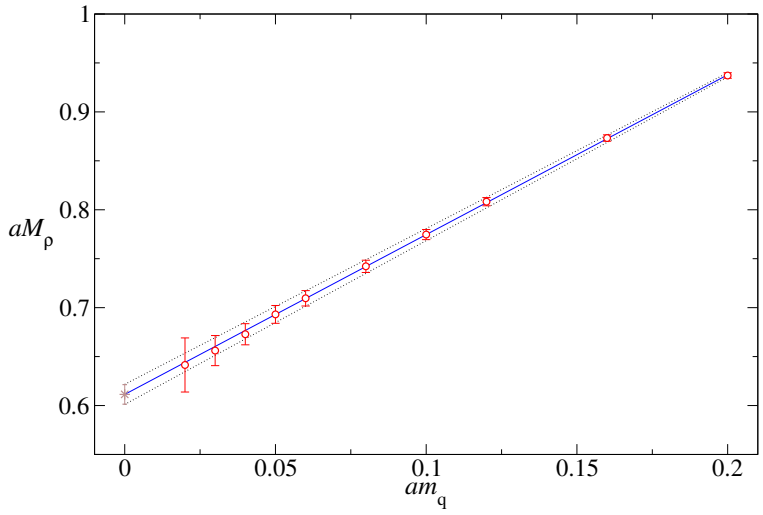

Figure 4.8: This plot shows the chiral extrapolation of data points for the ρ meson. Included is the upper and lower bound. [$16^3 \times 32$, $\beta_1 = 7.90$]

physical point is circumvented by extrapolations to the chiral limit. The chiral limit here refers to an extrapolation to vanishing quark masses.

Chiral extrapolations can be described in the framework of chiral perturbation theory. The quality of our data on the other hand does not require an approach that profound. Earlier works also rely on simpler fitting functions (also see [A$^+$00, G$^+$04] for a comparison of naive and chiral extrapolations). It turns out that the mass of the $N(939)$ state plotted against the quark mass can be described reasonably well by a behaviour of the form

$$(aM_{N(939)})^2 = C_0 + C_1\, am_q.$$

The states with negative parity can also be extrapolated linearly

$$aM = C_0' + C_1'\, am_q.$$

Figures 4.9 and 4.10 show chiral extrapolations for the $\beta_1 = 7.90$, $16^3 \times 32$ lattice for the states $N(939)$ respectively $N(1535)$ and $N(1650)$. The experimental values are indicated by stars. The numbers, as obtained from the extrapolations, are given in Table D.12. The χ^2/d.o.f. is always smaller than one. A better comparison to experimental values can be done with ratios of the masses. The ratios are dimensionless, i.e. the scale is set with baryons. These ratios are shown in Tables 4.2 and D.13. Note that the results in Table 4.2 include data with smeared sinks for the $N(939)$ and point-like sinks otherwise. We find the nucleon $N(939)$ and the ratio of the negative parities in perfect agreement with the physical values. The negative parity states are about 7% too high compared to the $N(939)$. Nevertheless, our results are certainly in good agreement with experimental data given that our calculations are done in the quenched approximation (see Section 1.7.1), where discrepancies up to 10% are seen in many observables.

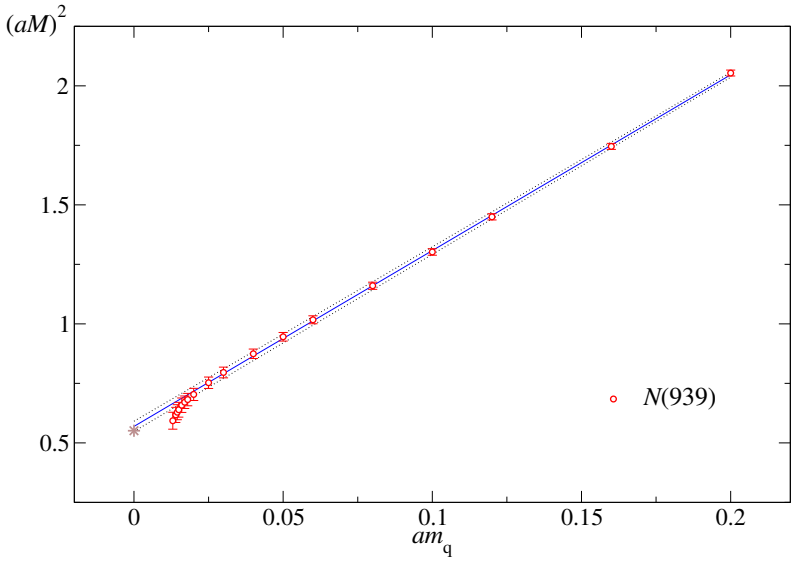

Figure 4.9: This plot shows the chiral extrapolation of data points for the $N(939)$ state. Included is the upper and lower bound, the physical value is marked by a star. [$16^3 \times 32$, $\beta_1 = 7.90$, smeared–smeared]

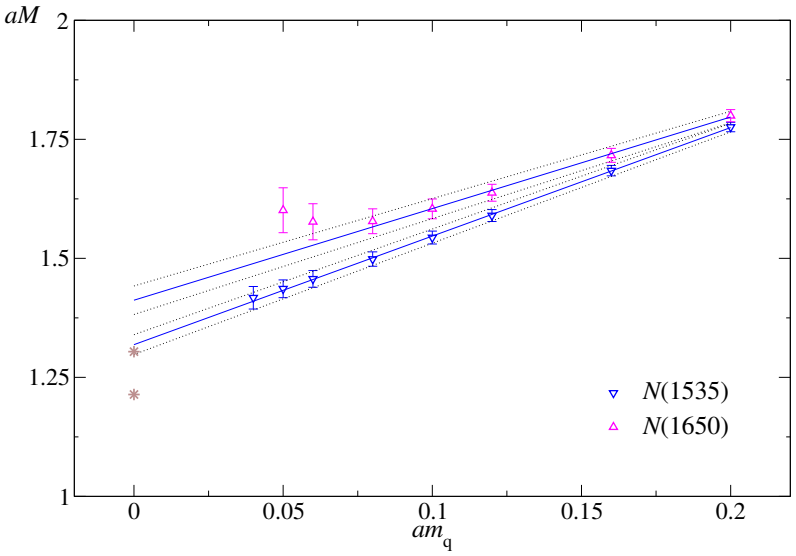

Figure 4.10: This plot shows the chiral extrapolations of data points for the negative parity states. Included are the upper and lower bounds and the physical values for $N(1535)$ and $N(1650)$ indicated by stars. [$16^3 \times 32$, $\beta_1 = 7.90$, smeared–point]

Considering the N' state, we can clearly conclude from the chiral extrapolations that it is not the Roper resonance $N(1440)$. The mass is by far too high (see Table D.12) and the correct relative level ordering for the Roper is not seen.

We also remark that our extrapolations are based on uncorrelated fits. Strictly, we would have to use correlated fits since the data sets for different masses m_{q} are not independent. This is due to the calculation of the Dirac propagator $\mathcal{D}^{-1}$ for different masses on the same set of gauge configurations. This results in correlations between the different quark masses. Thus we effectively have fewer degrees of freedom and we should expect slightly larger errors for the masses. Fully correlated fits for data based on the same lattices and with comparable results are for example done in [G+04].

4.4 Operator content

We interpret the content of our optimal operators, i.e. we take a closer look at their decomposition in terms of the original set of operators (Section 2.2.1). As explained in Section 3.4, the optimal operators are a superposition (3.26),

$$\tilde{\mathcal{N}}_\alpha = \sum_{i=1}^{r} c_i^\alpha \, \mathcal{N}_i, \tag{4.6}$$

where the coefficients c_i^α can be related to the components of the eigenvectors from the variational problem (4.4). We found

$$c_i^\alpha = (v_\alpha^*)_i. \tag{4.7}$$

Hence the components $(v_\alpha^*)_i$ of the eigenvectors provide insight into the physics of the nucleon system. In Figure 4.11 we show the coefficients c_i^α determined from the first two eigenvectors. These coefficients provide the optimal operators for the ground and excited state. Note that the eigenvectors are orthonormal since the correlation matrix is hermitian and normalised. Thus the sum of the squares of the coefficients is also normalised: $|c_1^\alpha|^2 + |c_2^\alpha|^2 + |c_3^\alpha|^2 = 1$. Looking at Figure 4.11, we find time dependence not only for the eigenvalues but also for the eigenvectors. A proper physical state on the other hand should be time independent since its structure does not change. Indeed we find plateaus for the coefficients in the same range of t values where we also see plateaus for

	simulation	experiment	difference
$M_{N(939)}/M_\rho$	1.239 ± 0.047	1.220	2%
$M_{N(1535)}/M_{N(939)}$	1.748 ± 0.134	1.633	7%
$M_{N(1650)}/M_{N(939)}$	1.872 ± 0.154	1.755	7%
$M_{N(1650)}/M_{N(1535)}$	1.071 ± 0.086	1.075	$< 1\%$

Table 4.2: Results from the chiral extrapolation. The ratios are given as dimensionless numbers. Experimental values are taken from [H+02]. Note that the errors are purely statistical uncertainties from the jackknife method. [$16^3 \times 32$, $\beta_1 = 7.90$]

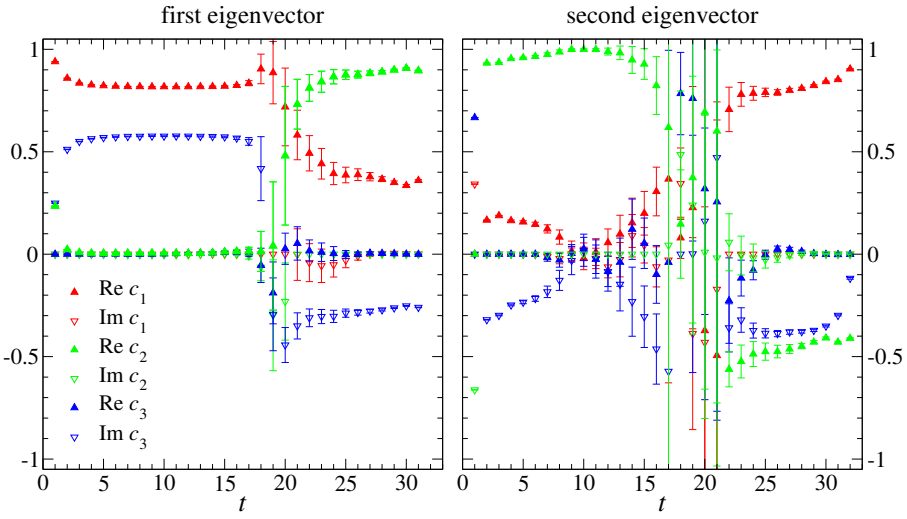

Figure 4.11: Here we plot the coefficients c_i from the first two eigenvectors against time t. [$16^3 \times 32$, $\beta_1 = 7.90$, $am_q = 0.16$, smeared–point]

the effective mass. For the first eigenvalue on the l.h.s. of Figure 4.11 the time independent region is approximately $t = 5 \ldots 15$, whereas the negative parity states again have shorter plateaus for $t = 26 \ldots 30$. A strong time dependence occurs for the time slices around $t = 1$ and 32 where higher excited states contribute and at the transition between positive and negative parity states at $t \sim 19$. Furthermore, the regions of these plateaus agree nicely with the fit ranges found in Section 4.2.3, again confirming the asymptotic behaviour necessary for a correct fit procedure. The excited positive parity state shows the most unclear behaviour as can be seen for $t < 19$ on the r.h.s. of Figure 4.11. Comparing this to the lower right plot in Figure 4.3 it seems that for $t < 7$ the N' state dominates and then changes to a much lighter contribution. This explains the difficulties when fitting the N' state.

We also plot the coefficients against the quark mass in order to see if the contributions to the optimal operators change when we approach the chiral limit. Therefore, we keep the time slice at which the coefficients are considered fixed within a plateau for each state. In particular we take $t = 8$ and $t = 5$ for the states $N(939)$ and N' respectively. For the negative parity states we chose $t = 28$. Figure 4.12 shows the corresponding plots. It is obvious from the figure that the coefficients have a non-trivial mass dependence. This behaviour towards the chiral limit indicates that the physics is influenced by chiral symmetry.

The content of our optimal operators can also be interpreted physically. Such an interpretation can be based on the quark model as discussed in Section 2.1. According to the quark model the $N(939)$ belongs to the **56**-plet (see Table 2.2) with a symmetric spatial wave function with respect to exchange of two quarks. Hence the parity of any diquark part in the nucleon wave function is positive. This also implies that the wave function of the SU(6) symmetric nucleon cannot contain a pseudo-scalar diquark content since it has negative parity [PS95]. The parity can easily by verified by calculations similar to the ones performed in

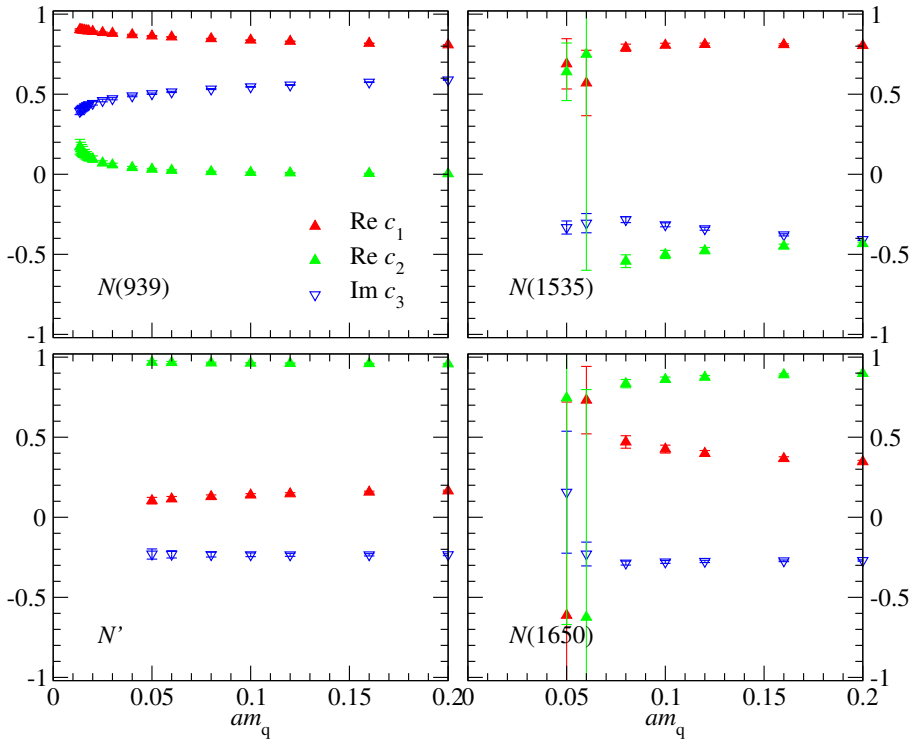

Figure 4.12: This plot shows the coefficients c_i from the first two eigenvectors for fixed times t but different masses am_q, only the non-zero parts of the coefficients are displayed. [$16^3 \times 32$, $\beta_1 = 7.90$, smeared–point]

Section 2.2.2. Consequently, the $N(939)$ state cannot couple to the operator $\mathcal{N}_2$. However, the SU(6) symmetry is broken (see Section 2.1.3) which can explain the small contributions from this operator that can be seen from the non-vanishing coefficient c_2 in the upper left plot in Figure 4.12. The different weight of the operators $\mathcal{N}_1$ and $\mathcal{N}_3$ can be attributed to the different chiral representation they belong to. If chiral symmetry was not broken, only one operator would couple to the nucleon. This might be indicated by the decrease of the amplitude c_3 for small quark masses. The fact that both operators have overlap with the nucleon ground state for large masses shows that chiral symmetry is broken.

Essentially the same applies for the Roper resonance $N(1440)$ since it also belongs to a **56**-plet, but is radially excited (Table 2.2). Comparing this to the N' state in the lower left of Figure 4.12 we find additional evidence that this is note the Roper resonance. This is due to the large coefficient c_2 implying good overlap with $\mathcal{N}_2$. In particular the overlap with $\mathcal{N}_1$ is small, unlike expected for $N(1440)$.

Although not quite as clear, similar arguments can be applied to the negative parity states on the l.h.s. of Figure 4.12. The $N(1535)$ and $N(1650)$ states both belong to a **70**-plet so the wave functions contain scalar and pseudo-scalar parts. We approximately find the states coupling to $(\mathcal{N}_1 - \mathcal{N}_2)$ in case of the $N(1535)$

and to $(\mathcal{N}_1 + \mathcal{N}_2)$ for the $N(1650)$ state. This behaviour can be used as a basis for the explanation of $N^* \to N\eta$ and $N^* \to N\pi$ decays [BCG+04].

This analysis also explains why the operator $\mathcal{N}_1$ is in general a good choice to obtain large overlap with the nucleon ground state $N(939)$. We find the biggest weight for this operator. Another observation is that the operator $\mathcal{N}_1$ has overlap with all four states. So in principle this operator could be used to extract masses for all the states from a single correlator with $\mathcal{N}_1$ only. However, our analysis also proves the strength of the variational method since some states contain much larger contributions from other operators.

4.5 Volume and discretisation effects

Simulations in lattice QCD always underly the constraint that either the physical volume of the lattice is small or the discretisation of space-time is done with sparsely spread lattice points. Desirable is the opposite, i.e. the limits $V \to \infty$ and $a \to 0$.

The constraint in either way leads to a problem. If the simulation is done with a too small volume, finite size effects occur. One common interpretation is that the studied states are squeezed into the volume and thus, following Heisenberg's uncertainty relation, their kinetic energy is increased. Another possible effect are fermion lines propagating around the lattice and thus contributing to the results. A bigger volume can be obtained with larger lattice spacings. However, this leads to an increase of discretisation effects.

Both effects can be studied. For volume effects one considers different lattice sizes with the lattice constant a (i.e. the coupling β_1) kept fixed. Scaling effects are observed for a constant physical lattice volume and varying number of lattice points in the space-time directions.

Our simulation is performed on three lattices (see Table 4.1), two of which have roughly the same physical volume while the lattices with different volume have the same lattice spacing. For each effect, two lattices are certainly not enough to attempt extrapolations to infinite volume or to continuum. However, we are able to check if our results are sensitive to these problems.

Finite size effects

We compare our results for both lattices with $\beta_1 = 7.90$ corresponding to a lattice spacing of $a = 0.156$ fm to check for finite size effects. The $16^3 \times 32$ lattice has a spatial extent of $L \sim 2.5$ fm while for the $16^3 \times 32$ lattice $L \sim 1.9$ fm. Note that the charge radius of the nucleon is less than 1 fm, hence we do not expect large effects for the $N(939)$ state. However, there is no clear statement for the size of the Roper. The results for all masses in GeV are shown in Figure 4.13. We do not find a strong dependence on the physical volume in our simulation. The results are compatible within errors. The rise of the higher masses towards the chiral limit cannot be attributed to physical finite size effects since we would expect a clearly different behaviour for the two lattices. In addition, we can once more rule out the possibility that the N' state is the Roper resonance. Finite size effects could in principle explain the energy shift of this resonance since, being a radially excited state, it should strongly suffer from squeezing effects described above.

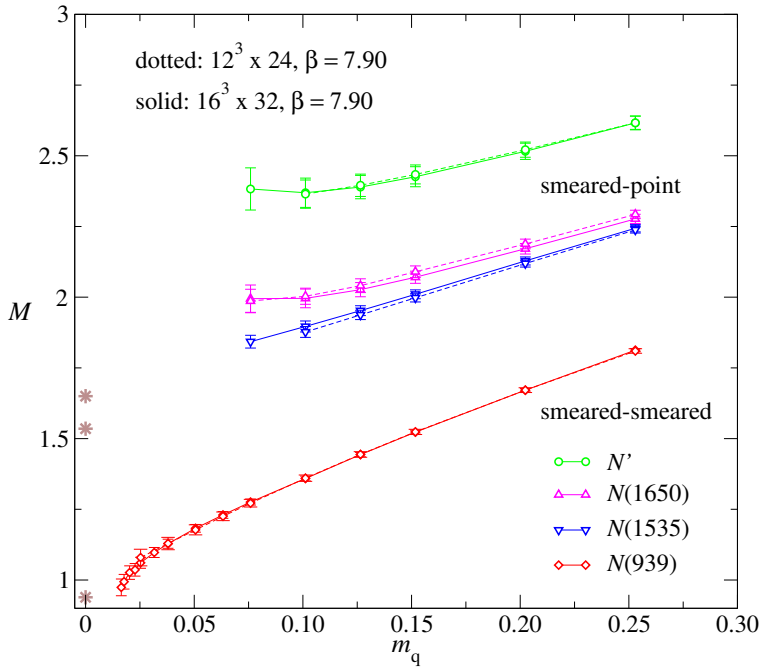

Figure 4.13: We show masses in GeV for lattices with the same lattice spacing but different volumes to reveal finite size effects. The full curve is for the $16^3 \times 32$ lattice, the broken curve corresponds to the $12^3 \times 24$ lattice. The sinks are smeared for the positive parity ground state and otherwise point-like. Experimental values are indicated by stars. [$16^3 \times 32$ and $12^3 \times 24$, $\beta_1 = 7.90$]

Scaling properties

The scaling behaviour is studied on two lattices with roughly the same physical extent of $L \sim 1.9$ fm. The lattices are $16^3 \times 32$ with $\beta_1 = 8.35$ and $12^3 \times 24$ with $\beta_1 = 7.90$ corresponding to $a = 0.111$ fm respectively $a = 0.156$ fm. In order to compare the two lattices for discretisation effects, it is important to have results that do not depend on the scale directly. We thus plot scale independent ratios of masses. For the $N(939)$ state, the ratio with the vector meson mass m_ρ is used. All other states are compared to the nucleon ground state. These ratios are plotted against $(m_{\rm PS}/m_\rho)^2$. The masses $m_{\rm PS}$ for the pion and m_ρ for the ρ meson are taken from [Sch02]. The plots are shown in Figure 4.14.We find that the results are compatible within errors, i.e. we do not see large scaling effects. Note that the errors shown are only statistical errors. Systematic uncertainties due to the difficulty of finding the fit ranges are not taken into account. In addition, the physical volume the two lattices only agrees within 5% making the observed deviations and conclusions less stringent.

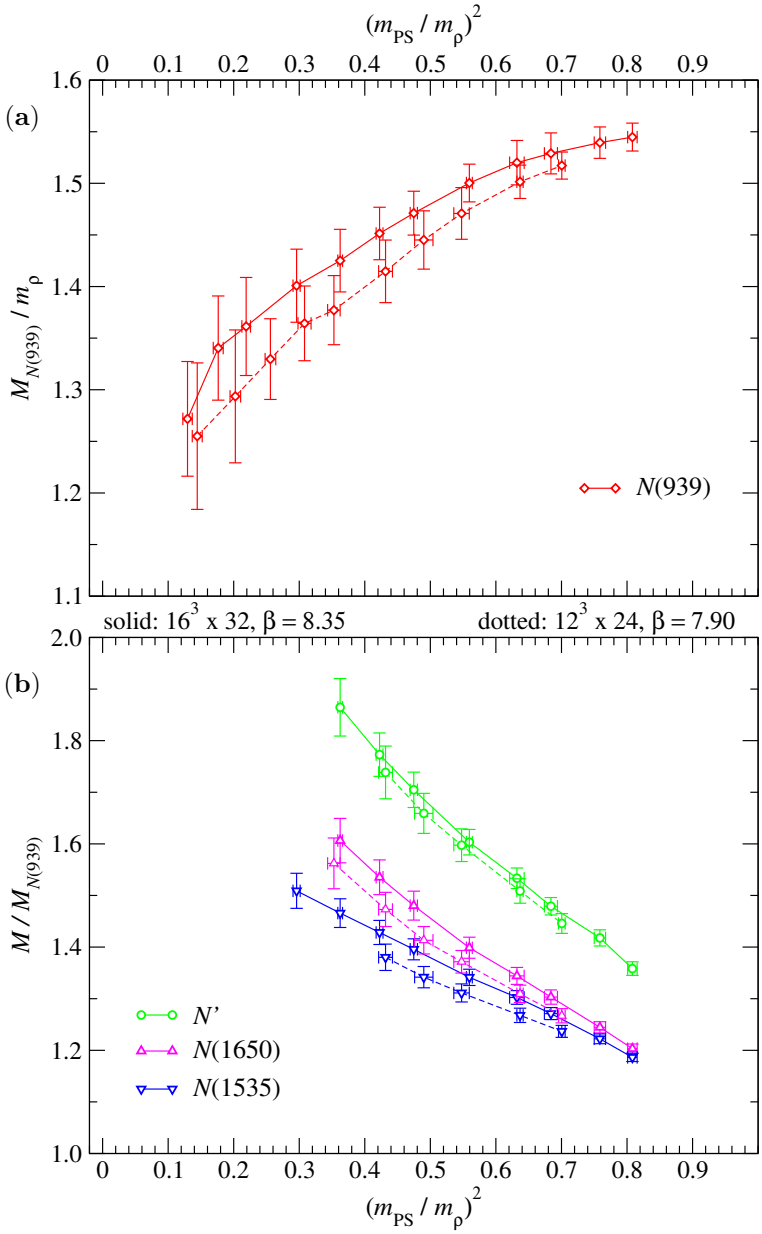

Figure 4.14: (**a**) A plot of the ratio of the $N(939)$ nucleon mass and the ρ meson against $(m_{\rm PS}/m_\rho)^2$. (**b**) A similar plot but now for ratios of the remaining states and the ground state nucleon.
We show two lattices with approximately the same physical extent $L \sim 1.9$ fm but different lattice constants a. For a good scaling behaviour we expect identical results. [$16^3 \times 32$, $\beta_1 = 8.35$ and $12^3 \times 24$, $\beta_1 = 7.90$]

4.6 Comparison to other groups

We now turn to a brief comparison to other groups.

Quite novel and controversial were the findings of Lee et al. [L$^+$03, D$^+$03]. They use constrained curve fitting with Bayesian priors and overlap fermions with exact chiral symmetry. Their lowest pion masses reached are at 180 MeV and they claim to find a level crossing of the first excited positive and negative parity states. For high quark masses their Roper state is comparable in size to our state N'. The level crossing then appears at pion masses $m_\pi \sim 220\,\text{MeV}$ which is below the region of our data. Close to the chiral limit, the Roper state then acquires the mass of the experimental value within errors. Hence they conclude that the Roper is a radial excitation of the nucleon with three valence quarks. They also conclude that the transition between heavy and light quarks occurs in the region $m_\pi \sim 300-400\,\text{MeV}$. Following their argument, the dynamics of the light quarks is dictated by chiral symmetry. This can be supported from our findings of the operator content in Section 4.4 where we also see a change in the coefficients. However, we find no hints for a level crossing of the excited positive and negative parity states.

Sasaki et al. [SSHA03, Sas03] also suggest a level switching between the Roper and the $N(1535)$ resonance which they observe at $m_\pi \sim 600\,\text{MeV}$. Although this is now in the region of our data, we did not find indications for that. They use Domain Wall fermions as well as the Wilson fermion action and combine both results to reveal the level crossing. In their articles they find it necessary to go to large physical volumes ($aL \sim 3$ fm) to identify the Roper resonance. On the other hand, to resolve the negative parity sector good chiral properties are found to be important. The masses of the states are reconstructed via spectral functions obtained from the MEM. Their analysis clearly reveal large finite size effects for the Roper resonance while the other states are not affected that strongly. This might point to problems with the MEM or indicate that their Roper resonance is not a pure state.

Other work also using the variational approach is for example [M$^+$03]. They use a FLIC fermion action to study the nucleon and other baryon octet resonances. Their correlation matrix is set up with only two operators $\mathcal{N}_1$ and $\mathcal{N}_2$ (also see [BCG$^+$04] for comparison). They find a clear splitting of the nucleon and its chiral partner and also between the negative parity states. This can be supported by our analysis of the operator content where $\mathcal{N}_1$ is found as main contribution for the ground state and a combination of both operators with the biggest weight for the negative parity states.

Summary and outlook

In the preceding chapters, non-perturbative QCD has been presented and was applied to a problem in nuclear physics. We introduced the formulation of lattice QCD starting with the Euclidean path integral. A connection between statistical mechanics and the formulation of the field theory was established. This connection can be used for a numerical simulation of QCD. In order to have a self-contained description, we introduced the Lagrangian of QCD and discussed chiral symmetry. We also outlined the underlying ideas of the applied lattice Dirac operator and the lattice gauge action. We then discussed the symmetries forming the basis of the experimentally observed multiplet structure of the nucleon. Next we turned to the lattice operators used to calculate the hadronic observables, i.e. the nucleon interpolating fields for the correlation functions. We discussed the technical details that lead to a definite momentum and parity of our observed particles as well as a smearing technique to increase the overlap of the operators. A detailed description of the variational approach to separate the physical states was then followed by a discussion of our fitting procedure.

The presented results were obtained from our quenched simulation using Chirally Improved fermions and the Lüscher-Weisz gauge action. In first tests we confirmed that our implementation of lattice QCD works as expected. We found the correct time behaviour of the correlation function and could reproduce a linear dispersion relation within error bars.

We then turned to our full set of interpolating fields and studied how they couple to the ground and excited states of both parities. The separation of the different states was achieved by the variational method. We could follow the signal of the nucleon ground state $N(939)$ down to quark masses around $m_{\mathrm{q}} \sim 20\,\mathrm{MeV}$ respectively to pion masses $m_{\mathrm{PS}} \sim 270\,\mathrm{MeV}$. The mass of the $N(939)$ state was found to be in perfect agreement with the experimental value. We could also clearly separate the negative parity states $N(1535)$ and $N(1650)$ for quark masses down to $m_{\mathrm{q}} \sim 65\,\mathrm{MeV}$ ($m_{\mathrm{PS}} \sim 500\,\mathrm{MeV}$). The relative splitting of the masses of the negative parity states was found in perfect agreement with experiment, but their masses came out about 7% too high compared to the nucleon ground state. This is nevertheless in good agreement to experiment for a quenched calculation. We could not identify the Roper $N'(1440)$ resonance. Instead, we found a state with much higher energy and from our analysis concluded that it cannot be identified with the Roper, in particular, we did not see a level crossing in the chiral region. One possibility is that the Roper resonance possesses a more intricate structure which we did not capture with the nucleon interpolating fields we used.

Our analysis of the components of the optimal operators revealed a clear

dependence on the quark mass. It is thus necessary to reach small quark masses while having good chiral properties. This is in particular valid for the negative parity sector.

Extracting the baryon spectrum from lattice simulations remains a challenge. We believe that the variational method is crucial for this task to obtain a clear separation of the states. Future simulations should thus be based on a larger set of operators. Additional improvements are possible with non-local interpolating fields, i.e. separated sources for the valence quarks inside the nucleon. The improved sources are expected to mimic a better nucleon wave function and hence provide more information about the dynamics. Such studies are currently in progress.

Although numerically much more challenging, the final goal will be calculations with dynamical quarks in the region where chiral perturbation theory is applicable and a reliable extrapolation to physical quark masses can be performed. Such calculations may become feasible with the next generation of supercomputers. We hope that the methods developed in this work will contribute to finally settle the question concerning the nature of the Roper resonance.

Appendix A

Notation and Conventions

A.1 Pauli matrices

The 2×2 Pauli matrices are defined by the Lie algebra

$$[\boldsymbol{\sigma}_i, \boldsymbol{\sigma}_j] = \boldsymbol{\sigma}_i \boldsymbol{\sigma}_j - \boldsymbol{\sigma}_j \boldsymbol{\sigma}_i = 2\mathrm{i}\epsilon_{ijk}\boldsymbol{\sigma}_k \tag{A.1}$$

and they read

$$\boldsymbol{\sigma}_1 = \begin{pmatrix} 0 & 1 \\ 1 & 0 \end{pmatrix}, \qquad \boldsymbol{\sigma}_2 = \begin{pmatrix} 0 & -\mathrm{i} \\ \mathrm{i} & 0 \end{pmatrix}, \qquad \boldsymbol{\sigma}_3 = \begin{pmatrix} 1 & 0 \\ 0 & -1 \end{pmatrix}. \tag{A.2}$$

A.2 Gamma matrices in Minkowski and Euclidean space

The gamma or Dirac matrices γ_μ in Minkowski space have to satisfy the following anti-commutation relations:

$$\{\gamma_\mu, \gamma_\nu\} \equiv \gamma_\mu\gamma_\nu + \gamma_\nu\gamma_\mu = 2g_{\mu\nu} \tag{A.3}$$

The Greek Dirac indices refer to Minkowski space: 0 for time and 1,2,3 for spatial coordinates. The matrix γ_5 is defined by

$$\gamma_5 = \mathrm{i}\gamma_0\gamma_1\gamma_2\gamma_3. \tag{A.4}$$

In a representation where γ_0 is diagonal they explicitly read:

$$\gamma_0 = \begin{pmatrix} \mathbf{1} & \mathbf{0} \\ \mathbf{0} & \mathbf{-1} \end{pmatrix}, \qquad \gamma_i = \begin{pmatrix} \mathbf{0} & \boldsymbol{\sigma}_i \\ -\boldsymbol{\sigma}_i & \mathbf{0} \end{pmatrix}, \qquad \gamma_5 = \begin{pmatrix} \mathbf{0} & \mathbf{1} \\ \mathbf{1} & \mathbf{0} \end{pmatrix}, \tag{A.5}$$

where $\boldsymbol{\sigma}_i$ are the 2×2 Pauli matrices. Latin indices denote the spatial indices 1,2,3 and $\mathbf{0}$ and $\mathbf{1}$ are 2×2 matrices.

The gamma matrices change for the case of Euclidean space which is used for lattice QCD. The time variable is continued to imaginary values (c.f. Section 1.1.1) resulting in a changed algebra

$$\{\gamma_\mu, \gamma_\nu\} = 2\delta_{\mu\nu} \tag{A.6}$$

and a different definition for γ_5

$$\gamma_5 = \gamma_1\gamma_2\gamma_3\gamma_4. \tag{A.7}$$

To stress the different Euclidean representation the Greek Dirac indices now run form 1 to 4 for spatial (1,2,3) and time coordinates (4). The gamma matrices then read:

$$\gamma_i = \begin{pmatrix} \mathbf{0} & -\mathrm{i}\boldsymbol{\sigma}_i \\ \mathrm{i}\boldsymbol{\sigma}_i & \mathbf{0} \end{pmatrix}, \qquad \gamma_4 = \begin{pmatrix} \mathbf{0} & \mathbf{1} \\ \mathbf{1} & \mathbf{0} \end{pmatrix}, \qquad \gamma_5 = \begin{pmatrix} \mathbf{1} & \mathbf{0} \\ \mathbf{0} & \mathbf{-1} \end{pmatrix}. \tag{A.8}$$

This is called the chiral representation of the Dirac gamma matrices in Euclidean space. For γ_5 we find

$$\{\gamma_5, \gamma_\mu\} = 0, \tag{A.9}$$

$$(\gamma_5)^2 = 1 \tag{A.10}$$

We will also need the charge conjugation matrix C. It is defined by the property

$$C\gamma_\mu^{\mathrm{T}} C^{-1} = -\gamma_\mu. \tag{A.11}$$

In the chiral representation it reads:

$$C = \mathrm{i}\gamma_2\gamma_4. \tag{A.12}$$

Additional useful properties of C are:

$$\begin{aligned} C\gamma_5^{\mathrm{T}} C^{-1} &= \gamma_5, \\ C = C^{-1} &= C^\dagger = -C^{\mathrm{T}}. \end{aligned} \tag{A.13}$$

A.3 Gell-Mann matrices

The generators for the algebra su(3) are proportional to the Gell-Mann matrices. They are usually defined as

$$\begin{aligned} \left[t^a, t^b\right] &= \mathrm{i} f^{abc} t^c, \\ t^a &= \frac{\lambda_a}{2}, \end{aligned} \tag{A.14}$$

where the f^{abc} are the structure constants of the algebra su(3) and λ_a the Gell-Mann matrices. f^{abc} is real and totally anti-symmetric. The fundamental representation of the $3^2 - 1$ hermitian matrices λ_a is:

$$\lambda_1 = \begin{pmatrix} 0 & 1 & 0 \\ 1 & 0 & 0 \\ 0 & 0 & 0 \end{pmatrix} \quad \lambda_2 = \begin{pmatrix} 0 & -\mathrm{i} & 0 \\ \mathrm{i} & 0 & 0 \\ 0 & 0 & 0 \end{pmatrix} \quad \lambda_3 = \begin{pmatrix} 1 & 0 & 0 \\ 0 & -1 & 0 \\ 0 & 0 & 0 \end{pmatrix}$$

$$\lambda_4 = \begin{pmatrix} 0 & 0 & 1 \\ 0 & 0 & 0 \\ 1 & 0 & 0 \end{pmatrix} \quad \lambda_5 = \begin{pmatrix} 0 & 0 & -\mathrm{i} \\ 0 & 0 & 0 \\ \mathrm{i} & 0 & 0 \end{pmatrix} \quad \lambda_6 = \begin{pmatrix} 0 & 0 & 0 \\ 0 & 0 & 1 \\ 0 & 1 & 0 \end{pmatrix}$$

$$\lambda_7 = \begin{pmatrix} 0 & 0 & 0 \\ 0 & 0 & -\mathrm{i} \\ 0 & \mathrm{i} & 0 \end{pmatrix} \quad \lambda_8 = \begin{pmatrix} \frac{1}{\sqrt{3}} & 0 & 0 \\ 0 & \frac{1}{\sqrt{3}} & 0 \\ 0 & 0 & \frac{-2}{\sqrt{3}} \end{pmatrix} \tag{A.15}$$

In the fundamental representation we then have

$$\mathrm{Tr}[t^a t^b] = \frac{1}{2}\delta^{ab}. \tag{A.16}$$

A.4 Discretised space-time

In Sections 1.1.1 and 1.1.2 the discretisation of space and time is introduced. The continuous variables x and t change to discrete sets:

$$\begin{aligned} (x^i, t) \to (x^i_{n^i}, t_m)\,, \qquad & i = 1,2,3 \text{ and} \\ & n^i = 0,1,\ldots,N-1,\ m = 0,1,\ldots,N_{\text{time}}-1 \\ x^i_{n^i} = n^i \cdot a\,, \quad & t_m = m \cdot a\,. \end{aligned} \tag{A.17}$$

Indices 1, 2, 3 refer to spatial coordinates and index 4 to the time coordinate. N is the number of spatial lattice points in one direction, N_{time} the number of time slices. Equation (A.17) defines the lattice constant a. A finite four-volume then reads:

$$\Omega = V \cdot T = L^3 \cdot T = a^4 \cdot N^3 \cdot N_{\text{time}}, \tag{A.18}$$

where V is the spatial volume, L the length in a spatial direction of the lattice and T the time extent. We use $c = 1$.
Some implications then are

$$\int \mathrm{d}^4x \quad \to \quad a^4 \sum_{x_i}, \tag{A.19}$$

$$[\mathrm{d}U] \quad \to \quad \prod_{x,\mu} \mathrm{d}U_\mu(x). \tag{A.20}$$

In an analogous way to the discretised space, momentum space also has discrete values only

$$\boldsymbol{p} = a\frac{2\pi}{N}\boldsymbol{n}\,, \quad n^i = 0,1,\ldots,N-1,\ i = 1,2,3. \tag{A.21}$$

Note that (A.21) explicitly depends on the boundary conditions of the lattice. Here we use periodic boundary conditions for space coordinates and anti-periodic boundary conditions for time. Note also that (A.21) (unlike (3.2)) is in physical units since the lattice constant a is included.

A.5 Rules for Young tableaus

A perhaps more general introduction to the usage of Young tableaus can be found in the Particle Data Book [H$^+$02] or any good book on group theory.[1] A set of rules sufficient for our purpose is given in [Clo79].

We need rules on how to combine Young diagrams and calculate the number of particles within the multiplets, e.g. for SU(6)

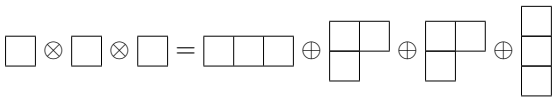

$$\mathbf{6} \otimes \mathbf{6} \otimes \mathbf{6} = \mathbf{56} \oplus \mathbf{70} \oplus \mathbf{70} \oplus \mathbf{20} \tag{A.22}$$

[1] for example references in [H$^+$02] and [Clo79].

where the last line states the dimensions of the multiplets. The multiplication of the representations, equivalent to combining the tableaus, is done successively one by one, i.e. we multiply the first two, then the next one is multiplied on this result and so forth. Combining two diagrams is done pictorially by adding the boxes of each of the diagrams to form all possibly allowed Young tableaus. So the first new combinations from the l.h.s. of (A.22) are

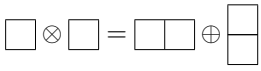

(A.23)

This is independent of the dimension of SU(N). Note that no diagrams need to be drawn with more than N boxes in any column. We will see that the dimension of such diagrams is trivially zero. We continue with combining the last diagram, so we have to add another box to the result of (A.23). Therefore we need to know the allowed diagrams resulting form the two combinations

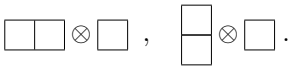

For us sufficient is the fact that no Young tableaus are allowed that are concave upwards nor concave towards the lower left.[2] Thus diagrams like

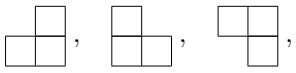

are forbidden whereas combinations like

are possible. In other words: Young tableaus need to be left justified and row m has to have at least as many boxes as row $m+1$. With these constraints, we obtain

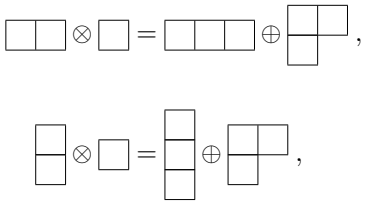

(A.24)

which is the result (A.22). What is now left, is to calculate the number of particles within the multiplets respectively their dimensionality. Here, the Particle Data Book [H$^+$02] provides a general equation which is a product of $\sum_{i=1}^{N-1} i$ factors for SU(N). We again use a pictorial recipe which involves forming a ratio of two numbers.

The *numerator* for any SU(N) diagram is obtained by assigning numbers to the boxes and take the product of theses numbers. The numbering scheme is as follows: Start by assigning N to the top left box, then continue with $N+1, N+2, \ldots$ in this row. For the next row start with $N-1$ on the left and

[2] more general rules are e.g. in [H$^+$02].

do the same. This is done for all rows. Some examples are:

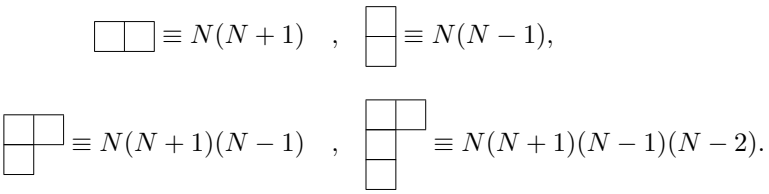

$$\equiv N(N+1) \quad , \quad \equiv N(N-1),$$

$$\equiv N(N+1)(N-1) \quad , \quad \equiv N(N+1)(N-1)(N-2).$$

We immediately see that diagrams with more than N boxes is any column have a factor of zero in the numerator and thus vanish.

The *denominator* is a product of 'hooks'. Each hook is associated with a number equal to the number of boxes the hook intersects. The hooks are found by drawing a line entering each row from the right and leaving the Young diagram to the bottom for each encountered box. Again some examples are:

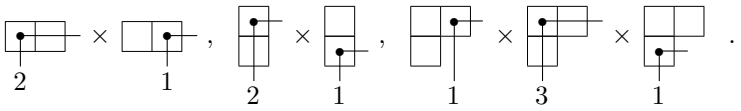

So the dimensions of the Young diagrams in (A.24) then are:

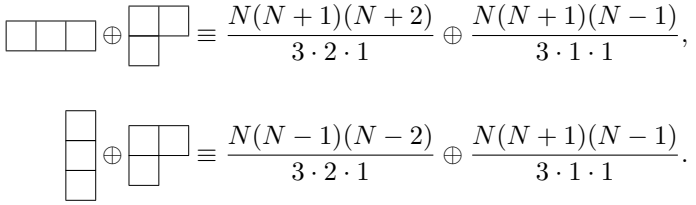

$$\equiv \frac{N(N+1)(N+2)}{3\cdot 2\cdot 1} \oplus \frac{N(N+1)(N-1)}{3\cdot 1\cdot 1},$$

$$\equiv \frac{N(N-1)(N-2)}{3\cdot 2\cdot 1} \oplus \frac{N(N+1)(N-1)}{3\cdot 1\cdot 1}. \tag{A.25}$$

This yields the result (A.22) for $N = 6$.

Appendix B

Calculations with Grassmann numbers

B.1 A Gaussian integral with Grassmann numbers

Grassmann numbers are anti-commuting. This implies that the square of any Grassmann variable is zero. Hence functions of these variables are polynomials of finite degree which will simplify the Gaussian integral. To solve the Gaussian integral we follow [ZJ02]. We want to solve (1.59), containing the Gaussian part

$$\int [\mathrm{d}\psi][\mathrm{d}\bar{\psi}] \mathrm{e}^{\bar{\psi}_i \mathcal{D}_{ij} \psi_j} \tag{B.1}$$

where we have included multi-indices i and j denoting flavour, colour, Dirac and space-time indices. Let N be the number of different flavour, colour, Dirac and Euclidean combinations. The integrand can be re-written:

$$\exp\left(\sum_{i,j=1}^{N} \bar{\psi}_i \mathcal{D}_{ij} \psi_j\right) = \prod_{i,j=1}^{N} \exp\left(\bar{\psi}_i \mathcal{D}_{ij} \psi_j\right) = \prod_{i,j=1}^{N} (1 + \bar{\psi}_i \mathcal{D}_{ij} \psi_j). \tag{B.2}$$

There are no other terms in the expansion of the exponential, as these would contain vanishing squares of Grassmann numbers. According to the rules of Grassmann integration, the result of (B.1) is the coefficient of the product $\bar{\psi}_N \psi_N \dots \bar{\psi}_1 \psi_1$ in the expansion (B.2). The only non-zero contributions to the integral of the expansion of the integrand (B.2) are

$$\sum_{\substack{\text{permutations p} \\ \text{of } 1,2,\dots,N}} \mathcal{D}_{1p_1} \mathcal{D}_{2p_2} \dots \mathcal{D}_{Np_N} \bar{\psi}_N \psi_{p_N} \dots \bar{\psi}_1 \psi_{p_1}. \tag{B.3}$$

Commuting the fields ψ_i to appear pairwise with the corresponding fields $\bar{\psi}_j$, we pick up a sign from the possible permutations

$$\sum_{\substack{\text{permutations p} \\ \text{of } 1,2,\dots,N}} \mathrm{sign}(p) \mathcal{D}_{1p_1} \mathcal{D}_{2p_2} \dots \mathcal{D}_{Np_N} \bar{\psi}_N \psi_N \dots \bar{\psi}_1 \psi_1. \tag{B.4}$$

The final result therefore is the fermion determinant:

$$\int [\mathrm{d}\psi][\mathrm{d}\bar{\psi}] \mathrm{e}^{\bar{\psi}_i \mathcal{D}_{ij} \psi_j} \equiv \det \mathcal{D}. \tag{B.5}$$

Note that the same calculation using standard numbers as opposed to Grassmann numbers yields $(\det \mathcal{D})^{-1}$ as a result. The derivation of this result can also be done with a change of variables

$$\mathcal{D}_{ij} \psi_j = \psi'_j \tag{B.6}$$

in the exponent.

B.2 Proof of Wick's Theorem

The theorem reads:

$$\begin{aligned} &\left\langle \psi_{i_1} \bar{\psi}_{j_1} \psi_{i_2} \bar{\psi}_{j_2} \cdots \psi_{i_n} \bar{\psi}_{j_n} \right\rangle \\ &\qquad = (-1)^n \sum_{\substack{\text{permutations } p \\ \text{of } 1,2,\ldots,n}} \left\langle \mathrm{sign}(p)\, \mathcal{D}^{-1}_{i_1 j_{p_1}} \mathcal{D}^{-1}_{i_2 j_{p_2}} \cdots \mathcal{D}^{-1}_{i_n j_{p_n}} \right\rangle_G \end{aligned} \tag{B.7}$$

where the ψ ($\bar{\psi}$) are (anti-) fermion fields, the indices are multi-indices denoting all of the colour, Dirac and space-time indices.[1] $\mathcal{D}$ is the Dirac operator and $\mathcal{D}^{-1}$ the corresponding propagator. Note that ψ and $\bar{\psi}$ appear pairwise only. Any correlator can be brought into this form by anti-commuting the fields.

Instead of proving (B.7) by induction we go along the same lines as for the Gaussian integral in Section B.1. We use the anti-commuting nature of Grassmann numbers and start with expanding the exponential in the generating functional (1.60). The remaining part after using (1.62) can then be re-written (analogous to (B.2))

$$\exp\left(\sum_{i,j=1}^{N} \bar{\eta}_i \mathcal{D}^{-1}_{ij} \eta_j \right) = \prod_{i,j=1}^{N} \exp\left(\bar{\eta}_i \mathcal{D}^{-1}_{ij} \eta_j \right) = \prod_{i,j=1}^{N} (1 + \bar{\eta}_i \mathcal{D}^{-1}_{ij} \eta_j). \tag{B.8}$$

We assume that the multi-indices i and j run from $1 \ldots N$. If we now think of n derivatives as in the general case of (B.7), we see that combinations with less than n factors of $(\bar{\eta}_i \mathcal{D}^{-1}_{ij} \eta_j)$ vanish due to the derivatives. Combinations with more than n such factors will also not contribute as we evaluate the generating functional with $\eta, \bar{\eta} = 0$. Hence the only non-vanishing contributions contain exactly n factors $(\bar{\eta}_i \mathcal{D}^{-1}_{ij} \eta_j)$. However, not only the number of factors has to be the same, but also the set of indices $(i_1, i_2, \ldots, i_n, j_1, j_2, \ldots, j_n)$ has to match the contributing factors. Otherwise again one or more derivatives would result in a vanishing factor. The overall contributions thus are:

$$\sum_{\substack{\text{permutations p} \\ \text{of } 1,2,\ldots,n}} \mathcal{D}^{-1}_{i_1 j_{p_1}} \mathcal{D}^{-1}_{i_2 j_{p_2}} \ldots \mathcal{D}^{-1}_{i_n j_{p_n}} \bar{\eta}_{i_n} \eta_{j_{p_n}} \ldots \bar{\eta}_{i_1} \eta_{j_{p_1}}. \tag{B.9}$$

[1] Wick's theorem factorises with respect to flavour indices as $\mathcal{D}$ is diagonal in flavour space. Hence the theorem can be applied for each flavour separately.

Quite naturally we only get results for $n \leq N$, or else the Pauli exclusion principle forbids any such combination. After commuting the currents $\eta, \bar{\eta}$ to appear pairwise and with the same ordering as on the l.h.s. of (B.7)) we pick up a sign according to the permutations:

$$\sum_{\substack{\text{permutations p} \\ \text{of } 1,2,\ldots,n}} \operatorname{sign}(p) \mathcal{D}^{-1}_{i_1 j_{p_1}} \mathcal{D}^{-1}_{i_2 j_{p_2}} \ldots \mathcal{D}^{-1}_{i_n j_{p_n}} \bar{\eta}_{i_1} \eta_{j_1} \ldots \bar{\eta}_{i_n} \eta_{j_n}. \tag{B.10}$$

Including the derivatives

$$\begin{aligned} \left\langle \psi_{i_1} \bar{\psi}_{j_1} \psi_{i_2} \bar{\psi}_{j_2} \cdots \psi_{i_n} \bar{\psi}_{j_n} \right\rangle &= \frac{\partial}{\partial \bar{\eta}_{i_1}} \frac{\partial}{\partial \eta_{j_1}} \frac{\partial}{\partial \bar{\eta}_{i_2}} \frac{\partial}{\partial \eta_{j_2}} \cdots \frac{\partial}{\partial \bar{\eta}_{i_n}} \frac{\partial}{\partial \eta_{j_n}} \\ &\times \sum_{\substack{\text{permutations p} \\ \text{of } 1,2,\ldots,n}} \left\langle \operatorname{sign}(p) \mathcal{D}^{-1}_{i_1 j_{p_1}} \mathcal{D}^{-1}_{i_2 j_{p_2}} \ldots \mathcal{D}^{-1}_{i_n j_{p_n}} \bar{\eta}_{i_1} \eta_{j_1} \ldots \bar{\eta}_{i_n} \eta_{j_n} \right\rangle_G, \end{aligned} \tag{B.11}$$

we see that we need to anti-commute each pair of currents $\bar{\eta}\eta$ to match the order in which the derivatives are taken.[2] This adds an extra $(-1)^n$ and we finally get

$$\begin{aligned} &\left\langle \psi_{i_1} \bar{\psi}_{j_1} \psi_{i_2} \bar{\psi}_{j_2} \cdots \psi_{i_n} \bar{\psi}_{j_n} \right\rangle \\ &\qquad = (-1)^n \sum_{\substack{\text{permutations } p \\ \text{of } 1,2,\ldots,n}} \left\langle \operatorname{sign}(p)\ \mathcal{D}^{-1}_{i_1 j_{p_1}} \mathcal{D}^{-1}_{i_2 j_{p_2}} \cdots \mathcal{D}^{-1}_{i_n j_{p_n}} \right\rangle_G. \end{aligned} \tag{B.12}$$

□

[2] Since the Grassmann derivatives also anti-commute and have to act directly on the corresponding variable.

Appendix C

Particle properties

Apart from the data of the simulation, the following is taken from the Particle Data Book [H$^+$02].

C.1 Quantum numbers

Quarks

All quarks carry spin $\frac{1}{2}$ and baryon number $\frac{1}{3}$. Non-zero additive quantum numbers are given in the table below.

$Q = -1/3$			$Q = +2/3$		
d	I_z	$= -1/2$	d	I_z	$= +1/2$
s	S	$= -1$	c	C	$= +1$
b	B	$= -1$	t	T	$= +1$

Q denotes the electromagnetic charge. The other quantum numbers in this table are the z-component of the isospin I_z, strangeness S, charm C, bottomness B and topness T.

Nuclei

	$I(J^P)$		$I(J^P)$
$N(939)$	$\frac{1}{2}(\frac{1}{2}^+)$	$N(1535)$	$\frac{1}{2}(\frac{1}{2}^-)$
$N(1440)$	$\frac{1}{2}(\frac{1}{2}^+)$	$N(1650)$	$\frac{1}{2}(\frac{1}{2}^-)$

Here I, J and P are isospin, total angular momentum and parity. The numbers in parentheses are the approximate masses in MeV. All nucleons have quantum numbers strangeness, charm, bottomness and topness 0. Charge and the baryon number are +1. The flavour content of the nucleons is (uud). In addition, the ground state $N(939)$ can also be identified with the neutron of charge 0 and flavour content (udd).[1]

[1] The negligible mass splitting between the neutron and the proton is due to electromagnetic effects and a slight difference in m_d and m_u.

C.2 Nucleon Masses

		experiment	simulation
p	****	938.271998 ± 0.000038	954 ± 36
n	****	939.565330 ± 0.000038	
$N(1440)$ P_{11}	****	1430 to 1470	
$N(1535)$ S_{11}	****	1520 to 1555	1668 ± 60
$N(1650)$ S_{11}	****	1640 to 1480	1786 ± 74

The masses are given in MeV. *"Particles are like hotels: they are put in categories and awarded stars."*[2] The stars $(*)$ therefore refer to the status of the particle. Categories are from $(*)$ to $(****)$, for the latter meaning excistence is certain and properties are at least fairly well explored.

[2]Quote from an unacquainted participant at a lattice conference.

Appendix D

Compiled data

$V \times T$	β_1	β_2	β_3
$12^3 \times 24$	7.90000	-0.54305	$-5.34600 \cdot 10^{-2}$
$16^3 \times 32$	7.90000	-0.54305	$-5.34600 \cdot 10^{-2}$
$16^3 \times 32$	8.35000	-0.55499	$-4.91900 \cdot 10^{-2}$

Table D.1: A list of the lattice sizes and β-values used for this work.

$V \times T$	β_1	#	am_{q}
$12^3 \times 24$	7.90	100	0.20, 0.16, 0.12, 0.10, 0.08, 0.06, 0.05, 0.04, 0.03, 0.02, 0.01
$16^3 \times 32$	7.90	100	0.0250, 0.0200, 0.0180, 0.0170, 0.0160, 0.0150, 0.0145, 0.0140, 0.0135, 0.0130, 0.0125, 0.0120, 0.0115, 0.0110
		100	0.20, 0.16, 0.12, 0.10, 0.08, 0.06, 0.05, 0.04, 0.03, 0.02
$16^3 \times 32$	8.35	91	0.20, 0.16, 0.12, 0.10, 0.08, 0.06, 0.05, 0.04, 0.03, 0.02, 0.015, 0.01

Table D.2: Number of configurations and bare quark masses available for each lattice. [Chapter 4]

am_q	$c(\boldsymbol{p})$			
$a^2\boldsymbol{p}^2(N/2\pi)^2$:	1	2	3	4
0.20	1.02 ± 0.35	1.04 ± 0.22	1.09 ± 0.20	1.03 ± 0.20
0.16	1.03 ± 0.34	1.05 ± 0.23	1.11 ± 0.22	1.04 ± 0.22
0.12	1.04 ± 0.35	1.07 ± 0.24	1.14 ± 0.25	1.07 ± 0.27

Table D.3: Values for the 'speed of light' as obtained from the $\mathcal{N}_1$–$\mathcal{N}_1$ correlator. [Section 4.1.2]

Ground state, positive parity		$12^3 \times 24$, $\beta_1 = 7.90$, smeared–smeared		
am_q	$t_\mathrm{min} \ldots t_\mathrm{max}$	E	A	χ^2/d.o.f.
0.02	5...9	0.853 ± 0.023	0.800	1.255
0.03	5...10	0.893 ± 0.017	0.757	0.581
0.04	5...11	0.931 ± 0.014	0.756	0.253
0.05	5...12	0.969 ± 0.012	0.767	0.429
0.06	5...12	1.005 ± 0.011	0.782	0.531
0.08	5...12	1.075 ± 0.009	0.816	0.746
0.10	5...12	1.142 ± 0.008	0.852	0.930
0.12	5...12	1.205 ± 0.007	0.885	1.048
0.16	5...13	1.321 ± 0.007	0.940	1.216
0.20	5...13	1.431 ± 0.006	0.988	1.091
Excited state, positive parity		$12^3 \times 24$, $\beta_1 = 7.90$, smeared–smeared		
am_q	$t_\mathrm{min} \ldots t_\mathrm{max}$	E	A	χ^2/d.o.f.
0.10	4...8	1.834 ± 0.049	0.190	1.036
0.12	4...8	1.871 ± 0.040	0.165	0.736
0.16	4...8	1.952 ± 0.032	0.127	0.459
0.20	4...8	2.036 ± 0.028	0.100	0.323
Ground state, negativ parity		$12^3 \times 24$, $\beta_1 = 7.90$, smeared–smeared		
am_q	$t_\mathrm{min} \ldots t_\mathrm{max}$	E	A	χ^2/d.o.f.
0.08	18...22	1.457 ± 0.026	0.224	0.522
0.10	18...22	1.504 ± 0.022	0.211	0.300
0.12	18...22	1.554 ± 0.020	0.201	0.194
0.16	17...22	1.655 ± 0.017	0.185	0.255
0.20	16...22	1.752 ± 0.016	0.169	0.254
Excited state, negative parity		$12^3 \times 24$, $\beta_1 = 7.90$, smeared–smeared		
am_q	$t_\mathrm{min} \ldots t_\mathrm{max}$	E	A	χ^2/d.o.f.
0.08	18...22	1.556 ± 0.031	0.677	0.268
0.10	17...22	1.579 ± 0.026	0.613	0.062
0.12	17...22	1.617 ± 0.023	0.569	0.016
0.16	17...22	1.701 ± 0.019	0.499	0.309
0.20	16...22	1.788 ± 0.017	0.444	0.524

Table D.4: Fit parameters of fits to λ_1 and λ_2. [Section 4.2.3/4.3]

Ground state, positive parity		$12^3 \times 24$, $\beta_1 = 7.90$, smeared–point		
am_q	$t_\mathrm{min} \ldots t_\mathrm{max}$	E	A	χ^2/d.o.f.
0.02	6…11	0.827 ± 0.026	0.404	0.795
0.03	6…11	0.883 ± 0.017	0.404	0.377
0.04	6…11	0.928 ± 0.014	0.416	0.238
0.05	6…11	0.969 ± 0.012	0.431	0.208
0.06	6…11	1.007 ± 0.010	0.447	0.244
0.08	6…12	1.078 ± 0.009	0.480	0.425
0.10	6…12	1.145 ± 0.008	0.512	0.463
0.12	6…13	1.208 ± 0.007	0.544	0.632
0.16	6…13	1.326 ± 0.007	0.604	0.590
0.20	6…13	1.436 ± 0.006	0.660	0.606
Excited state, positive parity		$12^3 \times 24$, $\beta_1 = 7.90$, smeared–point		
am_q	$t_\mathrm{min} \ldots t_\mathrm{max}$	E	A	χ^2/d.o.f.
0.10	4…8	1.894 ± 0.031	0.304	0.962
0.12	4…8	1.924 ± 0.026	0.266	0.937
0.16	4…8	1.993 ± 0.021	0.208	1.123
0.20	4…8	2.069 ± 0.018	0.166	1.660
Ground state, negativ parity		$12^3 \times 24$, $\beta_1 = 7.90$, smeared–point		
am_q	$t_\mathrm{min} \ldots t_\mathrm{max}$	E	A	χ^2/d.o.f.
0.08	19…22	1.484 ± 0.015	0.186	0.219
0.10	18…22	1.532 ± 0.013	0.179	0.093
0.12	17…22	1.579 ± 0.012	0.173	0.211
0.16	17…22	1.675 ± 0.010	0.163	1.105
0.20	16…22	1.769 ± 0.009	0.154	2.246
Excited state, negative parity		$12^3 \times 24$, $\beta_1 = 7.90$, smeared–point		
am_q	$t_\mathrm{min} \ldots t_\mathrm{max}$	E	A	χ^2/d.o.f.
0.06	18…22	1.570 ± 0.033	0.770	1.029
0.08	18…22	1.584 ± 0.023	0.707	0.315
0.10	18…22	1.613 ± 0.019	0.659	0.126
0.12	17…22	1.652 ± 0.016	0.624	0.315
0.16	17…22	1.730 ± 0.014	0.559	0.470
0.20	16…22	1.813 ± 0.012	0.508	0.528

Table D.5: Fit parameters of fits to λ_1 and λ_2. [Section 4.2.3/4.3]

Ground state, positive parity $16^3 \times 32$, $\beta_1 = 7.90$, smeared–smeared				
am_q	$t_\mathrm{min} \ldots t_\mathrm{max}$	E	A	χ^2/d.o.f.
0.013	5…9	0.770 ± 0.023	0.664	1.309
0.014	5…10	0.786 ± 0.020	0.687	1.309
0.0145	5…11	0.793 ± 0.020	0.697	1.188
0.015	5…11	0.799 ± 0.019	0.707	1.285
0.016	5…11	0.811 ± 0.019	0.725	1.470
0.017	6…12	0.819 ± 0.016	0.716	1.264
0.018	6…12	0.826 ± 0.016	0.718	1.274
0.02	6…12	0.839 ± 0.015	0.724	1.280
0.025	6…12	0.868 ± 0.014	0.739	1.175
0.03	6…13	0.892 ± 0.013	0.755	1.387
0.04	6…13	0.935 ± 0.011	0.767	1.005
0.05	6…14	0.972 ± 0.009	0.773	0.748
0.06	6…14	1.008 ± 0.008	0.782	0.661
0.08	6…14	1.077 ± 0.007	0.807	0.727
0.10	6…15	1.141 ± 0.006	0.828	1.073
0.12	6…15	1.204 ± 0.005	0.860	1.121
0.16	6…15	1.321 ± 0.005	0.916	1.153
0.20	6…16	1.433 ± 0.004	0.973	1.339
Excited state, positive parity $16^3 \times 32$, $\beta_1 = 7.90$, smeared–smeared				
am_q	$t_\mathrm{min} \ldots t_\mathrm{max}$	E	A	χ^2/d.o.f.
0.06	4…6	1.868 ± 0.088	0.319	0.189
0.08	4…6	1.860 ± 0.058	0.258	0.017
0.10	4…8	1.878 ± 0.045	0.216	0.154
0.12	4…8	1.912 ± 0.039	0.187	0.214
0.16	4…9	1.987 ± 0.032	0.142	0.641
0.20	4…9	2.068 ± 0.028	0.111	1.076
Ground state, negativ parity $16^3 \times 32$, $\beta_1 = 7.90$, smeared–smeared				
am_q	$t_\mathrm{min} \ldots t_\mathrm{max}$	E	A	χ^2/d.o.f.
0.06	27…30	1.438 ± 0.025	0.259	0.383
0.08	26…30	1.483 ± 0.022	0.242	0.218
0.10	26…30	1.530 ± 0.020	0.229	0.093
0.12	25…30	1.577 ± 0.018	0.217	0.754
0.16	25…30	1.676 ± 0.017	0.197	0.531
0.20	25…30	1.772 ± 0.016	0.180	0.595
Excited state, negative parity $16^3 \times 32$, $\beta_1 = 7.90$, smeared–smeared				
am_q	$t_\mathrm{min} \ldots t_\mathrm{max}$	E	A	χ^2/d.o.f.
0.06	27…30	1.518 ± 0.035	0.698	3.556
0.08	27…30	1.532 ± 0.028	0.641	2.429
0.10	27…30	1.565 ± 0.023	0.594	1.840
0.12	26…30	1.605 ± 0.021	0.557	1.072
0.16	26…30	1.691 ± 0.018	0.489	0.802
0.20	25…30	1.781 ± 0.016	0.437	0.558

Table D.6: Fit parameters of fits to λ_1 and λ_2. [Section 4.2.3/4.3]

Ground state, positive parity $16^3 \times 32$, $\beta_1 = 7.90$, smeared–point				
am_q	$t_\mathrm{min} \ldots t_\mathrm{max}$	E	A	χ^2/d.o.f.
0.016	7…10	0.827 ± 0.020	0.444	0.112
0.017	7…11	0.831 ± 0.018	0.428	0.170
0.018	7…11	0.839 ± 0.018	0.428	0.174
0.02	7…12	0.848 ± 0.016	0.417	0.314
0.025	7…13	0.873 ± 0.014	0.412	0.333
0.03	7…13	0.896 ± 0.012	0.412	0.232
0.04	7…13	0.935 ± 0.010	0.412	0.145
0.05	7…14	0.973 ± 0.009	0.417	0.214
0.06	7…14	1.009 ± 0.008	0.427	0.350
0.08	7…14	1.076 ± 0.007	0.453	0.565
0.10	7…14	1.146 ± 0.006	0.480	0.652
0.12	8…15	1.201 ± 0.006	0.484	0.378
0.16	8…15	1.319 ± 0.005	0.536	0.269
0.20	8…15	1.429 ± 0.005	0.587	0.268
Excited state, positive parity $16^3 \times 32$, $\beta_1 = 7.90$, smeared–point				
am_q	$t_\mathrm{min} \ldots t_\mathrm{max}$	E	A	χ^2/d.o.f.
0.05	4…6	1.922 ± 0.082	0.469	0.230
0.06	4…7	1.884 ± 0.058	0.399	0.227
0.08	4…7	1.873 ± 0.041	0.328	0.145
0.10	4…8	1.889 ± 0.032	0.281	0.167
0.12	4…9	1.918 ± 0.028	0.245	0.258
0.16	4…9	1.989 ± 0.022	0.192	0.700
0.20	4…9	2.068 ± 0.019	0.156	1.462
Ground state, negativ parity $16^3 \times 32$, $\beta_1 = 7.90$, smeared–point				
am_q	$t_\mathrm{min} \ldots t_\mathrm{max}$	E	A	χ^2/d.o.f.
0.05	28…30	1.436 ± 0.019	0.201	0.028
0.06	27…30	1.457 ± 0.018	0.196	0.040
0.08	26…30	1.498 ± 0.015	0.186	0.096
0.10	26…30	1.544 ± 0.014	0.178	0.084
0.12	26…30	1.590 ± 0.012	0.172	0.221
0.16	25…30	1.684 ± 0.011	0.161	1.104
0.20	25…30	1.776 ± 0.010	0.151	2.024
Excited state, negative parity $16^3 \times 32$, $\beta_1 = 7.90$, smeared–point				
am_q	$t_\mathrm{min} \ldots t_\mathrm{max}$	E	A	χ^2/d.o.f.
0.05	27…30	1.601 ± 0.047	0.804	0.363
0.06	27…30	1.577 ± 0.038	0.732	0.129
0.08	27…30	1.578 ± 0.026	0.656	0.066
0.10	26…30	1.604 ± 0.021	0.615	0.391
0.12	26…30	1.638 ± 0.018	0.577	0.386
0.16	25…30	1.716 ± 0.015	0.517	0.373
0.20	25…30	1.800 ± 0.013	0.470	0.295

Table D.7: Fit parameters of fits to λ_1 and λ_2. [Section 4.2.3/4.3]

Ground state, positive parity $16^3 \times 32$, $\beta_1 = 8.35$, smeared–smeared				
am_q	$t_\mathrm{min} \ldots t_\mathrm{max}$	E	A	χ^2/d.o.f.
0.01	5…10	0.598 ± 0.013	0.824	0.750
0.015	5…11	0.630 ± 0.010	0.783	0.382
0.02	6…11	0.652 ± 0.010	0.748	0.382
0.03	6…11	0.695 ± 0.009	0.737	0.520
0.04	6…12	0.731 ± 0.008	0.734	0.837
0.05	6…13	0.768 ± 0.008	0.746	0.601
0.06	6…13	0.803 ± 0.007	0.762	0.629
0.08	6…14	0.872 ± 0.006	0.798	0.673
0.10	6…14	0.935 ± 0.006	0.826	0.689
0.12	6…14	0.995 ± 0.005	0.853	0.695
0.16	6…14	1.111 ± 0.005	0.905	0.702
0.20	6…14	1.222 ± 0.005	0.953	0.707
Excited state, positive parity $16^3 \times 32$, $\beta_1 = 8.35$, smeared–smeared				
am_q	$t_\mathrm{min} \ldots t_\mathrm{max}$	E	A	χ^2/d.o.f.
0.04	4…7	1.340 ± 0.041	0.342	0.395
0.05	4…7	1.334 ± 0.030	0.297	0.113
0.06	4…8	1.344 ± 0.024	0.260	0.171
0.08	4…8	1.376 ± 0.019	0.205	0.202
0.10	4…8	1.416 ± 0.016	0.163	0.328
0.12	4…8	1.458 ± 0.015	0.132	0.484
0.16	4…8	1.545 ± 0.013	0.090	0.828
0.20	4…8	1.632 ± 0.013	0.064	1.182
Ground state, negativ parity $16^3 \times 32$, $\beta_1 = 8.35$, smeared–smeared				
am_q	$t_\mathrm{min} \ldots t_\mathrm{max}$	E	A	χ^2/d.o.f.
0.03	28…30	1.004 ± 0.015	0.277	0.129
0.04	26…30	1.036 ± 0.013	0.266	0.184
0.05	26…30	1.065 ± 0.011	0.256	0.186
0.06	26…30	1.092 ± 0.010	0.246	0.289
0.08	26…30	1.144 ± 0.009	0.226	0.247
0.10	26…30	1.197 ± 0.009	0.208	0.118
0.12	26…30	1.248 ± 0.008	0.193	0.028
0.16	26…30	1.350 ± 0.008	0.166	0.037
0.20	26…30	1.448 ± 0.008	0.145	0.242
Excited state, negative parity $16^3 \times 32$, $\beta_1 = 8.35$, smeared–smeared				
am_q	$t_\mathrm{min} \ldots t_\mathrm{max}$	E	A	χ^2/d.o.f.
0.04	27…30	1.145 ± 0.030	0.804	0.191
0.05	27…30	1.138 ± 0.022	0.726	0.084
0.06	27…30	1.143 ± 0.018	0.668	0.152
0.08	26…30	1.174 ± 0.013	0.584	0.365
0.10	26…30	1.215 ± 0.011	0.519	0.389
0.12	26…30	1.259 ± 0.010	0.467	0.352
0.16	26…30	1.352 ± 0.009	0.386	0.204
0.20	26…30	1.447 ± 0.009	0.327	0.096

Table D.8: Fit parameters of fits to λ_1 and λ_2. [Section 4.2.3/4.3]

Ground state, positive parity		$16^3 \times 32$, $\beta_1 = 8.35$, smeared–point		
am_q	$t_\mathrm{min} \ldots t_\mathrm{max}$	E	A	χ^2/d.o.f.
0.015	6…12	0.638 ± 0.010	0.514	1.568
0.02	6…12	0.665 ± 0.009	0.512	1.778
0.03	7…16	0.702 ± 0.008	0.488	0.342
0.04	7…17	0.744 ± 0.007	0.504	0.533
0.05	7…17	0.782 ± 0.007	0.523	0.804
0.06	7…17	0.818 ± 0.006	0.545	1.007
0.08	7…17	0.886 ± 0.006	0.591	1.178
0.10	7…17	0.949 ± 0.006	0.636	1.165
0.12	7…17	1.010 ± 0.005	0.676	1.131
0.16	7…17	1.122 ± 0.005	0.745	1.251
0.20	7…17	1.229 ± 0.004	0.809	1.491
Excited state, positive parity		$16^3 \times 32$, $\beta_1 = 8.35$, smeared–point		
am_q	$t_\mathrm{min} \ldots t_\mathrm{max}$	E	A	χ^2/d.o.f.
0.04	4…8	1.363 ± 0.025	0.611	0.833
0.05	4…10	1.361 ± 0.019	0.536	0.666
0.06	4…10	1.369 ± 0.015	0.477	0.902
0.08	4…10	1.398 ± 0.012	0.382	1.462
0.10	4…10	1.433 ± 0.010	0.311	1.944
0.12	4…11	1.472 ± 0.009	0.257	1.968
0.16	5…10	1.576 ± 0.011	0.205	0.521
0.20	5…11	1.660 ± 0.010	0.152	0.439
Ground state, negativ parity		$16^3 \times 32$, $\beta_1 = 8.35$, smeared–point		
am_q	$t_\mathrm{min} \ldots t_\mathrm{max}$	E	A	χ^2/d.o.f.
0.03	27…30	1.048 ± 0.010	0.273	0.057
0.04	27…30	1.072 ± 0.008	0.262	5.017
0.05	27…30	1.097 ± 0.007	0.253	7.199
0.06	27…30	1.121 ± 0.006	0.244	8.564
0.08	27…30	1.169 ± 0.005	0.229	10.137
0.10	27…30	1.217 ± 0.005	0.215	11.252
0.12	26…30	1.265 ± 0.005	0.204	9.111
0.16	26…30	1.358 ± 0.005	0.181	10.748
0.20	26…30	1.450 ± 0.005	0.163	13.457
Excited state, negative parity		$16^3 \times 32$, $\beta_1 = 8.35$, smeared–point		
am_q	$t_\mathrm{min} \ldots t_\mathrm{max}$	E	A	χ^2/d.o.f.
0.04	26…30	1.174 ± 0.018	1.106	1.219
0.05	26…30	1.179 ± 0.014	1.027	1.391
0.06	27…30	1.189 ± 0.012	0.962	2.796
0.08	27…30	1.219 ± 0.009	0.856	4.197
0.10	27…30	1.256 ± 0.008	0.771	4.950
0.12	27…30	1.297 ± 0.007	0.701	5.110
0.16	25…30	1.383 ± 0.006	0.591	2.634
0.20	24…30	1.470 ± 0.006	0.509	2.150

Table D.9: Fit parameters of fits to λ_1 and λ_2. [Section 4.2.3/4.3]

ρ **meson** $16^3 \times 32$, $\beta_1 = 7.90$		ρ **meson** $16^3 \times 32$, $\beta_1 = 8.35$	
am_{q}	am_ρ	am_{q}	am_ρ
0.02	0.6414 ± 0.0276	0.010	0.4495 ± 0.0214
0.03	0.6561 ± 0.0154	0.015	0.4517 ± 0.0152
0.04	0.6728 ± 0.0108	0.020	0.4604 ± 0.0121
0.05	0.6931 ± 0.0091	0.030	0.4813 ± 0.0088
0.06	0.7095 ± 0.0078	0.040	0.5019 ± 0.0071
0.08	0.7422 ± 0.0063	0.050	0.5217 ± 0.0060
0.10	0.7747 ± 0.0052	0.060	0.5410 ± 0.0054
0.12	0.8083 ± 0.0042	0.080	0.5790 ± 0.0045
0.16	0.8733 ± 0.0032	0.100	0.6164 ± 0.0039
0.20	0.9372 ± 0.0029	0.120	0.6533 ± 0.0035
		0.160	0.7254 ± 0.0030
		0.200	0.7950 ± 0.0027

Table D.10: Data points used for the chiral extrapolation of the ρ meson, taken from work done in conjunction with [Sch02] ($\beta_1 = 8.35$) and [Hie04] ($\beta_1 = 7.90$). [Section 4.2.4]

	am_{q}	am_ρ	χ^2/d.o.f.	M_{phys} [MeV]
$16^3 \times 32$, $\beta_1 = 7.90$	$0.010 \ldots 0.20$	0.610 ± 0.012	0.007	770
$16^3 \times 32$, $\beta_1 = 8.35$	$0.013 \ldots 0.20$	0.432 ± 0.008	0.282	770

Table D.11: Results from the chiral extrapolation for the ρ meson. [Section 4.2.4]

smeared–point				$12^3 \times 24$, $\beta_1 = 7.90$
	am_{q}	aM	χ^2/d.o.f.	M_{phys} [MeV]
$N(939)$	$0.02 \ldots 0.20$	0.559 ± 0.027	0.060	945 ± 42
N'	$0.08 \ldots 0.20$	1.722 ± 0.046	0.044	2178 ± 101
$N(1535)$	$0.08 \ldots 0.20$	1.294 ± 0.018	0.002	1637 ± 55
$N(1650)$	$0.08 \ldots 0.20$	1.420 ± 0.027	0.067	1796 ± 70
smeared–smeared				$12^3 \times 24$, $\beta_1 = 7.90$
	am_{q}	aM	χ^2/d.o.f.	M_{phys} [MeV]
$N(939)$	$0.02 \ldots 0.20$	0.570 ± 0.027	0.034	955 ± 41
N'	$0.10 \ldots 0.20$	1.626 ± 0.033	0.004	2057 ± 122
$N(1535)$	$0.08 \ldots 0.20$	1.258 ± 0.030	0.005	1591 ± 70
$N(1650)$	$0.08 \ldots 0.20$	1.380 ± 0.036	0.115	1746 ± 81
smeared–point				$16^3 \times 32$, $\beta_1 = 7.90$
	am_{q}	aM	χ^2/d.o.f.	M_{phys} [MeV]
$N(939)$	$0.016 \ldots 0.20$	0.577 ± 0.023	0.117	961 ± 38
N'	$0.08 \ldots 0.20$	1.716 ± 0.047	0.122	2170 ± 101
$N(1535)$	$0.04 \ldots 0.20$	1.319 ± 0.021	0.045	1668 ± 60
$N(1650)$	$0.08 \ldots 0.20$	1.412 ± 0.030	0.133	1786 ± 74
smeared–smeared				$16^3 \times 32$, $\beta_1 = 7.90$
	am_{q}	aM	χ^2/d.o.f.	M_{phys} [MeV]
$N(939)$	$0.02 \ldots 0.20$	0.569 ± 0.021	0.189	954 ± 36
$N(1535)$	$0.06 \ldots 0.20$	1.291 ± 0.026	0.006	1633 ± 65
$N(1650)$	$0.06 \ldots 0.20$	1.369 ± 0.035	0.234	1731 ± 78
smeared–point				$16^3 \times 32$, $\beta_1 = 8.35$
	am_{q}	aM	χ^2/d.o.f.	M_{phys} [MeV]
$N(939)$	$0.015 \ldots 0.20$	0.314 ± 0.017	0.314	998 ± 36
N'	$0.06 \ldots 0.20$	1.220 ± 0.013	0.842	2169 ± 63
$N(1535)$	$0.03 \ldots 0.20$	0.980 ± 0.008	0.112	1742 ± 45
$N(1650)$	$0.05 \ldots 0.20$	1.057 ± 0.013	0.830	1880 ± 76
smeared–smeared				$16^3 \times 32$, $\beta_1 = 8.35$
	am_{q}	aM	χ^2/d.o.f.	M_{phys} [MeV]
$N(939)$	$0.01 \ldots 0.20$	0.297 ± 0.013	0.843	969 ± 39
$N(1535)$	$0.03 \ldots 0.20$	0.936 ± 0.013	0.132	1665 ± 52
$N(1650)$	$0.06 \ldots 0.20$	0.993 ± 0.017	0.283	1766 ± 62

Table D.12: Results for the linear fits of the states $N(939)$,N', $N(1535)$ and $N(1650)$. [Section 4.3]

$M_{N(939)}/M_\rho$	$M_{N(1535)}/M_{N(939)}$	$M_{N(1650)}/M_{N(939)}$	$M_{N(1650)}/M_{N(1535)}$
experiment			
1.220	1.633	1.755	1.075
$12^3 \times 24$, $\beta_1 = 7.90$, smeared–point			
1.227 ± 0.054	1.732 ± 0.142	1.901 ± 0.163	1.097 ± 0.082
$12^3 \times 24$, $\beta_1 = 7.90$, smeared–smeared			
1.240 ± 0.053	1.666 ± 0.151	1.828 ± 0.171	1.097 ± 0.104
$16^3 \times 32$, $\beta_1 = 7.90$, smeared–point			
1.248 ± 0.049	1.736 ± 0.136	1.858 ± 0.163	1.071 ± 0.086
$16^3 \times 32$, $\beta_1 = 7.90$, smeared–smeared			
1.239 ± 0.047	1.712 ± 0.138	1.814 ± 0.157	1.060 ± 0.094
$16^3 \times 32$, $\beta_1 = 8.35$, smeared–point			
1.296 ± 0.047	1.745 ± 0.113	1.884 ± 0.149	1.079 ± 0.073
$16^3 \times 32$, $\beta_1 = 8.35$, smeared–smeared			
1.258 ± 0.051	1.718 ± 0.128	1.822 ± 0.144	1.061 ± 0.073

Table D.13: Results from the chiral extrapolation. The ratios are given as dimensionless numbers. Experimental values are taken from [H$^+$02] [Section 4.3]

$N(939)$	am_q	$\mathrm{Re}\, c_1$	$\mathrm{Im}\, c_2$	$\mathrm{Re}\, c_3$
	0.0135	0.903 ± 0.005	0.172 ± 0.046	0.393 ± 0.020
	0.014	0.902 ± 0.005	0.159 ± 0.041	0.400 ± 0.018
	0.0145	0.901 ± 0.004	0.148 ± 0.037	0.407 ± 0.017
	0.015	0.900 ± 0.004	0.140 ± 0.035	0.412 ± 0.016
	0.016	0.898 ± 0.004	0.126 ± 0.030	0.421 ± 0.014
	0.017	0.896 ± 0.004	0.115 ± 0.027	0.428 ± 0.013
	0.018	0.894 ± 0.004	0.106 ± 0.024	0.434 ± 0.012
	0.025	0.885 ± 0.004	0.070 ± 0.014	0.460 ± 0.008
	0.02	0.892 ± 0.004	0.095 ± 0.020	0.443 ± 0.010
	0.03	0.880 ± 0.003	0.058 ± 0.010	0.472 ± 0.007
	0.04	0.871 ± 0.003	0.042 ± 0.007	0.489 ± 0.005
	0.05	0.864 ± 0.003	0.031 ± 0.005	0.503 ± 0.005
	0.06	0.857 ± 0.002	0.025 ± 0.004	0.514 ± 0.004
	0.08	0.847 ± 0.002	0.016 ± 0.003	0.532 ± 0.003
	0.10	0.838 ± 0.003	0.012 ± 0.003	0.546 ± 0.003
	0.12	0.830 ± 0.003	0.009 ± 0.002	0.557 ± 0.002
	0.16	0.818 ± 0.001	0.005 ± 0.001	0.575 ± 0.002
	0.20	0.808 ± 0.001	0.003 ± 0.001	0.589 ± 0.002
N'	am_q	$\mathrm{Re}\, c_1$	$\mathrm{Im}\, c_2$	$\mathrm{Re}\, c_3$
	0.05	0.104 ± 0.020	0.968 ± 0.010	-0.229 ± 0.032
	0.06	0.115 ± 0.015	0.966 ± 0.007	-0.231 ± 0.023
	0.08	0.129 ± 0.012	0.964 ± 0.005	-0.233 ± 0.015
	0.10	0.139 ± 0.009	0.962 ± 0.004	-0.234 ± 0.011
	0.12	0.147 ± 0.007	0.961 ± 0.003	-0.235 ± 0.009
	0.16	0.157 ± 0.006	0.959 ± 0.003	-0.235 ± 0.007
	0.20	0.165 ± 0.005	0.958 ± 0.002	-0.234 ± 0.006
$N(1535)$	am_q	$\mathrm{Re}\, c_1$	$\mathrm{Im}\, c_2$	$\mathrm{Re}\, c_3$
	0.05	0.689 ± 0.157	0.640 ± 0.179	-0.333 ± 0.041
	0.06	0.570 ± 0.204	0.750 ± 1.349	-0.305 ± 0.060
	0.08	0.790 ± 0.022	-0.543 ± 0.040	-0.283 ± 0.018
	0.10	0.806 ± 0.013	-0.501 ± 0.026	-0.316 ± 0.012
	0.12	0.810 ± 0.009	-0.477 ± 0.019	-0.340 ± 0.009
	0.16	0.809 ± 0.005	-0.449 ± 0.013	-0.378 ± 0.007
	0.20	0.804 ± 0.004	-0.433 ± 0.010	-0.408 ± 0.005
$N(1650)$	am_q	$\mathrm{Re}\, c_1$	$\mathrm{Im}\, c_2$	$\mathrm{Re}\, c_3$
	0.05	-0.037 ± 0.083	0.745 ± 1.415	0.157 ± 0.381
	0.06	0.000 ± 0.022	-0.624 ± 1.422	-0.229 ± 0.074
	0.08	0.010 ± 0.020	0.835 ± 0.026	-0.286 ± 0.012
	0.10	0.006 ± 0.012	0.861 ± 0.015	-0.279 ± 0.009
	0.12	0.005 ± 0.009	0.875 ± 0.010	-0.275 ± 0.007
	0.16	0.004 ± 0.006	0.890 ± 0.006	-0.273 ± 0.005
	0.20	0.003 ± 0.004	0.898 ± 0.005	-0.270 ± 0.004

Table D.14: Non-vanishing coefficients that form the optimal operators. Given for the $16^3 \times 32$ lattice at $\beta_1 = 7.90$. [Section 4.4]

Bibliography

[A+93] Allton, C. R., et al. Gauge invariant smearing and matrix correlators using Wilson fermions at Beta = 6.2. *Phys. Rev.*, D47:5128–5137, 1993, [eprint: *hep-lat/9303009*].

[A+00] Aoki, S., et al. Quenched light hadron spectrum. *Phys. Rev. Lett.*, 84:238–241, 2000, [eprint: *hep-lat/9904012*].

[A+03] Aoki, S., et al. Light hadron spectrum and quark masses from quenched lattice QCD. *Phys. Rev.*, D67:034503, 2003, [eprint: *hep-lat/0206009*].

[AGJ+94] Alexandrou, C., Gusken, S., Jegerlehner, F., Schilling, K., and Sommer, R. The static approximation of heavy - light quark systems: A systematic lattice study. *Nucl. Phys.*, B414:815–855, 1994, [eprint: *hep-lat/9211042*].

[B+97] Best, C., et al. Pion and rho structure functions from lattice QCD. *Phys. Rev.*, D56:2743–2754, 1997, [eprint: *hep-lat/9703014*].

[B+03] Basak, S., et al. Baryon operators and spectroscopy in lattice QCD. 2003, [eprint: *hep-lat/0312003*].

[BCG+03] Brömmel, D., Crompton, P., Gattringer, C., Glozman, L. Y., Lang, C.B., Schäfer, A., and Schaefer, S. Low-lying nucleons from chirally improved fermions. 2003, [eprint: *hep-lat/0309036*]. Presented at 21st International Symposium on Lattice Field Theory (LATTICE 2003).

[BCG+04] Brömmel, D., Crompton, P., Gattringer, C., Glozman, L. Y., Lang, C.B., Schäfer, A., and Schaefer, S. Excited nucleons with chirally improved fermions. *Phys. Rev.*, D69:094513, 2004, [eprint: *hep-ph/0307073*].

[BGR] *Coefficients for the Chirally Improved Dirac Operator.* URL: `http://physik.uni-graz.at/ cbl/research/data/dci/`.

[BH97] Binder, K., and Heermann, D. W. *Monte Carlo Simulation in Statistical Physics: An introduction*, volume 80 of *Springer Series in Solid-State Sciences*. Springer, 3rd edition, 1997.

[Bha88] Bhaduri, R. K. *Models of the Nucleon: From Quarks to Soliton*, volume 22 of *Lecture notes and supplements in physics*. Addison-Wesley, 1988.

[CDKS82] Chung, Y., Dosch, H. G., Kremer, M., and Schall, D. Baryon sum rules and chiral symmetry breaking. *Nucl. Phys.*, B197:55, 1982.

[CJ97] Cohen, T. D., and Ji, X.-D. Chiral multiplets of hadron currents. *Phys. Rev.*, D55:6870–6876, 1997, [eprint: *hep-ph/9612302*].

[Clo79] Close, F. E. *An Introduction to Quarks and Partons.* Academic Press, 1979.

[CR00] Capstick, S., and Roberts, W. Quark models of baryon masses and decays. *Prog. Part. Nucl. Phys.*, 45:S241–S331, 2000, [eprint: *nucl-th/0008028*].

[D+03] Dong, S. J., et al. Roper resonance and s(11)(1535) from lattice qcd. 2003, [eprint: *hep-ph/0306199*].

[DGH96] Donoghue, J. F., Golowich, E., and Holstein, B. R. *Dynamics of the standard model.* Cambridge Monographs on Particle Physics, Nuclear Physics, and Cosmology. Cambridge University Press, 1996.

[F+82] Fucito, F., et al. Hadron spectroscopy in lattice QCD. *Nucl. Phys.*, B210:407, 1982.

[FH65] Feynman, R. P., and Hibbs, A. R. *Quantum Mechanics and Path Integrals.* McGraw-Hill, 1965.

[G+04] Gattringer, C., et al. Quenched spectroscopy with fixed-point and chirally improved fermions. *Nucl. Phys.*, B677:3–51, 2004, [eprint: *hep-lat/0307013*].

[Gat01] Gattringer, C. A new approach to Ginsparg-Wilson fermions. *Phys. Rev.*, D63:114501, 2001, [eprint: *hep-lat/0003005*].

[Gat03a] Gattringer, C. Lecture notes to *Quantenfeldtheorie mit Gitterregularisierung.* Universität Regensburg, 2003. unpublished.

[Gat03b] Gattringer, C. Recent results from systematic parameterizations of Ginsparg-Wilson fermions. *Nucl. Phys. Proc. Suppl.*, 119:122–130, 2003, [eprint: *hep-lat/0208056*].

[GHL01] Gattringer, C., Hip, I., and Lang, C.B. Approximate Ginsparg-Wilson fermions: a first test. *Nucl. Phys.*, B597:451, 2001.

[GHS02] Gattringer, C., Hoffmann, R., and Schaefer, S. Setting the scale for the Luescher-Weisz action. *Phys. Rev.*, D65:094503, 2002, [eprint: *hep-lat/0112024*].

[Gol61] Goldstone, J. Field theories with 'superconductor' solutions. *Nuovo Cim.*, 19:154–164, 1961.

[Gup98] Gupta, R. Introduction to Lattice QCD. 1998, [eprint: *hep-lat/9807028*].

[GW82] Ginsparg, P. H., and Wilson, K. G. A remnant of chiral symmetry on the lattice. *Phys. Rev.*, D25:2649, 1982.

[H+02] Hagiwara, K., et al. Review of particle physics. *Phys. Rev.*, D66:010001, URL: `http://pdg.lbl.gov/`, 2002.

[Hau02] Hauswirth, S. *Light Hadron Spectroscopy in Quenched Lattice QCD with Chiral Fixed-Point Fermions*. PhD thesis, Universität Bern, 2002, [eprint: *hep-lat/0204015*].

[Hie04] Hierl, D. *Pion-Streunung auf dem Gitter mit chiral verbesserten Fermionen*. Diploma Thesis, Universität Regensburg, 2004. unpublished.

[HK83] Hey, A. J., and Kelly, R. L. Baryon spectroscopy. *Phys. Rept.*, 96:71–204, 1983.

[Iof81] Ioffe, B. L. Calculation of baryon masses in quantum chromodynamics. *Nucl. Phys.*, B188:317–341, 1981. [Erratum-ibid. B191, 591-592 (1981)].

[L+02] Lepage, G. P., et al. Constrained curve fitting. *Nucl. Phys. Proc. Suppl.*, 106:12–20, 2002, [eprint: *hep-lat/0110175*].

[L+03] Lee, F. X., et al. Excited baryons from Bayesian priors and overlap fermions. *Nucl. Phys. Proc. Suppl.*, 119:296–298, 2003, [eprint: *hep-lat/0208070*].

[Lan] Lang, C.B. *private communication*.

[Lei95] Leinweber, D. B. Nucleon properties from unconventional interpolating fields. *Phys. Rev.*, D51:6383–6393, 1995, [eprint: *nucl-th/9406001*].

[LM93] Lepage, G. P., and Mackenzie, P. B. On the viability of lattice perturbation theory. *Phys. Rev.*, D48:2250–2264, 1993, [eprint: *hep-lat/9209022*].

[LW85] Lüscher, M., and Weisz, P. On-shell improved lattice gauge theories. *Commun. Math. Phys.*, 97:59, 1985. [Erratum-ibid. 98, 433 (1985)].

[LW90] Lüscher, M., and Wolff, U. How to calculate the elastic scattering matrix in two-dimensional quantum field theories by numerical simulation. *Nuc. Phys.*, B339:222, 1990.

[Lyo91] Lyons, L. *A Practical Guide to Data Analysis for Physical Science Students*. Cambridge University Press, 1991.

[M+03] Melnitchouk, W., et al. Excited baryons in lattice qcd. *Phys. Rev.*, D67:114506, 2003, [eprint: *hep-lat/0202022*].

[MM97] Montvay, I., and Münster, G. *Quantum Fields on a Lattice*. Cambridge Monographs on Mathematical Physics. Cambridge University Press, 1997.

[Mor02] Morningstar, C. Bayesian curve fitting for lattice gauge theorists. *Nucl. Phys. Proc. Suppl.*, 109A:185–191, 2002, [eprint: *hep-lat/0112023*].

[Mor03] Morningstar, C. Baryon spectroscopy on the lattice: Recent results. 2003, [eprint: *nucl-th/0308026*].

[MR03] Maynard, C. M., and Richards, D. G. Excitations of the nucleon with dynamical fermions. *Nucl. Phys. Proc. Suppl.*, 119:287–289, 2003, [eprint: *hep-lat/0209165*].

[MT83] Michael, C., and Teasdale, I. Extracting glueball masses from lattice QCD. *Nucl. Phys.*, B215:433, 1983.

[Mut00] Muta, T. *Foundations of Quantum Chromodynamics.* World Scientific Publishing, 2nd edition, 2000.

[Nie99] Niedermayer, F. Exact chiral symmetry, topological charge and related topics. *Nucl. Phys. Proc. Suppl.*, 73:105–119, 1999, [eprint: *hep-lat/9810026*].

[PS95] Peskin, M. E., and Schroeder, D. V. *An Introduction to Quantum Field Theory.* Perseus Books, 1995.

[R+02] Richards, D. G., et al. Excited nucleon spectrum using a non-perturbatively improved clover fermion action. *Nucl. Phys. Proc. Suppl.*, 109A:89–95, 2002, [eprint: *hep-lat/0112031*].

[Sas03] Sasaki, S. Latest results from lattice qcd for the roper resonance. *Prog. Theor. Phys. Suppl.*, 151:143–148, 2003, [eprint: *nucl-th/0305014*].

[SBO02] Sasaki, S., Blum, T., and Ohta, S. A lattice study of the nucleon excited states with domain wall fermions. *Phys. Rev.*, D65:074503, 2002, [eprint: *hep-lat/0102010*].

[Sch95] Schwabl, F. *Quantum Mechanics.* Springer, 2nd rev. edition, 1995.

[Sch02] Schaefer, S. *Chiral symmetry and hadronic measurements on the lattice.* PhD thesis, Universität Regensburg, 2002.
URL: `http://www.bibliothek.uni-regensburg.de/...`
`...opus/volltexte/2003/131/`.

[Ski89] Skilling, J., editor. *Maximum entropy and Bayesian methods.* Fundamental theories of physics. Kluwer, 3rd edition, 1989.

[SSHA03] Sasaki, S., Sasaki, K., Hatsuda, T., and Asakawa, M. Bayesian approach to the first excited nucleon state in lattice QCD. *Nucl. Phys. Proc. Suppl.*, 119:302–304, 2003, [eprint: *hep-lat/0209059*].

[Y+02] Yamazaki, T., et al. Spectral function and excited states in lattice QCD with maximum entropy method. *Phys. Rev.*, D65:014501, 2002, [eprint: *hep-lat/0105030*].

[ZJ02] Zinn-Justin, J. *Quantum field theory and critical phenomena.* Clarendon Press, 4th edition, 2002.

Acknowledgements

I would like to thank Andreas Schäfer for the opportunity to work in the field of lattice QCD and for providing advice when necessary. No less I am indebted to Christof Gattringer for supervising my work and for patiently answering my sometimes silly questions – again and again. Furthermore I thank Meinulf Göckeler for his knowledge and Stefan Schaefer for some hints and also the first lines of code to start from. Likewise, I appreciate the collaboration with the group in Graz, especially Leonid Ya. Glozman. I also have to mention Dieter Hierl with whom I had helpful discussions on various problems arising during our work.

I further thank: Alexander Weber, who put up with proof reading the thesis and who was always up for interesting discussions about all kinds of physics – and real things of course. Moreover Michael Malorny for joining me grumbling about the world in general and politicians in particular, even from far away Grenoble. And not to forget all the other cards and card players for the distraction in between.

Most importantly I have to thank my parents. Without them, studying physics would not have been possible in the first place. They supported me whenever needed and waited patiently for me to graduate.

Erklärung

Hiermit erkläre ich, daß ich die Diplomarbeit selbständig angefertigt und keine Hilfsmittel außer den in der Arbeit angegebenen benutzt habe.

Regensburg, den 30. Januar 2004 .....
(Dirk Brömmel)